Satellite-based Fusion of Image/Inertial Sensors for Precise Geolocation

THESIS

Neil R. Jesse, Captain, USAF

AFIT/EO/ENG/09-04

DEPARTMENT OF THE AIR FORCE
AIR UNIVERSITY

AIR FORCE INSTITUTE OF TECHNOLOGY

Wright-Patterson Air Force Base, Ohio

The views expressed in this thesis are those of the author and do not reflect the official policy or position of the United States Air Force, Department of Defense, or the United States Government.

AFIT/EO/ENG/09-04

Satellite-based Fusion of Image/Inertial Sensors for Precise Geolocation

THESIS

Presented to the Faculty

Department of Electrical and Computer Engineering

Graduate School of Engineering and Management

Air Force Institute of Technology

Air University

Air Education and Training Command

In Partial Fulfillment of the Requirements for the

Degree of Master of Science in Electrical Engineering

Neil R. Jesse, BSEE

Captain, USAF

March 2009

AFIT/EO/ENG/09-04

Satellite-based Fusion of Image/Inertial Sensors for Precise Geolocation

Neil R. Jesse, BSEE

Captain, USAF

Approved:

Lt Col Michael J. Veth, PhD (Chairman)	24 Feb 09 Date
John F. Raquet, PhD (Member)	24 Feb 09 Date
Maj Jason D. Schmidt, PhD (Member)	24 Feb 09 Date

Abstract

The ability to produce high-resolution images of the Earth's surface from space has flourished in recent years with the continuous development and improvement of satellite-based imaging sensors. Earth-imaging satellites often rely on complex onboard navigation systems, with dependence on Global Positioning System (GPS) tracking and/or continuous post-capture georegistration, to accurately geolocate ground targets of interest to either commercial and military customers. Consequently, these satellite systems are often massive, expensive, and susceptible to poor or unavailable target tracking capabilities in GPS-denied environments. Previous research has demonstrated that a tightly-coupled image-aided inertial navigation system (INS), using existing onboard imaging sensors, can provide significant target tracking improvement over that of conventional navigation and tracking systems. Satellite-based image-aided navigation is explored as a means of autonomously tracking stationary ground targets by implementing feature detection and recognition algorithms to accurately predict a ground target's pixel location within subsequent satellite images. The development of a robust satellite-based image-aided INS model offers a convenient, low-cost, low-weight and highly accurate solution to the geolocation precision problem, without the need of human interaction or GPS dependency, while simultaneously providing redundant and sustainable satellite navigation capabilities.

Acknowledgements

I would like to recognize a number of people at the Air Force Institute of Technology, who, thanks to their technical support, have made this thesis possible, including my advisor, my committee members and my fellow graduate students. Also, I extend my gratitude to the Advanced Multi-spectral Sensors Group at Ball Aerospace & Technologies Corp. for their cooperation and consultation. Not least, perhaps, I should thank my wife and daughter for their patience, understanding, and encouragement.

Neil R. Jesse

Table of Contents

Page

List of Figures

List of Tables

List of Abbreviations

Abbreviation		Page
GPS	Global Positioning System	2
EKF	Extended Kalman Filter	6
INS	Inertial Navigation System	6
DCM	Direction Cosine Matrix	7
NED	North, East and Down	8
DCM	Direction Cosine Matrix	10
MMSE	Minimum Mean-Square-Error	16
LEO	Low Earth Orbit	25
ISS	International Space Station	25
GEO	Geosynchronous Orbit	25
HEO	High Earth orbit	25
MOL	Molniya Orbit	26
CCD	Charge-Coupled Device	27
CMOS	Metaloxide Semiconductor	27
RMS	Root Mean Square	33
H-V	Hufnagel-Valley	34
HAST	High Accuracy Star Tracker	43
SSD	Sum-of-Squared-Difference	43
NASA	National Aeronautics and Space Administration	62
RSS	Root-Sum-Squared	80
WGS 84	World Geodetic System 1984	105

Satellite-based Fusion of Image/Inertial Sensors for Precise Geolocation

I. Introduction

This research outlines the methodology of integrating the imaging sensors of a satellite-based Earth observation system with the inertial sensors of the satellite's navigation system in order to accurately locate a ground target of interest and autonomously track that target over an extended period of time. The image-aided satellite navigation system design uses conventional feature detection and recognition methods in order to provide robust, rapid target tracking capability without the need for additional vehicle-based or ground-based hardware or dependency on external navigation reference sources.

1.1 Background

As early as the mid-1950s, the desire to explore the space beyond our skies led to the development of man-made satellites. Ever since the first of these satellites, the Soviet-built Sputnik 1, was launched in 1957, scientists, astronomers, and engineers were eager to harness the vast capabilities of the space environment. These efforts paved the way for space-based breakthroughs in communications, weather, imaging, and manned space flight.

In particular, the numerous applications involving terrestrial imagery from space have led to high demands in the areas of agriculture, geology, education, intelligence, and warfare. At any one point in time, day or night, ground images are continuously captured from space by observation satellite systems orbiting the Earth. Often, a ground target of interest's geographic location (referred to as the target's "geoloca-

tion") is desired; for example, for commercial or military purposes. However, the ability to quickly, accurately and efficiently detect and track a ground target from space, without the need of sophisticated, costly, or deniable systems, has been an ongoing challenge of the space community.

1.2 Problem Definition

Current Earth-imaging satellite systems often rely on either external navigation reference sources, such as the Global Positioning System (GPS), or continuous post-capture georegistration, to provide precise ground target geolocation. Often, these current imaging system designs are massive, expensive, sluggish, and jammable. An additional risk to highly complex systems is the increased susceptibility to unforeseen hardware-related anomalies. Since high image resolution requirements must be met in order to track many man-made targets, conventional satellite databases often demand high memory capacity. The resulting image processing time is often impractical. Additionally, if routine hardware calibration is required onboard the satellite in order to maintain navigation accuracy, the resulting image capturing performance could degrade if such a calibration where to inhibit the imaging sensor's ability to locate the ground target.

The motivation of this research is to develop an inexpensive, light-weight, highly accurate image-aided inertial satellite navigation system without the need for human interaction or dependence on external navigation reference systems, such as GPS. Image-aided geolocation algorithms are of interest for both military and civilian space applications in which weight, cost, and time savings are of interest and/or the denial of GPS is of concern. Any civilian or military satellite system producing digital imagery would benefit from a robust, low-cost, autonomous satellite system providing precise geolocation capabilities.

1.3 Scope

Satellite-based image-aided navigation is explored as a means of autonomously tracking a stationary ground target within subsequent satellite images and using feature recognition algorithms to predict the target's pixel location within each image. In order to make this problem tractable, certain assumptions are made. Although the effects of atmospheric turbulence are covered in detail, weather and lighting conditions are assumed to be favorable at the location of interest. For example, environmental limitations such as precipitation, fog, cloud cover, and poor sunlight conditions are not covered. Image quality issues, including ego-motion disparity and motion blur among subsequent images are also not specifically identified in this research. Also, for simplicity, a spherical Earth model of constant elevation is assumed.

1.4 Research Contributions

Many contributions are made on behalf of this research. These contributions are primarily defined in Chapter II and implemented in Chapter III of this thesis, and are listed here in their respective order of appearance.

The extended Kalman filter is utilized to efficiently estimate the state of the nonlinear dynamic satellite navigation system from a series of noisy measurements [12,13]. A background in orbital mechanics, specifically, the systematic transformation from geometrical orbital parameters to satellite position and velocity vectors, provide nominal satellite trajectory modeling [15, 22]. A detailed understanding of the turbulent and refractive effects on an image propagating through the atmosphere provides insight to realistic image system modeling [1, 5, 21]. The primary contribution to image-aided navigation theory demonstrates that tightly-coupled image-aided inertial navigation can provide significant target tracking improvement over that of conventional navigation systems [28,30]. Image matching theory utilized the sum-of-squared-difference algorithm, in which a target with unique features can be tracked among a series of pixelated images by measuring the correspondence between images [3, 16].

Finally, the development of the stochastic projection method provided a means of accurately and optimally predicting a target's pixel location within in a series of images by limiting the number false matches and constraining the feature correspondence search [28, 30].

1.5 Methodology

The thesis is organized as follows:

- *Chapter II*: Chapter II provides the detailed mathematical background of the image/inertial sensor integration problem. The first sections of this chapter cover mathematical notation, reference-frame declarations, coordinate transformations, inertial sensor design, and Kalman filtering. The following sections review orbital dynamics, specifically, Newtonian and Keplerian theory, satellite trajectory transformation, and orbital classifications. Further sections discuss optical modeling, spatial coherence, and imaging through turbulence, specifically, the effects of image jitter and horizontal light refraction displacement. The following sections cover image-aided navigation theory, image matching techniques, and georeferencing theory. The final section of this chapter covers the stochastic projection method.
- *Chapter III*: Chapter III covers the methodology of this research, implementing the theories covered in Chapter II to build a satellite-based image-aided navigation system. The first sections develop the orbital model, satellite vehicle model, and imaging system model. The next sections assign noise modeling with respect to atmospheric turbulence, image sensors, satellite trajectory, and optical measurements. The following sections develop the truth model with respect to the ground target and implement image matching and georeferencing techniques to provide an accurate target location error prediction. The final section of this chapter is the implementation of the extended Kalman filter.

- *Chapter IV*: Chapter IV supports the Monte Carlo results and observations of the image-aided satellite navigation system. Two distinct profiles, one satellite in a low-Earth orbit with high image resolution, and the other in a high-Earth orbit with low image resolution, are produced. The respective vehicle position, vehicle velocity, vehicle attitude, and target location errors are analyzed in detail in the following sections, both with and without the introduction of image-aided target predictions.
- *Chapter V*: Chapter V provides conclusions and closing remarks regarding the image/inertial integrated navigation system, as well as potential areas for future exploration in the subject.

II. Background

This chapter reviews the mathematical and conceptual background required to fully develop an image-aided navigation system of an orbiting satellite. First, a definition of the mathematical notation used throughout the document will be presented, followed by reference frame definitions. A basic understanding of inertial navigation will follow. Next, a review of both linear and nonlinear Kalman filtering methods will be discussed, specifically, the Extended Kalman Filter (EKF). Orbital mechanics required to define a satellite's orbital path, as well as the concepts behind satellite imaging will be described. Finally, an in-depth discussion of imaging through atmospheric turbulence will be presented and analyzed.

2.1 Mathematical Notation

The mathematical notation to be used throughout this paper is listed in Table 2.1.

2.2 Inertial Navigation

In this section, basic concepts of an inertial navigation system (INS) are discussed, including navigation reference frames, coordinate frame transformation, and functionality and errors associated with strapdown INS sensors.

2.2.1 Basic Concepts . The concept of navigation as a means of determining direction from one place to another has been used for centuries. Navigation can be as simple as following directions on a map by determining position based on one's surroundings. Navigation systems are often developed for vehicles in order to plot, ascertain, and direct the vehicle through land, air, sea or space. One navigation technique uses fixed stars to define a reference frame fixed in space. This reference is commonly referred to as the "inertial" reference frame. Given knowledge of the motion of the Earth and the time of the observation, the navigator is able to use the celestial measurements to define his or her position on the surface of the Earth [24].

Table 2.1: Defined mathematical notation

Type	**Description**	**Example**
Scalars	Scalar variables are designated with italic type	x or X
Vectors	Vectors are denoted by lower case bold type	$\mathbf{x}$
Matrices	Matrices are denoted by uppercase bold type	$\mathbf{X}$
Transpose	The transpose of a vector or matrix is designated with a superscript capital letter T	$\mathbf{x}^T$ or $\mathbf{X}^T$
Estimated Variables	Estimates of random variables are identified with the *hat* character	$\hat{\mathbf{x}}$
Calculated Variables	Variables containing error are denoted with the *tilde* character	$\tilde{\mathbf{x}}$
Direction Cosine Matrix (DCM)	DCMs are designated by a bold capital letter $\mathbf{C}$ with a subscript designating the originating coordinate frame and a superscript as the resulting coordinate frame	$\mathbf{C}_a^b$
Frame of Reference	Vectors expressed in a specific reference frame are annotated with a superscript letter	$\mathbf{r}^a$

2.2.2 Reference Frames. In order to express inertial navigation information in standardized coordinates, fundamental reference frames must be defined relative to an origin and orthogonal axes. Descriptions of the reference frames discussed are as follows, based on those described in Refs. [24] and [25]:

- *The True Inertial Frame* (I-frame) is a theoretical reference frame where Newton's laws of motion apply; therefore, it has no predefined origin or orientation.
- *The Earth-centered Inertial Frame* (i-frame), depicted in Figure 2.1, is an orthogonal reference frame with an origin at the Earth's center of mass and a non-rotating x, y and z axes with respect to fixed stars. For terrestrial navigation purposes, the Earth-centered inertial frame can be considered an inertial reference frame.
- *The Earth-centered Earth-fixed Frame* (e-frame), depicted in Figure 2.2, is an orthogonal reference frame whose origin is also located at Earth's center of

mass. Its x, y and z axes are fixed with respect to the Earth, with the x axis on the equatorial plane pointing toward the Greenwich meridian, the y axis on the equatorial plane pointing toward 90 degrees east longitude, and the z axis aligned with the north pole.

- *The Vehicle-fixed Navigation Frame* (n'-frame), depicted in Figure 2.1, is an orthogonal reference frame with an origin located at a predefined point on a vehicle (usually the vehicle's center of gravity). Its x, y and z axes point in the north, east and down (NED) directions relative to the Earth, respectively. For standardization, down is defined as the direction of the local vertical component of the Earth's gravity vector.
- *The Earth-fixed Navigation Frame* (n-frame), depicted in Figure 2.2, is an orthogonal reference frame with an origin located at a predefined location on the Earth (i.e., Earth's surface). Similar to the n'-frame, its x, y and z axes point in the NED directions relative to the Earth, respectively (where down is defined as the direction of the local vertical component of Earth's gravity vector).
- *The Body Frame* (b-frame), depicted in Figure 2.3, is an orthogonal reference frame aligned with the roll, pitch and yaw axes that point out of a vehicle's nose, right wing and bottom, respectively. Vehicle strapdown inertial navigation systems are referenced in the b-frame. For an orbiting satellite, it is assumed that this frame is equivalent to the n-frame.
- *The Camera Frame* (c-frame), depicted in Figure 2.4, is an orthogonal reference frame rigidly attached to a camera, with origin at the camera's optical center. Its x, y and z axes are oriented up, to the right, and out of the camera, respectively. It will be assumed in this research that the camera is rigidly mounted onto the satellite; therefore, the c-frame will be equivalent to the n-frame.

2.2.3 Coordinate Transformations. Coordinate transformations describe the relationship between two reference frames and are classified as either three- or four-parameter transformations [19,24,25]. In this research, this coordinate transformation

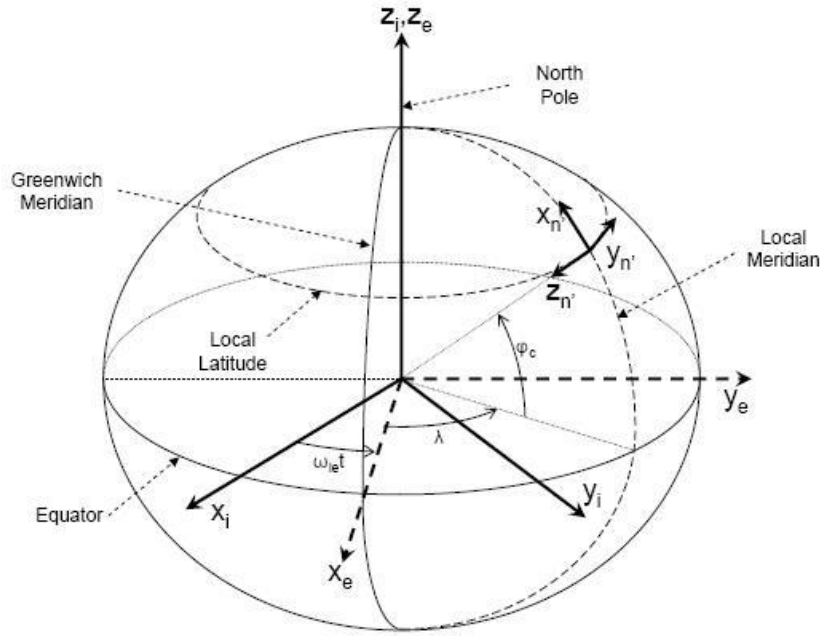

Figure 2.1: Inertial, Earth and Navigation Reference Frames [25].

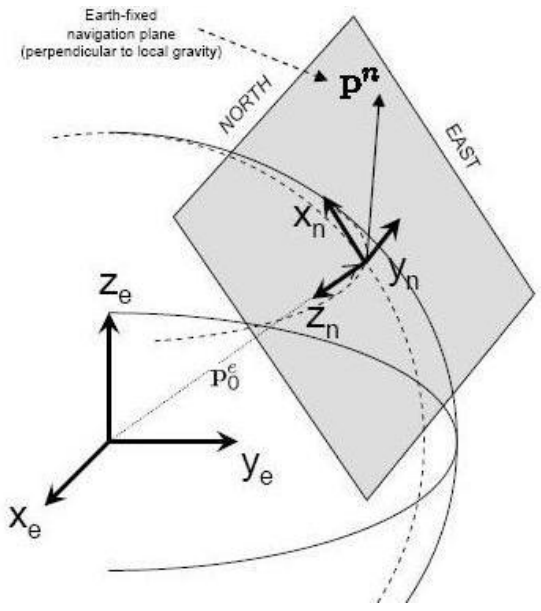

Figure 2.2: Earth-centered, Earth-fixed Navigation Reference Frame [25].

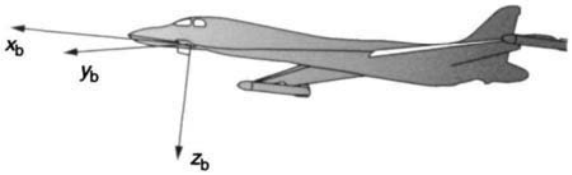

Figure 2.3: Body Reference Frame [24].

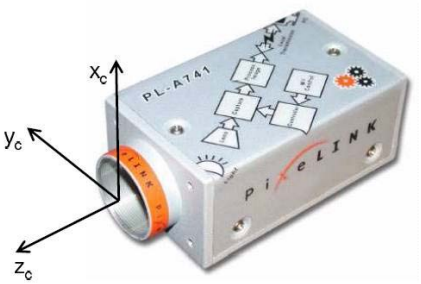

Figure 2.4: Camera Reference Frame [25].

will be the direction cosine matrix (DCM). Since three-parameter coordinate transformations contain a singularity at a pitch angle of 90°, the use of the four-parameter DCM coordinate transformation will be used.

The DCM is a three-by-three matrix representing the unit vector of the originating frame projected along the axis of the resulting frame. The DCM is written in component form as

$$\mathbf{C}_o^r = \begin{bmatrix} c_{11} & c_{12} & c_{13} \\ c_{21} & c_{22} & c_{23} \\ c_{31} & c_{32} & c_{33} \end{bmatrix}. \tag{2.1}$$

The elements c_{ij} represent the cosine of the angle between the i-axis of originating reference frame (o) and the j-axis of the resulting frame (r). The DCM is propagated in time through the equation

$$\dot{\mathbf{C}}_o^r = \mathbf{C}_o^r \boldsymbol{\Omega}_{ro}^o, \tag{2.2}$$

where $\boldsymbol{\Omega}_{ro}^o$ is the skew symmetric form of the angular rate vector $\omega_{ro}^o = [\omega_x \;\; \omega_y \;\; \omega_z]^T$, defined as

$$\mathbf{\Omega}_{ro}^{o} = \begin{bmatrix} 0 & -\omega_z & \omega_y \\ \omega_z & 0 & -\omega_x \\ -\omega_y & \omega_x & 0 \end{bmatrix}. \tag{2.3}$$

This represents the angular turn rate of the originating frame with respect to the resulting frame expressed in the axes of the originating frame.

2.2.4 Navigation Sensors . To more accurately describe inertial navigation, it is the process of establishing the position, velocity, and attitude of a vehicle using information derived from its inertial sensors. Sensors within INS units are often rigidly "fixed" to the moving body, commonly referred to as a strapdown INS system. These sensor devices, namely accelerometers and gyroscopes, are used to measure linear and angular motion, respectively, in the inertial frame. Figures 2.5 and 2.6 illustrate the function of accelerometers and gyroscopes within a strapdown INS system.

Accelerometers are mechanical or electrical sensor systems that use seismic masses and springs to measure translational motion of the platform in which they are located. In other words, accelerometers use simple proof mass physics to measure the total external specific force acting upon itself [24]. Specific force is defined here as the sum of acceleration acting on the body with respect to the inertial reference frame plus gravity. Strapdown IMU systems consist of a triad of accelerometers, usually aligned with the vehicle's body reference frame.

Gyroscopes are the mechanical, electrical, or optical sensor systems used to measure rotational motion in an inertial system [24]. Mechanical gyroscopes rely on the inertial properties of a proof (often spinning) mass for their operation, producing measurements of turn angle or turn rate with respect to inertial space. Similarly, optical gyroscopes provide a measure of angular rate. However, instead of a using a spinning mass to detect rotation, these gyroscopes use interference of laser light, called the Sagnac effect, to detect changes in orientation and spin of the gyroscope. Optical

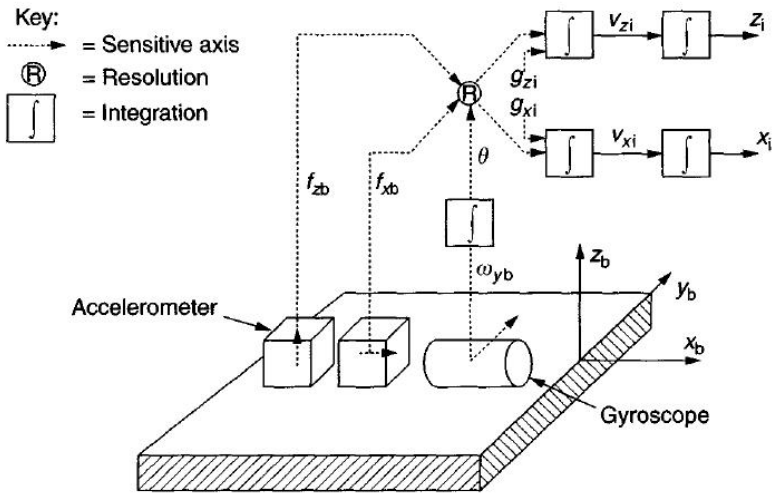

Figure 2.5: A two-dimensional strapdown INS unit [24]. The body attitude, θ, is computed by integrating the measured angular rate, ω_{yb}, and is used to resolve the specific forces, f_{xb} and f_{zb}, into the reference frame.

gyroscopes, such as ring laser gyroscopes, have an advantage over their mechanical counterparts, as there are no moving parts, no inherent drift due to friction, and generally compact in size and lightweight.

As with all real-world IMUs, the measurements from accelerometers and gyroscopes are corrupted by errors. Most of these errors are correctable through factory calibration techniques; however, it is not possible to remove all errors. A brief explanation of these sensor errors, general to both accelerometers and gyroscopes, are listed below [24] [25]:

- *Bias*: Constant or slowly-varying additive error.
- *Scale Factor*: Constant or slowly-varying multiplicative error.
- *Sensor Misalignment*: The result of mechanical fabrication and installation errors made at the factory. These errors result in a difference between the sensor's sensitive axis and the platform reference.
- *Vibration*: Measurement bias as a function of specific vibration(s).

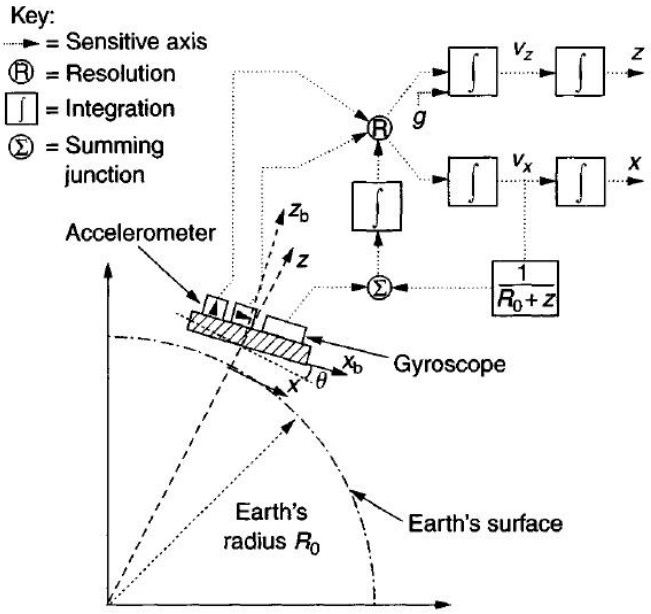

Figure 2.6: A strapdown INS unit in a rotating reference frame [24]. An estimate of the turn rate of the reference frame is derived using the estimated component of horizontal velocity.

- *Measurement Noise*: An additive error component with high-bandwidth power spectral density, such as electrical noise, thermal noise, etc.

2.3 Kalman Filtering

In this section, basic concepts of Kalman filtering are discussed. Two types of Kalman filters will be presented: conventional (for linear navigation states) and extended (for nonlinear navigation states). All equations in Section 2.3 are derived in Refs. [12] and [13].

2.3.1 The Conventional Kalman Filter. The conventional Kalman filter is an efficient recursive filter that estimates the state of a dynamic system from a series of measurements containing random noise [12]. To make the estimation problem tractable, it is assumed that the prior knowledge of the navigation state can be adequately described as a multivariate Gaussian distribution. In addition, the stochastic process noise and additive measurement noise are assumed to be zero-mean, Gaussian

and white, and that the nonlinear state dynamics and measurement equations can be modeled using perturbation techniques.

The Kalman filter state equation, also known as the linear stochastic differential equation, can be written as

$$\dot{\mathbf{x}}(t) = \mathbf{F}(t)\mathbf{x}(t) + \mathbf{B}(t)\mathbf{u}(t) + \mathbf{G}(t)\mathbf{w}(t), \tag{2.4}$$

where $\mathbf{F}(t)$ is the state model applied to the state vector $\mathbf{x}(t_k)$, $\mathbf{B}(t)$ is the control-input model applied to the control vector $\mathbf{u}(t)$, and $\mathbf{G}(t)$ is the noise model applied to the zero mean, white Gaussian process noise vector $\mathbf{w}(t)$ with covariance kernel

$$E[\mathbf{w}(t)\mathbf{w}^T(t+\tau)] = \mathbf{Q}(t)\delta(\tau). \tag{2.5}$$

In Equation (2.5), $\mathbf{Q}(t)$ is the process noise intensity and $\delta(\tau)$ represents the Dirac delta function. The measurement model equation for the Kalman filter is defined at time t_k as

$$\mathbf{z}(t_k) = \mathbf{H}(t_k)\mathbf{x}(t_k) + \mathbf{v}(t_k), \tag{2.6}$$

where $\mathbf{H}(t_k)$ is the observation model applied to the true state vector $\mathbf{x}(t_k)$ and $\mathbf{v}(t_k)$ is the zero-mean, white Gaussian measurement noise process of intensity $\mathbf{R}(t_i)$ in which

$$E[\mathbf{v}(t_i)\mathbf{v}^T(t_j)] = \begin{cases} \mathbf{R}(t_i) & t_i = t_j \\ 0 & t_i \neq t_j. \end{cases} \tag{2.7}$$

The initial conditions of this Kalman filter are characterized by the equations

$$\hat{\mathbf{x}}(t_o) = \hat{\mathbf{x}}_o \tag{2.8}$$

and

$$\mathbf{P}(t_o) = \mathbf{P}_o. \tag{2.9}$$

In Equations (2.8) and (2.9), $\hat{\mathbf{x}}_o$ is defined as the initial measurement estimate vector at initial time t_0 and $\mathbf{P}_o$ is the initial covariance matrix of the form

$$\mathbf{P}_o = E[\delta\mathbf{x}_o \delta\mathbf{x}_o^T], \tag{2.10}$$

where $\delta\mathbf{x}_o$ is the initial state error. The measurement estimate and covariance are propagated forward in time by k iterations using the equations

$$\hat{\mathbf{x}}(t_{k+1}^-) = \Phi(t_{k+1}, t_k)\hat{\mathbf{x}}(t_k^+) + \mathbf{B}_d(t_k)\mathbf{u}(t_k) \tag{2.11}$$

$$\mathbf{P}(t_{k+1}^-) = \Phi(t_{k+1}, t_k)\mathbf{P}(t_k^+)\Phi^T(t_{k+1}, t_k) + \mathbf{G}_d(t_k)\mathbf{Q}_d(t_k)\mathbf{G}_d^T(t_k). \tag{2.12}$$

In Equations (2.11) and (2.12), $\hat{\mathbf{x}}(t_{k+1}^-)$ and $\mathbf{P}(t_{k+1}^-)$ are the propagated state vector and covariance matrix prior to a measurement update, respectively, $\Phi(t_{k+1}, t_k) = e^{\mathbf{F}(t_k)\Delta t}$ is the state transition matrix, $\mathbf{B}_d(t_k)$ is the discrete control-input model, $\mathbf{G}_d(t_k)$ is the discrete noise model and $\mathbf{Q}(t_k)$ is the discrete process noise intensity (calculated using the Van Loan approach or first-order approximation methods [12]). The measurement updates are computed as

$$\mathbf{K}(t_k) = \mathbf{P}(t_k^-)\mathbf{H}^T(t_k)\ [\mathbf{H}(t_k)\mathbf{P}(t_k^-)\mathbf{H}^T(t_k) + \mathbf{R}(t_k)]^{-1} \tag{2.13}$$

$$\hat{\mathbf{x}}(t_k^+) = \hat{\mathbf{x}}(t_k^-) + \mathbf{K}(t_k)\ [\mathbf{z}_k - \mathbf{H}(t_k)\hat{\mathbf{x}}(t_k^-)] \tag{2.14}$$

$$\mathbf{P}(t_k^+) = \mathbf{P}(t_k^-) - \mathbf{K}(t_k)\mathbf{H}(t_k)\mathbf{P}(t_k^-), \tag{2.15}$$

where $\mathbf{K}(t_k)$ is the Kalman gain, $\mathbf{z}_k$ is the measurement, and $\hat{\mathbf{x}}(t_k^+)$ and $\mathbf{P}(t_k^+)$ are the state vector and covariance matrix following the measurement update.

2.3.2 The Extended Kalman Filter . The extended Kalman filter (EKF) is a minimum mean-square-error (MMSE) estimator based upon the first-order approximation Taylor series expansion of the non-linear system dynamics and measurement models [13]. Unlike the conventional Kalman filter, the EKF can handle nonlinear system models and is therefore more applicable in real-world scenarios. The EKF nonlinear stochastic differential equation can be written as

$$\dot{\mathbf{x}}(t) = \mathbf{f}\ [\ \mathbf{x}(t), \mathbf{u}(t), t\ ] + \mathbf{G}(t)\mathbf{w}(t), \tag{2.16}$$

where $\mathbf{f}\ [\ \mathbf{x}(t), \mathbf{u}(t), t\ ]$ is a known model vector of nonlinear functions with respect to the state vector $\mathbf{x}(t)$ and the control-input vector $\mathbf{u}(t)$. $\mathbf{G}(t)$ is the noise model applied to the additive noise vector $\mathbf{w}(t)$.

Rewriting the nonlinear measurement equations in matrix form with respect to the desired navigation states, the discrete-time measurements for the EKF are modeled as a known nonlinear function of the state plus linearly additive measurement noise as

$$\mathbf{z}(t_i) = \mathbf{h}\ [\ \mathbf{x}(t_i), t_i\ ] + v(t_i). \tag{2.17}$$

Given the nonlinear stochastic state and measurement models, the extended Kalman filter can be built. As a starting point, the initial state and covariance conditions at time t_0 are defined with respect to the initial time t_0. They are defined as, respectively,

$$\hat{\mathbf{x}}(t_0/t_0) = \hat{\mathbf{x}}(t_i^+) \tag{2.18}$$

and

$$\mathbf{P}(t_0/t_0) = \mathbf{P}(t_i^+). \tag{2.19}$$

The basic concept of the EKF is to relinearize about each state estimate $\hat{\mathbf{x}}$ once it has been computed. As soon as a new state estimate is made, a new and statistically "better" reference state trajectory is incorporated into the estimation process. With the EKF, it is assumed that deviations from the reference (or nominal) trajectory are small enough to allow linear perturbation techniques to be employed with adequate results.

To achieve the final form of the extended Kalman filter, the most recent nominal $\mathbf{x}_n(t/t_i)$, defined at time t with respect to incremented time t_i, is combined with the state perturbation estimate, $\delta\hat{\mathbf{x}}(t/t_i)$, to generate an estimate of the full state. This assumes the following model is accurate for $\mathbf{x}(t)$:

$$\mathbf{x}(t) = \mathbf{x}_n(t/t_i) + \delta\mathbf{x}(t/t_i). \tag{2.20}$$

The optimal estimate, $\hat{\mathbf{x}}(t/t_i)$, is defined as the sum of the most recent nominal estimate and the optimal estimate of $\delta\mathbf{x}(t)$, denoted as

$$\hat{\mathbf{x}}(t/t_i) = \mathbf{x}_n(t/t_i) + \delta\hat{\mathbf{x}}(t/t_i). \tag{2.21}$$

Since, for the EKF, $\delta\hat{\mathbf{x}}(t/t_i)$ is zero over the entire duration between measurement intervals, the best estimate of the total state over this interval would be the solution to the following

$$\dot{\hat{\mathbf{x}}}(t/t_i) = \mathbf{f}[\ \hat{\mathbf{x}}(t/t_i),\ \mathbf{u}(t),\ t\ ]. \tag{2.22}$$

By calculating the partial derivative of $\mathbf{f}\ [\ \mathbf{x}(t), \mathbf{u}(t), t\ ]$ with respect to the state vector, $\mathbf{x}$, the dynamics partial derivative matrix, $\mathbf{F}[\ t;\ \hat{\mathbf{x}}(t/t_i)\ ]$, is derived as

$$\mathbf{F}[\ t;\ \hat{\mathbf{x}}(t/t_i)\ ] \triangleq \left.\frac{\partial \mathbf{f}\ [\ \mathbf{x}(t), \mathbf{u}(t), t\ ]}{\partial \mathbf{x}}\right|_{\mathbf{x}(t)=\mathbf{x}_n(t/t_i)}. \tag{2.23}$$

It is assumed that $\mathbf{F}[\ t;\ \hat{\mathbf{x}}(t/t_i)\ ]$ is valid and constant with respect to each time interval. Therefore, the transition matrix $\Phi(t_{i+1}, t_i)$ for the stochastic difference equation can be computed for each time interval as

$$\Phi(t_{i+1}, t_i) = e^{\ \mathbf{F}[\ t;\ \hat{\mathbf{x}}(t/t_i)\ ]\ \Delta t} \tag{2.24}$$

$$\delta\mathbf{x}(t_{i+1}) = \Phi(t_{i+1}, t_i)\ \delta\mathbf{x}(t_i) + \mathbf{w}(t_i). \tag{2.25}$$

Similarly, the partial derivative of $\mathbf{h}\ [\ \mathbf{x}(t_i), t_i\ ]$ can be calculated from the measurement equation with respect to the state vector, $\mathbf{x}$. The observation partial derivative matrix, $\mathbf{H}[\ t_i;\ \hat{\mathbf{x}}(t_i^-)\ ]$, is derived as

$$\mathbf{H}[\ t_i;\ \hat{\mathbf{x}}(t_i^-)\ ] \triangleq \left.\frac{\partial \mathbf{h}\ [\ \mathbf{x}(t), t_i\ ]}{\partial \mathbf{x}}\right|_{\mathbf{x}(t)=\hat{\mathbf{x}}(t_i^-)}. \tag{2.26}$$

Next, the estimate is propagated forward to the next sample time t_{i+1} by the following estimate and covariance propagation equations

$$\dot{\hat{\mathbf{x}}}(t/t_i) = \mathbf{f}[\ \hat{\mathbf{x}}(t/t_i),\ \mathbf{u}(t),\ t\ ] \tag{2.27}$$

$$\mathbf{P}(t_{i+1}^-) = \Phi(t_{i+1}, t_i)\mathbf{P}(t_i^+)\Phi^T(t_{i+1}, t_i) + \mathbf{G}_d(t_i)\mathbf{Q}_d(t_i)\mathbf{G}_d^T(t_i), \tag{2.28}$$

where $\mathbf{Q}_d(t_i)$ is the discrete process noise intensity. In Equation (2.28), the conventional Kalman filter covariance equation above is used since it is assumed that $\mathbf{F}[\ t;\ \hat{\mathbf{x}}(t/t_i)\ ]$ remains constant over the time interval. Furthermore, since this equa-

tion is a relatively simple to calculate (unlike the differential equation form that will be seen with the other filters), the overall run time of this filter will be greatly decreased.

Finally, the extended Kalman filter measurement update equations incorporate the measurement by

$$\mathbf{K}(t_i) = \mathbf{P}(t_i^-)\mathbf{H}^T[t_i;\ \hat{\mathbf{x}}(t_i^-)]\left(\mathbf{H}[t_i;\ \hat{\mathbf{x}}(t_i^-)]\mathbf{P}(t_i^-)\mathbf{H}^T[t_i;\ \hat{\mathbf{x}}(t_i^-)] + \mathbf{R}(t_i)\right)^{-1} \tag{2.29}$$

$$\hat{\mathbf{x}}(t_i^+) = \hat{\mathbf{x}}(t_i^-) + \mathbf{K}(t_i)\left(\mathbf{z}_i - \mathbf{h}[\hat{\mathbf{x}}(t_i^-),\ t_i]\right) \tag{2.30}$$

$$\mathbf{P}^+(t_i) = \left(\mathbf{I} - \mathbf{K}(t_i)\mathbf{H}^T[t_i;\ \hat{\mathbf{x}}(t_i^-)]\right)\mathbf{P}(t_i^-), \tag{2.31}$$

where $\mathbf{K}(t_i)$ is the Kalman gain and $\mathbf{I}$ is the identity matrix. Now that the new whole value state estimate $\hat{\mathbf{x}}(t_i^+)$ is defined, it can be used to reset the new, most recent nominal estimate $\mathbf{x}_n(t/t_{i+1})$ and is proceeded to the next propagation set as

$$\mathbf{x}_n(t/t_{i+1}) = \hat{\mathbf{x}}(t_i^+) \tag{2.32}$$

$$\hat{\mathbf{x}}(t/t_{i+1}) = \mathbf{x}_n(t/t_{i+1}) + \delta\hat{\mathbf{x}}(t/t_{i+1}). \tag{2.33}$$

2.4 Orbital Mechanics

Accurately predicting an orbiting satellite's position at any given instant is vital if precise geolocation of ground targets is to be achieved. Satellite tracking can be accomplished by one of two methods: an onboard navigation system, such as INS, or an external tracking system with an onboard receiver, such as GPS. Orbital prediction is often determined several hours (up to 48 hours) in advance and is based on the known orbital parameters of the satellite [15]. In order to fully understand the behavior of satellites orbiting the Earth, an in-depth explanation of orbital mechanics is warranted, including an understanding of Newton's laws, Kepler's laws, Keplerian element transformation, and orbit types.

2.4.1 Newton's Laws . To understand how a satellite travels around a planet, the laws of motion derived by the English scientist Sir Isaac Newton (1642 - 1727) must be analyzed [31]. Based on Newton's second law, that is, the acceleration of the center of a body is proportional to the force applied to that body, this concept can be used with regard to the satellite and the Earth as point mass bodies under gravitational attraction. Although gravitational forces are not the only forces acting upon these bodies, it is by far the largest contributor and is a valid approximation of orbital position prediction [15].

According to Newton, the gravitational force of the Earth onto an orbiting satellite is

$$\mathbf{F} = -\frac{GMm}{r^2}\frac{\mathbf{r}}{r} \tag{2.34}$$

where $G = 6.67 \times 10^{-11}$ N(m/kg)^2 is the Earth's gravitational constant, $M = 5.97 \times 10^{24}$ kg is the mass of the Earth, m is the mass of the satellite in kg, r is the distance between the point masses in km (equaling the radius of the Earth plus the satellite's altitude above the Earth), and $\mathbf{r} = \mathbf{r}_{sat} - \mathbf{r}_{Earth}$ is the position of the satellite relative to the Earth, in a Cartesian coordinate system, in km. The motion of the satellite can therefore be written as a second order differential equation as [19]

$$\ddot{\mathbf{r}} + \frac{G(M+m)}{r^3}\mathbf{r} = 0 \tag{2.35}$$

and can be simplified, since $M \gg m$, to

$$\ddot{\mathbf{r}} + \frac{GM}{r^3}\mathbf{r} = 0 \tag{2.36}$$

where $GM = 3.986 \times 10^8$ m^3/s^3 is the Earth's standard gravitational parameter.

2.4.2 Kepler's Laws . It is well understood that objects orbiting the Earth follow an elliptical pattern. One of first to discover this was the sixteenth-century Ger-

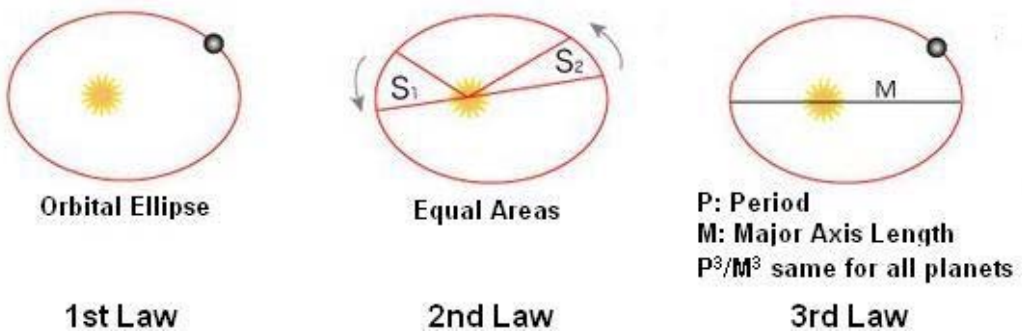

Figure 2.7: Kepler's three laws of planetary motion: orbital ellipse, law of equal areas, and orbits with equal periods [22].

man astronomer Johannes Kepler (1571-1630). Kepler devised the three fundamental laws of planetary motion as follows [22]:

- Planets follow an elliptical orbit with the sun at one of its foci.
- A line joining a planet and the sun sweeps out equal areas during equal intervals of time.
- Two planets with the same semi-major axis length have equal orbital periods.

These laws are summarized in Figure 2.7.

2.4.3 Keplerian Elements . Given knowledge of Kepler's laws of planetary motion under idealized conditions (i.e., a perfect ellipse), the motion of a satellite can be characterized by an elliptical orbit in space with the Earth as one of its foci. This orbit can be specifically identified in three dimensions by six geometrical orbital parameters, known as geometric Keplerian elements [15] [22]. Five of these elements describe the size and shape of the orbit, while the sixth element describes the position of the satellite at a particular instant in time (or "epoch"). The definitions of these six geometric Keplerian elements are listed below, and are depicted in Figure 2.8:

- *Semi-major axis (a)*: The size of the orbit in km, its length is the distance between the geometric center of the orbital ellipse and the apoapsis (point of farthest approach to the central body).

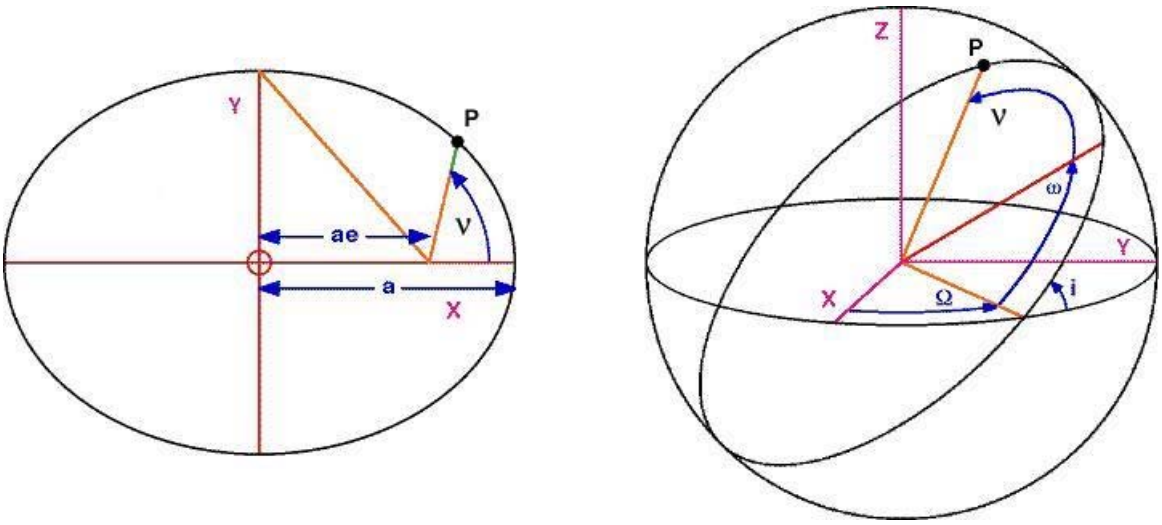

Figure 2.8: The six geometric Keperian orbital elements in two and three dimensions, respectively. The X and Y directions correspond to the semi-major and semi-minor axes of the orbit, respectively. The elements a, e, i, Ω, ω and ν describe the position of the satellite P at a given epoch [22].

- *Eccentricity (e)*: The shape of the orbit. It is a measure of how much the ellipse deviates from a perfect circle (when $e = 0$).
- *Inclination (i)*: The angle between the orbital plane to central body's equator in rad.
- *Right Ascension of the Ascending Node (RAAN or Ω)*: The rotation of orbit's reference plane with respect to ascending node (the point on the satellite's orbit where it crosses the equatorial plane) in rad.
- *Argument of Perigee (ω)*: The angle from the ascending node to perigee (the point at which the satellite is closest to the center of the Earth) in rad.
- *True Anomaly (ν)*: The location of the satellite at a given epoch, this is the angle between the ascending node and the satellite position in the orbital plane in rad.

Given the Keplerian elements, the satellite's orbital period in sec, T_{orb}, and orbital apogee in m, ap_{orb}, (the point in orbit farthest from the Earth) can be deduced as

$$T_{orb} = 2\pi\sqrt{\frac{a^3}{GM}} \tag{2.37}$$

$$ap_{orb} = (1+e)a - R_e, \tag{2.38}$$

where GM is the standard gravitational parameter (see Section 2.4.1) and R_e is the radius of the Earth in m.

2.4.4 Satellite Position and Velocity Transformation . Although it is more common to see the Keplerian elements described in Section 2.4.3 as geometrical characterizations of the orbit itself, these elements also can be represented as the six satellite position and velocity elements in the Cartesian coordinate system [15]. The defined orbital coordinate system is equivalent to the inertial frame (i-frame) in which the origin is located at the elliptical foci located at the center of the Earth. The x and y axes of this reference frame correspond to the semi-major and semi-minor axes of the orbit, respectively, as seen previously in Figure 2.8.

In order to generate the three-dimensional satellite position and velocity vectors, $\mathbf{r}$ and $\mathbf{v}$, in the i-frame, the six geometric Keplerian elements a, e, i, Ω, ω and ν must undergo a reference frame transformation [15]. The magnitude of the orbital radius, $\|\mathbf{r}\|$, or the distance between Earth's center and the satellite, is defined as

$$\|\mathbf{r}\| = \frac{a(1-e^2)}{1+e\cos\nu}. \tag{2.39}$$

The satellite position and velocity vectors in the two-dimensional orbital plane described in Figure 2.8 (denoted here as the pqw-frame), are calculated, respectively, as

$$\mathbf{r}^{pqw} = \begin{bmatrix} \|\mathbf{r}\| \cos(\nu) \\ \|\mathbf{r}\| \sin(\nu) \\ 0 \end{bmatrix} \tag{2.40}$$

and

$$\mathbf{v}^{pqw} = \sqrt{\frac{GM}{a(1-e^2)}} \begin{bmatrix} -\sin(\nu) \\ e + \cos(\nu) \\ 0 \end{bmatrix}. \tag{2.41}$$

Transforming from the pqw-frame to the i-frame, the direction cosine matrix $\mathbf{C}^i_{pqw}$ (see Section 2.2.3) is defined as

$$\mathbf{C}^i_{pqw} = \begin{bmatrix} \cos\Omega\cos\omega - \sin\Omega\sin\omega\cos i & -\cos\Omega\sin\omega - \sin\Omega\cos\omega\cos i & \sin\Omega\sin i \\ \sin\Omega\cos\omega - \cos\Omega\sin\omega\cos i & -\sin\Omega\sin\omega + \cos\Omega\cos\omega\cos i & -\cos\Omega\sin i \\ \sin\omega\sin i & \cos\omega\sin i & \cos i \end{bmatrix}. \tag{2.42}$$

Finally, the satellite position and velocity vectors in the i-frame are calculated, respectively, to be

$$\mathbf{r}^i = \begin{bmatrix} r_x^i \\ r_y^i \\ r_z^i \end{bmatrix} = \mathbf{C}_{pqw}^i \mathbf{r}^{pqw} \tag{2.43}$$

and

$$\mathbf{v}^i = \begin{bmatrix} v_x^i \\ v_y^i \\ v_z^i \end{bmatrix} = \mathbf{C}_{pqw}^i \mathbf{v}^{pqw}. \tag{2.44}$$

2.4.5 Orbit Types . Now that the elliptical orbit of the satellite can be fully characterized as the six satellite position and velocity parameters, a unique elliptical orbit can be designed. Considerations for the satellite's orbit are largely based upon the desired orbital period and apogee (see Section 2.4.3). For comparison, three popular orbital classifications are listed below and depicted in Figure 2.9 [22, 31]:

- *Low Earth Orbit (LEO)*: The orbit closest to the Earth's surface. It lies just beyond the thermosphere (or outer atmosphere). LEO orbits typically have a period of approximately 90 min and an apogee between 450 and 600 km above the Earth's surface. High-resolution imaging satellites and the International Space Station (ISS) are located in this orbit.
- *Geosynchronous Orbit (GEO)*: A high Earth orbit (HEO), a geosynchronous orbit has a period equal to that of Earth's (approximately 24 hrs). Its apogee is approximately 36,000 km above the Earth's surface. A GEO orbit directly above the Earth's equator is known as a geostationary orbit. Communication,

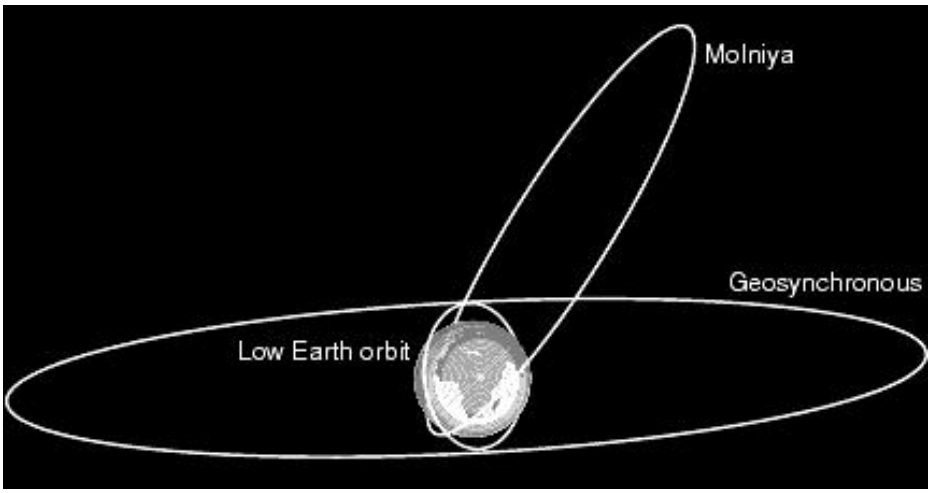

Figure 2.9: Three common satellite orbits: low Earth orbit (LEO), Geosynchronous orbit (GEO), and Molniya orbit (MOL), the last two of which are defined as high Earth orbits (HEOs) [31].

early warning and nuclear detection satellites are located in geosynchronous and geostationary orbits.

- *Molniya Orbit (MOL)*: The Molniya orbit, a HEO orbit named after the Soviet/Russian satellites of the same name, has a unique 12 hr orbit at an approximate 63 deg inclination. With an apogee between 26,000 and 38,000 km above the Earth's surface, a distinct advantage of satellites in MOL orbits is their ability to track locations in the northern hemisphere for an extended period of time, with less ground interference at high look angles than would be true with lower Earth orbits. Communication and intelligence satellites use this orbit.

2.5 Optical Modeling and Spatial Coherence

In this section, the basic physical properties of an optical sensor model are presented, and the concept of spatial coherency is reviewed.

2.5.1 Optical Modeling . An optical sensor is designed to measure the intensity of light entering the device through an aperture and converts it into an electrical signal which can be read by an observer [25, 28]. These sensors typically make use

of either a charge-coupled device (CCD) or complimentary metaloxide semiconductor (CMOS) active-pixel sensor to create a two-dimensional image as a function of light intensity [9].

For the purposes of this research, the world is defined as a collection of real objects of interest that illuminate the world and interact with the other physical objects through various types of reflection. In radiometry, irradiance is defined as the amount of light intensity with respect to unit area that falls on an object's surface [2]. The physical irradiance pattern enters the aperture of the optical sensor (defined as the scene) and is projected onto the image plane. This process is represented as a continuous array of nonnegative real numbers. For simplicity, object surfaces are assumed to be Lambertian, meaning the brightness of the surface to an observer is the same regardless of the observer's angle of view.

A digital optical imaging sensor consists of an aperture, lens, detector array, and sampling array. A simple imaging system model is shown in Figure 2.10. The lens images the scene on the detector array. The light pattern focused on the detector array is defined as the image. The detector array converts the light energy into a voltage or a charge which is converted to a digital value by the sampling array (e.g., an 8-bit digital value within the set [0-255], where 255 represents the highest intensity).

2.5.2 Spatial Coherence. Spatial coherence is defined as the property of waves to maintain definite phase in space. Within the topic of imaging, an understanding of coherence is warranted as it describes the correlation properties of light waves [9]. The constructive addition and destructive subtraction of light waves, known as optical interference, can affect the resulting image clarity, particularly in the presence of atmospheric turbulence.

First, the physical properties of light waves must be characterized. In mathematical terms, the equation for a light wave is defined as a complex field

$$U_g(u,v) = A(u,v)e^{-i\ \phi(u,v)} \tag{2.45}$$

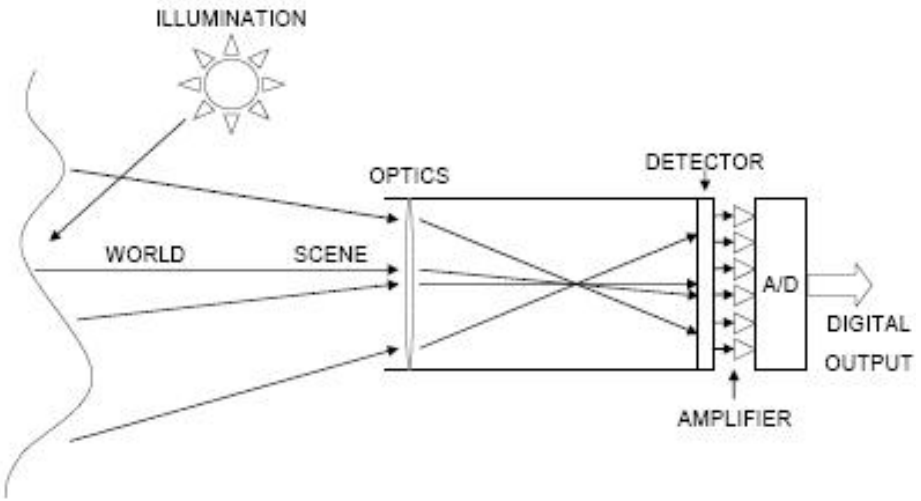

Figure 2.10: A digital optical imaging system, consisting of an aperture, lens, detector array and sampling array [28]. Objects in the world are collected into the aperture (a scene) as an irradiance pattern and focused onto the detector, producing an image represented digitally as an array of nonnegative numbers.

where $A(u, v)$ is the amplitude, $\phi(u, v)$ is the phase and i is the imaginary number. Coherent sources have correlated (non-random) wave phase while incoherent sources have uncorrelated (random) phase [8].

The simulation of coherent and incoherent sources through a lens can be achieved by the means of convolution [8]. This convolution, in which the object forms a spread function region at the image plane, results in a slightly blurred image. This method is depicted in Figure 2.11.

It can be shown that coherent imaging is linear in amplitude while incoherent imaging is linear in intensity, as

$$I_i(u, v) = |h(u, v) \otimes U_g(u, v)|^2 \quad \text{(Coherent Imaging)} \tag{2.46}$$

$$I_i(u, v) = |h(u, v)|^2 \otimes I_g(u, v) \quad \text{(Incoherent Imaging)}, \tag{2.47}$$

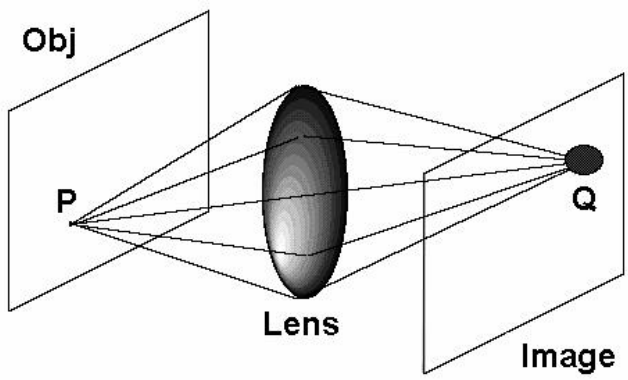

Figure 2.11: Convolution through a lens. An object at point P forms a spread function of region Q, resulting in a slightly blurred image.

where $h(u, v)$ is the amplitude spread function, $|h(u, v)|^2$ is the point spread function, $I_g(u, v)$ is the object intensity, $I_i(u, v)$ is the image intensity, and "$\otimes$" is the convolution operator [8]. For coherent light, image intensity is the squared convolution of the object wave function and the amplitude spread function. For incoherent light, image intensity is the convolution of the object intensity and the point spread function (which is the amplitude spread function squared). The resulting effects of these cases are illustrated with a simple rectangular object pattern in Figure 2.12 [21]. In the case of coherent imaging, the resulting image intensity has a blurred "waffling effect", a phenomenon known as Fresnel ringing, which is the result of optical diffraction [21]. In the case of incoherent imaging, the image intensity distributes evenly, producing images with sharper features than those produced by coherent imaging.

In the case of satellite imaging, the sun is a predominantly incoherent source, meaning the majority of the light rays from the sun have random phase. This results in nearly uniform phase distribution on the image plane as light from the sun bends around the edges of the object (or objects) in the object plane. Therefore, image blurring as the result of Fresnel ringing is not of concern.

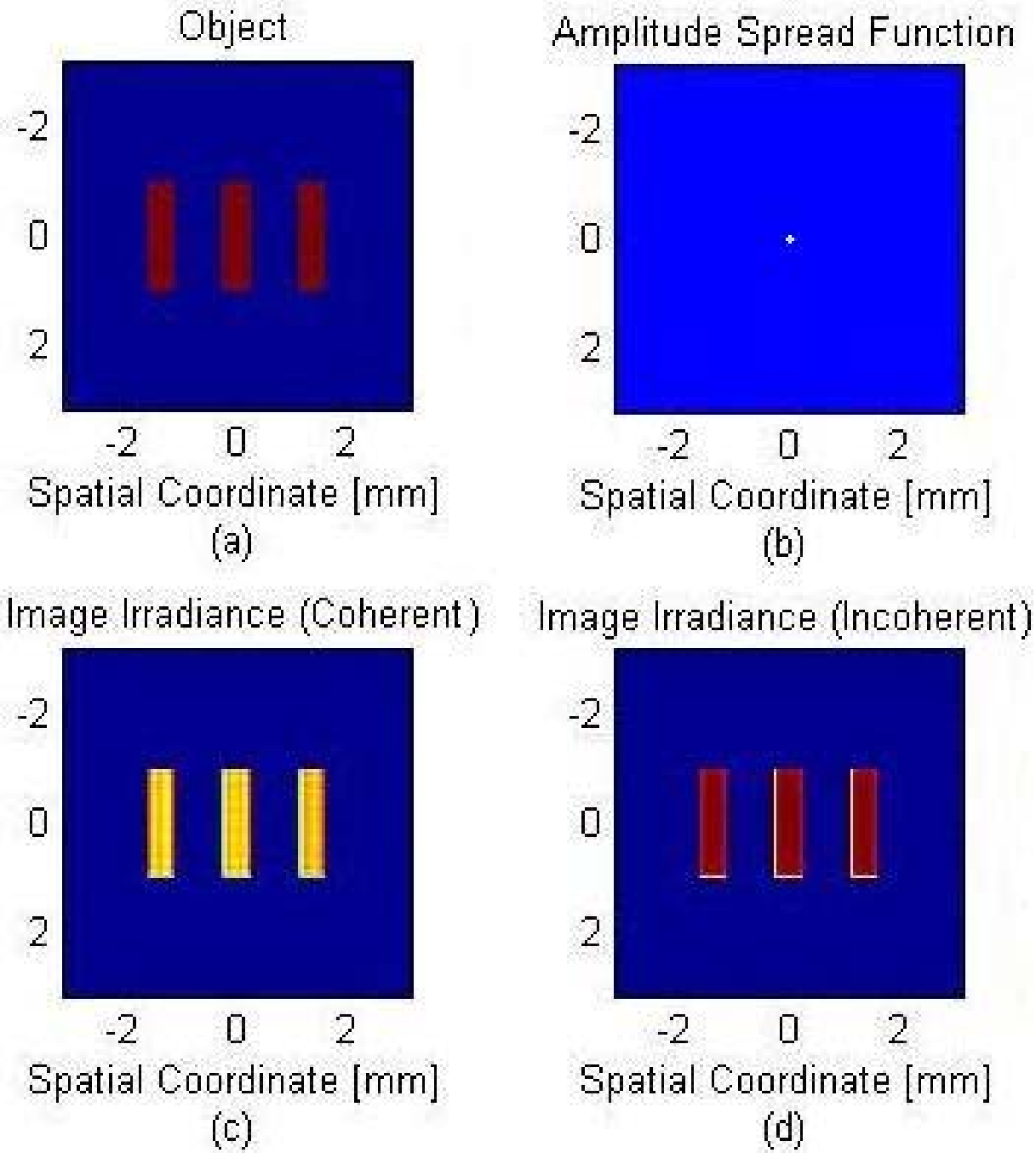

Figure 2.12: Coherent and incoherent imaging with a rectangular pattern. The object (a) is convolved with the amplitude (or point spread) function (b) to produce either a coherent image (c) or incoherent image (d). Note the blurred "waffle effect" in (c), the result of optical diffraction [21].

2.6 Imaging Through Turbulence

Ground images are continuously captured from space by orbiting observation satellite systems. When these images are collected from a satellite several kilometers above the Earth's surface, it is likely that image resolution and image displacement will be affected by the atmosphere. In order to understand the turbulent effects on an image collected through the atmosphere, a background of turbulence theory must be presented. Following this background, the concepts and derivations of the turbulence strength parameter, C_n^2 is defined. The atmospheric coherence width, r_0, among other important turbulence parameters, will then be discussed in light of the problem at hand. Unless stated otherwise, all equations in Section 2.6 are derived in Ref. [1].

2.6.1 Turbulence Background . The Earth's atmosphere is comprised of gases, chemicals and water vapor, all contributing to refractive index fluctuations, causing light waves to bend and scatter (or attenuate) unpredictably. The refractive index of the Earth's atmosphere is near unity, however, as light propagates through this medium, the optical waves become randomly distorted and the resulting image resolution becomes limited [21].

Atmospheric turbulence is the result of stochastic variations in temperature and velocity within the Earth's atmosphere [21]. This turbulence is caused by a combination of solar heating the surface and atmosphere, convection (causing hot air to rise and cold air to fall) and diffusion (mixing areas of high concentration and areas low concentration). An illustration of the atmospheric layers is depicted in Figure 2.13. The largest concentration of turbulence is within the first 20 to 24 km above the surface [1]. It is assumed in this analysis that weather conditions are clear with no obstruction due to clouds, rain or fog.

2.6.2 Turbulence Strength . The index of refraction, n, is one of the most significant parameters with respect to light wave propagation through the atmosphere [1]. Fluctuations in atmospheric refractive index are related to corresponding fluctuations

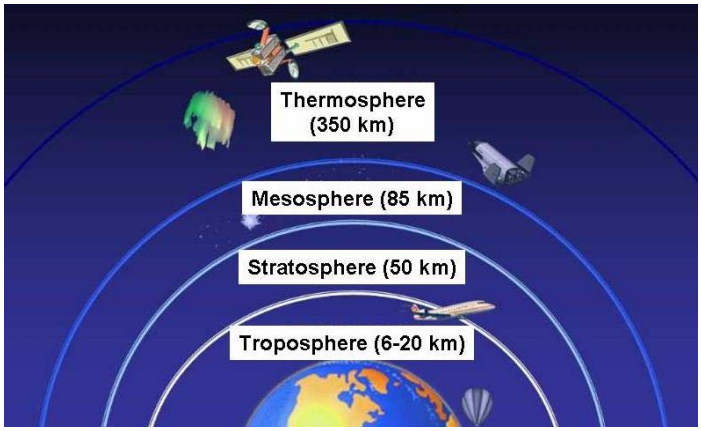

Figure 2.13: The Earth's atmospheric layers. Nearly 100% of the atmospheric mass is contained within the troposphere and stratosphere, the majority of which is contained solely within the troposphere.

in temperature, T (measured in K), and pressure, P (measured in millibars), and can be written accordingly as

$$n(\mathbf{R}) = 1 + 79 \times 10^{-6} \frac{P(\mathbf{R})}{T(\mathbf{R})}, \tag{2.48}$$

where $\mathbf{R}$, assigned as any point in space, is bounded by the inertial subrange, or the range of unstable air masses (eddies) defined by the inner scale bound l_o and outer scale bound L_o as $[l_o \ll \mathbf{R} \ll L_o]$. For this research, the Kolmogorov turbulence spectrum will be assumed; therefore, the inertial subrange is unbounded.

The statistical description of the random turbulence-induced fluctuations in the atmosphere's refractive index can be expressed as a structure function with respect to $\mathbf{R}$. Assuming statistically homogeneous and isotropic turbulence ($R = |\mathbf{R}_1 - \mathbf{R}_2|^2$), the structure function, $D_n(R)$, is expressed as

$$D_n(R) = \begin{cases} C_n^2 \, l_o^{-4/3} \, R^2 & 0 \leq R \ll l_o \\ C_n^2 \, R^{2/3} & l_o \ll R \ll L_o, \end{cases} \tag{2.49}$$

where C_n^2 is the refractive index structure parameter. C_n^2 is a measure of the strength of fluctuations in the refractive index, and can be interpreted as a measure of the strength

of atmospheric turbulence. C_n^2 is quantified in terms of pressure, P, temperature, T and the temperature structure constant, C_T^2, by

$$C_n^2 = \left(79 \times 10^{-6} \frac{P}{T^2}\right)^2 C_T^2. \tag{2.50}$$

The associated power spectral density for refractive index fluctuations, over the inertial subrange defined by $[1/L_o \ll \kappa \ll 1/l_o]$, is defined by

$$\Phi_n(\kappa) = 0.0033 C_n^2 \kappa^{-11/3}. \tag{2.51}$$

C_n^2 is known to vary as a function of height above ground, the strongest occurring during the daytime near the ground (on an order of $10^{-13}\mathrm{m}^{-2/3}$ or higher). In order to express the turbulent strength as a function of height, models for both C_n^2 and atmospheric winds must be assigned. The Bufton wind model is commonly used to describe the atmospheric winds as

$$V(z) = v_G + \omega_s z \cos\zeta_Z + v_T \exp\left[-\left(\frac{z\cos\zeta_Z - H_T}{L_T}\right)^2\right]\left[\sin^2\phi + \cos^2\phi\cos^2\zeta_Z\right]^{1/2}, \tag{2.52}$$

where z is the propagation slant path (in m) given by the equation $z = h\sec\zeta$, where h is the height above ground in m and ζ is the zenith angle in rad. The zenith angle angle assignment is depicted in Figure 2.14. Furthermore, $v_G = 5$ m/s is assigned as the ground wind speed, $\omega_s = 0$ deg/s as the turbulent slew rate, $v_T = 30$ m/s as the tropopause wind speed, $H_T = 12.5$ km as the average altitude of the tropopause, $L_T = 4.8$ km as the average thickness of tropopause and $\phi = 0$ deg as the direction of wind speed [1].

Using the Bufton wind model in Equation (2.52), the root mean square (RMS) wind speed due to turbulence is calculated to be

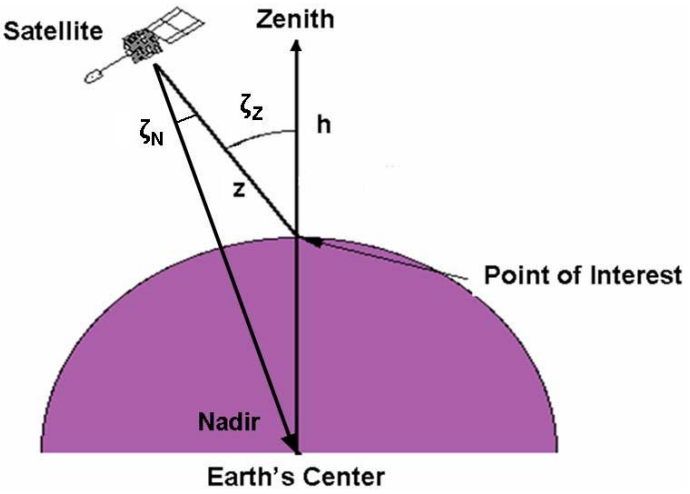

Figure 2.14: Zenith and nadir viewing angles, ζ_Z and ζ_N, respectively. The relationship of slant path, z, with respect to altitude, h, is $z = h \sec \zeta$ [21].

$$v_{rms} = \left[\frac{1}{15 \times 10^3} \int_{6\times10^3}^{20\times10^3} V^2(z)\, dz \right]^{1/2}, \tag{2.53}$$

where the integration limits in Equation (2.53) encompass the troposphere defined in Figure 2.13.

Finally, the Hufnagel-Valley (H-V) 5-7 model, commonly used to describe C_n^2, is defined as [1]

$$\begin{aligned} C_n^2(h) = 0.00594 \left(\frac{v_{rms}}{27}\right)^2 (10^{-5}\ h)^{10} \exp\left(\frac{-h}{1000}\right) \\ +2.7 \times 10^{-16} \exp\left(\frac{-h}{1500}\right) + A \exp\left(\frac{-h}{100}\right), \end{aligned} \tag{2.54}$$

where $h = z \cos\zeta$, $A = 1.7 \times 10^{-14}$ m$^{-2/3}$, and $v_{rms} = 21$ m/s from Equation (2.53). Note that A is the nominal value of C_n^2 at the ground (or $C_n^2(0)$). Using the H-V C_n^2 model, a comparison of the turbulent strength, C_n^2 as a function of propagation distance, z, and zenith angle, ζ, can be seen in Figure 2.15.

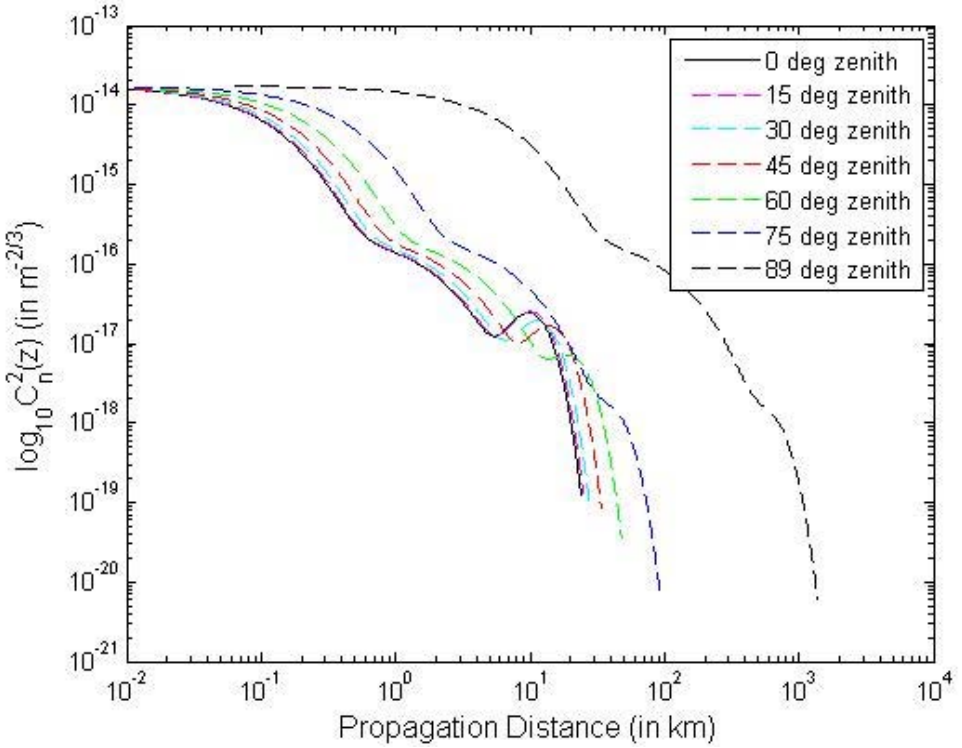

Figure 2.15: Turbulence strength, C_n^2, as a function of propagation distance, z, and zenith angle, ζ_Z. As ζ_Z increases, the relative height above ground decreases to where turbulence is greatest, contributing to higher C_n^2 for longer durations.

2.6.3 Atmospheric Coherence Width . The atmospheric coherence width, r_0, also called Fried's parameter, is the measure of the spatial coherence of light at the receiver. A large r_0 implies that light is coherent across large distances, indicating good imaging system performance [1,21]. Since turbulent strength, C_n^2, is nonlinear in nature, the direction of propagation can greatly affect the resulting coherence width.

Consider two distinct paths of a propagating point source, producing a spherical wave at the source that becomes a planar wave over a large propagation distance (such as the case between the Earth's surface and an orbiting satellite). In the first case, an uplink path is defined in which the atmosphere is farthest from the receiver (i.e., an imaging system in orbit). In the second case, a downlink path is defined in which the turbulent atmosphere is nearest the receiver (i.e., for an imaging system on the ground). The resulting coherence width of the uplink path, onto the satellite receiver, is many times larger than the satellite itself. This large coherence width is due to the sun's incoherent light, reflected from the ground, bending appreciably early in the propagation path (when the wave's spatial extent is small) and remaining essentially unchanged as it propagates toward the satellite. The opposite is true for the relatively small coherence width of the downlink path, in which the wave's spatial extent is large when entering the turbulent atmosphere and remains turbulent as it propagates toward the ground [6, 7]. An illustration of these two cases can be seen in Figure 2.16.

For a satellite imaging system, in which light is propagated from the ground (the transmitter) to the satellite (the receiver), the uplink path is assigned. For coherence width computation, it is necessary to identify the statistical path moments of the optical system. The uplink propagation first and second path moments are, respectively,

$$\mu_{1u} = \int_{h_0}^{H} C_n^2(h) \left[\Theta + \bar{\Theta}\ \xi\right]^{5/3} dh \tag{2.55}$$

$$\mu_{2u} = \int_{h_0}^{H} C_n^2(h) \left(1 - \xi\right)^{5/3} dh, \tag{2.56}$$

where h is the the elevation in km, $h_0 = 0$ is the elevation of the ground (at sea level), H is the elevation of the satellite in km, and $\xi = (h - h_0)/(H - h_0)$ is the normalized distance variable. The output (receiver) beam curvature parameter, Θ, equals one for a spherical wave. Therefore, $\bar{\Theta} = 1 - \Theta = 0$. The resulting coherence width for the uplink path, r_{0_u}, is defined as

$$r_0 = \left[0.42 \sec(\zeta_N) k^2 \left(\mu_{1u} + 0.622 \mu_{2u} \Lambda^{11/6}\right)\right]^{-3/5} \tag{2.57}$$

$$= \left[0.42 \sec(\zeta_N) k^2 \mu_{1u}\right]^{-3/5}. \tag{2.58}$$

Since the output (receiver) Fresnel ratio parameter, Λ, equals zero for a spherical wave case, Equation (2.57) is simplified to Equation (2.58). Note that, for the uplink case, the viewing angle, ζ_N, is with respect to nadir at the satellite, pointing downward. As expected, r_0 for the uplink case will be much larger than for the downlink case. This result implies good imaging system performance for an observation satellite collecting images of the ground.

2.6.4 Image Jittering . An on-axis object may appear to wander within a satellite image due to atmospheric turbulence. This frequent shifting (or displacement) of the object, otherwise known as "image jittering" is associated with the angle of arrival fluctuations of an optical wave onto the receiver aperture [1,32]. These angle of arrival fluctuations, $< \beta_a^2 >$, are defined primarily by turbulence at high altitudes, and are related to the coherence width of the propagation path (see Section 2.6.3).

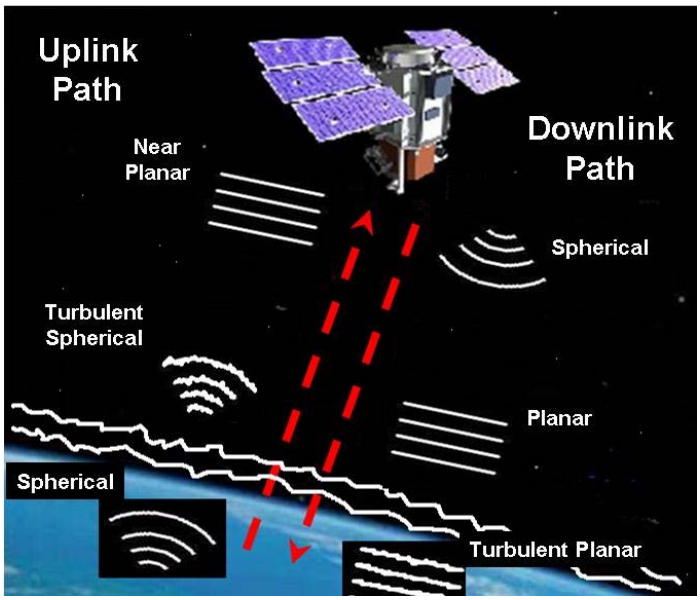

Figure 2.16: Uplink and downlink path scenarios for a propagating point source (spherical wave). Note the effects of free-space diffraction in the uplink case, providing minimal atmospheric turbulence effects and ultimately a large coherence width at the receiver (the satellite) [21].

The RMS angle of arrival for an uplink path, in rad, simplified for a spherical wave, is calculated as

$$< \beta_a^2 >= 2.91 \mu_{1u} \sec(\zeta_N) (D_G)^{-1/3}, \tag{2.59}$$

where D_G is the aperture diameter of the receiver in m. The resulting image displacement standard deviation (or "image jitter"), in m, is calculated to be

$$\sigma_{imag} = f_{lens} \sqrt{< \beta_a^2 >}, \tag{2.60}$$

where f_{lens} is the focal length of the lens in m. The variance of the angle of arrival fluctuations in rad, σ_a^2, which attributes to reduction in image resolution, is calculated as

$$\sigma_a^2 = 6.88 (r_0)^{-5/3} \sec(\zeta_N) (D_G)^{-1/3} k^{-2}, \tag{2.61}$$

where r_0 is the uplink coherence width in m and k is the wave number in rad/m. In the uplink case, σ_{imag} and σ_a^2 are very small, since r_0 is very large. Assuming an off-nadir angle of less than 25 deg for LEO orbits, and an angle of less than 5 deg for HEO orbits, atmospheric turbulence due to image jittering can generally be ignored with respect to an observation satellite.

2.6.5 Atmospheric Refraction . In free space, light waves propagate in straight lines due to the fact that their dielectric permittivity, ϵ_0, and magnetic permeability, μ_0, are constant in space and time relative to the speed of wave propagation c as defined by the following formula [8]

$$c = (\mu_0 \epsilon_0)^{-1/2}. \tag{2.62}$$

However, the dielectric permittivity of the atmosphere, ϵ, is greater than that of free space ($\epsilon > \epsilon_0$). Therefore, light waves propagate at a speed ν that less than c and in doing so deviate from straight propagation paths, resulting in refraction (or bending) of the beam [5]. This results in a non-uniform atmospheric refraction, n, that is greater than unity with respect to the Cartesian coordinate $x-$, $y-$ and $z-$directions, or [8]

$$n(x, y, z) = \frac{c}{\nu} > 1. \tag{2.63}$$

Therefore, in order to determine the true path of the light wave, atmospheric refraction must be considered.

According to Ref. [1], the refractive index of the atmosphere can be closely approximated as a function of optical wavelength, λ (in m), pressure, P (in mbars), and temperature, T (in K). Assuming the non-uniform lower atmospheric density is limited to within 20 km of the surface, P and T are analyzed as a function of altitude, z (in km). From [5], pressure in the lower atmosphere is calculated to be

$$P(z) = \| - (2.26 \times 10^{-5} z - 1)^{5.32 \times 10^3} \|, \quad 0 \leq z \leq 20 \text{ km}. \tag{2.64}$$

Likewise, temperature in the lower atmosphere is computed as

$$T(z) = \begin{cases} -6.81 \times 10^{-3}(z-1) + 293, & 0 \leq z \leq 11 \text{ km} \\ 218, & 11 < z \leq 20 \text{ km}. \end{cases} \tag{2.65}$$

Finally, the atmosphere's refractive index, n, can be written in terms of optical wavelength, λ (in m), pressure, P (in millibars), and temperature, T (in K), as [1]

$$n(z) = 1 + 77.6 \times 10^{-6}(1 + 7.52 \times 10^{-3}\lambda^{-2})\frac{P(z)}{T(z)}, \quad 0 \leq z \leq 20 \text{ km}. \tag{2.66}$$

Figure 2.17 depicts the plot of pressure, temperature and refractive index, with respect to altitude.

Next, Snell's law [9] is used to calculate the ground-to-satellite horizontal displacement due to light refraction. Snell's law is defined as

$$n_1 \sin\theta_1 = n_2 \sin\theta_2 = n_3 \sin\theta_3, \tag{2.67}$$

where n_1, n_2 and n_3 are the refractive indices of the troposphere, tropopause and free space, respectively. This relationship can be seen in Figure 2.18. Given a known off-zenith departure angle θ_1, the sequential angles θ_2 and θ_3 can also be computed. Using geometry, the horizontal displacement Δx_n can be calculated as

$$\begin{aligned} \Delta x_n &= x_w - x_{wo} && (2.68) \\ &= (z_{w1}\tan\theta_{w1} + z_{w2}\tan\theta_{w2} + z_{w3}\tan\theta_{w3}) - z_{w0}\tan\theta_{wo}, && (2.69) \end{aligned}$$

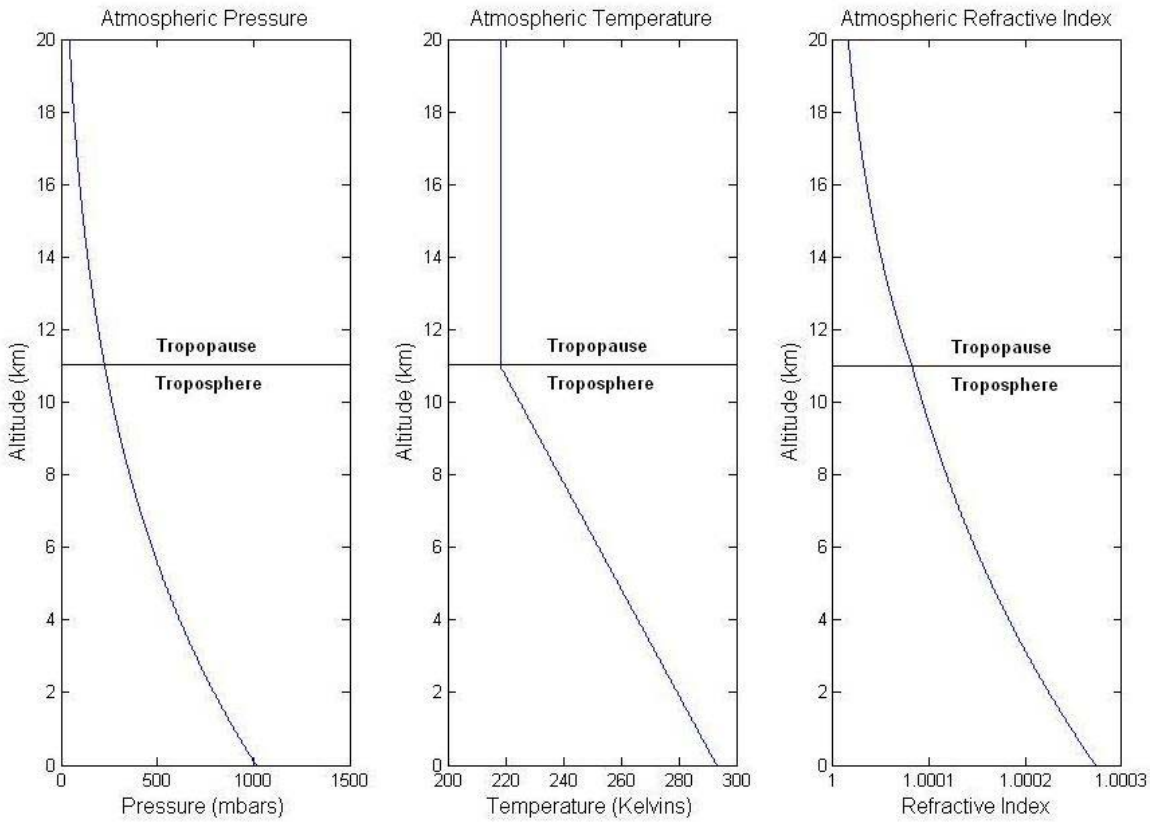

Figure 2.17: Pressure, temperature and refractive index, with respect to altitude, at a wavelength of 675 nm. Between 11-20 km, temperature remains steady through the tropopause. Above an altitude of 20 km, it is assumed that turbulence is negligible, and therefore is approximately where free space begins ($n \simeq 1$).

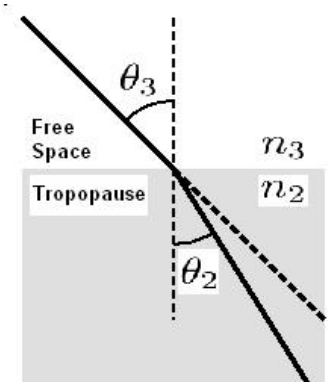

Figure 2.18: The refraction of a light wave through the tropopause (n_2) to free space (n_3). Since the index of refraction decreases to approximately 1 at altitudes above the tropopause ($n_3 < n_2$), light waves refract to a greater extent, resulting in a larger departure angle in free space ($\theta_3 > \theta_2$)

where x_w is the total horizontal displacement from the surface to the satellite including atmospheric refraction and x_{wo} is the horizontal displacement from the surface to the satellite without atmospheric refraction. Assuming an off-nadir angle of less than 25 deg for LEO orbits, and an angle of less than 5 deg for higher orbits, the effects of atmospheric refraction is found to be minimal.

2.7 Image-Aided Navigation

In previous research [25, 27], it has been demonstrated that the coupling of imaging with inertial sensors has provided a navigation improvement of at least two orders of magnitude over inertial systems without the aid of optical devices. As such, knowledge of the navigation state (i.e., position, velocity, and attitude) of a space vehicle could also be improved by using image-aided navigation, provided that optical measurements from an imaging sensor pointed toward the ground are available. This section will summarize the background behind image-aided navigation, review a means of matching a satellite image to predefined image template, and introduce the concept of georeferencing in order to identify a targets location on a relative coordinate system.

2.7.1 General Background . Although advances in the field of image-aided navigation have been made, the level of accuracy in such a system is critically determined by the alignment and calibration of the imaging sensor [23]. Previous approaches, including mechanical techniques and field-calibrated estimation based techniques [11], have had limited success, requiring dedicated equipment unsuitable for field work and being subject to intermittent manufacturer errors.

Other more recent approaches use real-time estimators and use the field of visible stars to provide the reference for the optical system [29]. No operator involvement or external equipment is required in this stellar observation approach. Additionally, star observation accounts for time-varying errors prominent in inertial sensors (see Section 2.2.4) and has the advantage of operating in real time. An example of such a spacecraft navigation system includes the high accuracy star tracker (HAST) [14]. However, stellar observations require visibility of the sky and star tracking algorithms must be sensitive enough to resolve the location of celestial objects. Additionally, if an onboard imaging system has the combined role of star tracking as well as Earth observation, the ability to track both star and ground targets may be limited.

2.7.2 Image Matching . Image matching is used in many applications, including object recognition, stereo matching, and feature tracking, as a means of identifying a feature or area common among a series of pixelated images [3]. Image-aided navigation can benefit from image matching algorithms by incorporating matched image data between subsequent images to determine how a stationary target "wanders" between those images.

Image matching applications used for feature tracking commonly use the sum-of-squared-difference (SSD) measure to determine the best match between subsequent images [16]. The SSD method operates directly on the pixelated irradiance pattern of the image (see Section 2.5.1) and measures the correspondence between an image and a template (in which a match of the original image exists). Knowledge of the maximum position uncertainty of the feature of interest within the template allows

the image matching to be performed efficiently with greatest likelihood of determining a unique image match.

The SSD can be computed as [3]

$$SSD(u,v) = \sum_{x=0}^{n}\sum_{y=0}^{n}\left[f(x,y) - t(x-u+d_x, y-v+d_y)\right]^2 \tag{2.70}$$

where f is the satellite image and t is the template in which the image is to be matched within. The summation is over the Cartesian coordinates (x, y), corresponding to the northern and eastern directions in the n-frame, respectively. A template with northern and eastern boundary limit parameters, u and v, form a "window" with respect to the origin (the origin is assumed to be in the center of the image). Disparities d_x and d_y are the vertical and horizontal differences between images in the n-frame, respectively, and are sometimes used to determine depth or distance of an object within the image [17]. Low SSD values represent a good match between the image and template, indicating where the difference between the image and template is minimal. In Equation (2.70), the differencing between the image and template is squared to ensure that SSD results are always non-negative.

Although the sum-of-squared-difference has the advantage of being relatively simplistic and easy to implement, weaknesses of SSD also exist. This method is sensitive to outliers and is not accustomed to template variations, such as those that occur at occluding boundaries in the image [16]. Since SSD is restricted to overlapping the entire image over the template, this algorithm can be easily "fooled" by repeated patterns throughout the template, resulting in increasing probability of erroneous matching. This weakness is especially inherent to indoor navigation, in which repeatable features (i.e., flooring and ceiling tiles) are common. Fortunately, this problem is not as prevalent with outdoor navigation and satellite imagery, where feature repeatability, particularly at higher resolutions, is rare.

Figure 2.19: Georeferenced control points with unique features are used to georegister a target in a satellite image to a reference map (image provided by Manifold Systems).

2.7.3 Georeferencing . Georeferencing is the process of identifying a target's location on a coordinate system relative to the Earth. The process of georeferencing a target onto a reference map is depicted in Figure 2.19, where pre-assigned feature-rich control points within the image are used to "georegister" (or adjust) a target to a geographic location based upon a known reference map. This process is known as georegistration. The target's georeferenced location (measured in *e*-frame latitude/-longitude coordinates) is referred to as the target's geolocation.

A georeferenced image can be used to measure the coordinates of a target of interest within an image. However, inaccurate geolocation can limit this capability, for example, if an insufficient number of control points are available to accurately determine the target's location. Large satellite attitude errors characterized by a low-performance inertial sensors can also limit geolocation performance.

Tightly coupled image-aided inertial navigation systems have been designed to extract navigation information of the satellite by automatically detecting and tracking stationary optical features of opportunity in the environment, thereby vastly reducing the vehicle's attitude errors [26]. One significant advantage of this navigation system is that it can operate in areas where GPS is either denied or unavailable.

2.8 Stochastic Constraints

Using an imaging sensor to determine the navigation states from optical measurements depends upon tracking the target location through a series of images. Target recognition through image interpretation, however, can be very inefficient and time consuming if the number false matches are not limited and the feature correspondence search is not constrained. Therefore, the stochastic projection method developed in Refs. [28,30], which constrains this correspondence search by area by incorporating a priori knowledge of the satellite navigation states, allows the user to accurately and optimally predict the pixel location and uncertainty of a target feature in a series of images.

As mentioned in Ref. [30], this stochastic projection method uses many of the assumptions of the Kalman filter in Section 2.3.1. The landmark of interest is assumed to be stationary (or very slowly moving) with respect to the surface of the Earth. Additionally, the camera is assumed to be rigidly mounted to the vehicle with a known alignment and calibration. Finally, it is assumed that the terrain is flat (constant elevation). All equations in Section 2.8 are derived in Ref. [30].

Given the navigation state at time t_i, $\mathbf{x}(t_i)$, described in Equation (2.4), the landmark position corresponding to a pixel location, $\mathbf{y}(t_i)$, is a non-linear function of $\mathbf{x}$, given by

$$\mathbf{y}(t_i) = \mathbf{g}\ [\mathbf{x}(t_i)]. \tag{2.71}$$

The calculated landmark position, $\tilde{\mathbf{y}}(t_i)$, is modeled as a perturbation about the true position as

$$\tilde{\mathbf{y}}(t_i) = \mathbf{y}(t_i) + \delta\mathbf{y}(t_i), \tag{2.72}$$

where $\tilde{\mathbf{y}}(t_i)$ is a function of the calculated navigation state, $\tilde{\mathbf{x}}(t_i)$. $\tilde{\mathbf{x}}(t_i)$ is also modeled as a perturbation about truth, and is of the form

$$\tilde{\mathbf{x}}(t_i) = \mathbf{x}(t_i) + \delta\mathbf{x}(t_i). \tag{2.73}$$

Applying perturbation techniques to the landmark position function, the landmark error, $\delta\mathbf{y}(t_i)$, can be expressed as a linear function of the navigation state errors

$$\delta\mathbf{y}(t_i) = \mathbf{G}_{yx}(t_i)\delta\mathbf{x}(t_i), \tag{2.74}$$

where the influence coefficient, $\mathbf{G}_{yx}(t_i)$, is defined as

$$\mathbf{G}_{yx}(t_i) = \left.\frac{\partial \mathbf{g}\ [\mathbf{x}(t_i)]}{\partial \mathbf{x}(t_i)}\right|_{\mathbf{x}(t_i)=\tilde{\mathbf{x}}(t_i)}. \tag{2.75}$$

The landmark error covariance, $\mathbf{P}_{yy}(t_i)$, and cross-correlation, $\mathbf{P}_{xy}(t_i)$, are defined as

$$\mathbf{P}_{yy}(t_i) = E[\delta\mathbf{y}(t_i)\delta\mathbf{y}^T(t_i)] \tag{2.76}$$

$$\mathbf{P}_{xy}(t_i) = E[\delta\mathbf{x}(t_i)\delta\mathbf{y}^T(t_i)]. \tag{2.77}$$

Substituting Equation (2.74) into Equation (2.76) yields

$$\mathbf{P}_{yy}(t_i) = \mathbf{G}_{yx}(t_i)\mathbf{P}_{xx}(t_i)\mathbf{G}_{yx}^T(t_i). \tag{2.78}$$

The cross correlation matrices are calculated in a similar manner as

$$\mathbf{P}_{xy}(t_i) = \mathbf{P}_{xx}(t_i)\mathbf{G}_{yx}^T(t_i) \tag{2.79}$$

$$\mathbf{P}_{yx}(t_i) = \mathbf{G}_{yx}(t_i)\mathbf{P}_{xx}(t_i). \tag{2.80}$$

Combining the navigation state with the landmark state through augmentation, the initial combined state vector, $\mathbf{x}^{\star}(t_o)$, and initial combined covariance matrix, $\mathbf{P}^{\star}(t_o)$, are defined, respectively, as

$$\mathbf{x}^{\star}(t_o) = \begin{bmatrix} \mathbf{x}(t_o) \\ \\ \mathbf{y}(t_o) \end{bmatrix} \tag{2.81}$$

and

$$\mathbf{P}^{\star}(t_o) = \begin{bmatrix} \mathbf{P}_{xx}(t_o) & \mathbf{P}_{xy}(t_o) \\ \\ \mathbf{P}_{yx}(t_o) & \mathbf{P}_{yy}(t_o) \end{bmatrix} \tag{2.82}$$

Likewise, the combined psuedonoise matrix, $\mathbf{G}^{\star}(t_i)$, is expressed as

$$\mathbf{G}^{\star}(t_i) = \begin{bmatrix} \mathbf{G}_x(t_i) & 0 \\ \\ 0 & \mathbf{G}_y(t_i) \end{bmatrix} \tag{2.83}$$

and the combined process noise intensity, $\mathbf{Q}^{\star}(t_i)$, is expressed as

$$\mathbf{Q}^{\star}(t_i) = \begin{bmatrix} \mathbf{Q}_x(t_i) & 0 \\ \\ 0 & \mathbf{Q}_y(t_i) \end{bmatrix}. \tag{2.84}$$

$\mathbf{G}_y(t_i)$ defines the landmark error dynamics as a random walk by

$$\delta\dot{\mathbf{y}}(t_i) = \mathbf{G}_y(t_i)\mathbf{w}_y(t_i), \tag{2.85}$$

and $\mathbf{w}_y(t_i)$ is a zero-mean, white Gaussian noise process with covariance kernel

$$E[\mathbf{w}_y(t_i)\mathbf{w}_y^T(t_i+\tau)] = \mathbf{Q}_y(t_i)\delta(\tau). \tag{2.86}$$

For propagating the combined navigation and landmark estimate, the EKF nonlinear stochastic differential equation is expressed as

$$\dot{\mathbf{x}}^\star(t/t_i) = \mathbf{f}\,[\,\mathbf{x}^\star(t/t_i), \mathbf{u}^\star(t), t\,] + \mathbf{G}^\star(t_i)\mathbf{w}(t_i), \tag{2.87}$$

in which the dynamics of the landmark state within $\mathbf{x}^\star(t/t_i)$ are zero. Therefore, the respective partial derivative dynamics matrices for the navigation and landmark state are derived as

$$\mathbf{F}_x[\,t;\ \hat{\mathbf{x}}(t/t_i)\,] \triangleq \left.\frac{\partial \mathbf{f}\,[\,\mathbf{x}, \mathbf{u}_x(t), t\,]}{\partial \mathbf{x}}\right|_{\mathbf{x}=\mathbf{x}_n(t/t_i)} \tag{2.88}$$

$$\mathbf{F}_y[\,t;\ \hat{\mathbf{y}}(t/t_i)\,] \triangleq \left.\frac{\partial \mathbf{f}\,[\,\mathbf{y}, \mathbf{u}_y(t), t\,]}{\partial \mathbf{y}}\right|_{\mathbf{y}=\mathbf{y}_n(t/t_i)=0}, \tag{2.89}$$

and the combined partial derivative dynamics matrix is written as

$$\mathbf{F}^\star[\,t;\ \hat{\mathbf{x}}^\star(t/t_i)\,] = \begin{bmatrix} \mathbf{F}_x[\,t;\ \hat{\mathbf{x}}(t/t_i)\,] & 0 \\ 0 & \mathbf{F}_y[\,t;\ \hat{\mathbf{y}}(t/t_i)\,] \end{bmatrix}. \tag{2.90}$$

The pixel location measurements for the EKF are modeled as a known nonlinear pixel projection function of the combined state plus linearly additive measurement noise as

$$\mathbf{z}(t_i) = \mathbf{h}\,[\,\mathbf{x}^\star(t_i), t_i\,] + v(t_i), \tag{2.91}$$

such that the pixel location measurements are a function of the combined navigation and landmark state. The respective partial derivative pixel projection matrices are then derived as

$$\mathbf{H}_{zx}[\ t_i;\ \hat{\mathbf{x}}(t_i^-)\ ] \triangleq \left.\frac{\partial \mathbf{h}\ [\ \mathbf{x}, t_i\ ]}{\partial \mathbf{x}}\right|_{\mathbf{x}=\hat{\mathbf{x}}(t_i^-)} \tag{2.92}$$

$$\mathbf{H}_{zy}[\ t_i;\ \hat{\mathbf{y}}(t_i^-)\ ] \triangleq \left.\frac{\partial \mathbf{h}\ [\ \mathbf{y}, t_i\ ]}{\partial \mathbf{y}}\right|_{\mathbf{y}=\hat{\mathbf{y}}(t_i^-)}, \tag{2.93}$$

and the combined partial derivative pixel projection matrix is written as

$$\mathbf{H}^{\star}[\ t_i;\ \hat{\mathbf{x}}^{\star}(t_i^-)\ ] = \begin{bmatrix} \mathbf{H}_{zx}[\ t_i;\ \hat{\mathbf{x}}(t_i^-)\ ] & 0 \\ 0 & \mathbf{H}_{zy}[\ t_i;\ \hat{\mathbf{y}}(t_i^-)\ ] \end{bmatrix}. \tag{2.94}$$

Finally, the the covariance of the pixel location errors can be written as the EKF residual covariance computed within the Kalman gain (Equation (2.30)) as

$$\mathbf{P}_{zz}(t_i) = \mathbf{H}^{\star}[\ t_i;\ \hat{\mathbf{x}}^{\star}(t_i^-)\ ]\mathbf{P}^{\star}(t_i^-)\mathbf{H}^{\star T}[\ t_i;\ \hat{\mathbf{x}}^{\star}(t_i^-)\ ] + \mathbf{R}(t_i). \tag{2.95}$$

Therefore, given the pixel coordinates of a stationary ground landmark at time t_i, the predicted pixel coordinates of the same landmark at time t_{i+1} can be described by the pixel location error covariance, $\mathbf{P}_{zz}(t_i)$, as a function of the combined navigation and landmark state covariance, $\mathbf{P}^{\star}(t_i)$, the pixel projection matrix, $\mathbf{H}^{\star}[\ t_i;\ \hat{\mathbf{x}}^{\star}(t_i^-)\ ]$, and the measurement noise intensity, $\mathbf{R}(t_i)$.

III. Method

In this chapter, the modeling and methodology of a satellite-based image-aided navigation system will be covered, using concepts covered in the previous chapter. First, two satellite trajectories, one low-Earth orbit and one high-Earth orbit, will be produced. Next, modeling of the satellite system will be developed, including the vehicle's imaging system parameters as well as identifying system-level noise parameters. The ground image model will be constructed, using the defined satellite trajectory and noise parameters, as well as existing satellite imagery. Image matching and georeferencing techniques will be implemented to predict the landmark state. Finally, an extended Kalman filter model will be presented.

3.1 Orbit Modeling

One of the first steps in developing an image-aided navigation system for an orbiting satellite is the understanding of the satellite's trajectory around the Earth. This requires knowledge of the satellite's position and velocity, both of which are computed from this trajectory.

In order to prove orbital independence of this satellite-based system, two orbit types, one LEO and one HEO (specifically, a MOL), will be produced. Descriptions of these orbits can be found in Section 2.4.5. Using geometric Keplerian orbital elements defined in Section 2.4.3, both orbits are characterized. The basis of this element assignment may be dependent upon orbit requirements for the system, such as a specified orbital period or orbital apogee (see Equations (2.37) and (2.38)). It should be noted that these orbit declarations are assumed to be nominal and are not corrupted by error. The parameters assigned for the low Earth and Molniya orbits of this satellite are represented in Table 3.1.

3.2 Satellite System Modeling

Provided the assigned Keplerian orbit elements mentioned in Section 3.1, the initial conditions for all navigation and landmark states of this satellite navigation

Table 3.1: Assigned nominal Keplerian elements for a typical LEO and MOL. Using these elements, the orbital period and apogee were calculated.

Keplerian Element	**LEO**	**MOL**
a (km)	6,760	26,600
e	0.0323	0.704
i (rad)	1.71	1.10
Ω (rad)	5.97	3.60
ω (rad)	5.46	4.92
ν (rad)	3.12	1.36
T_{orb} (hrs)	1.54	12.0
ap_{orb} (km)	598	38,900

system can be defined. These nominal parameters will later provide a basis for the true navigation and landmark states (where error corruption will be introduced).

3.2.1 Nominal System State Modeling . First, the initial position and velocity navigation states for the nominal satellite system dynamics are defined in the three-dimensional Cartesian coordinate system. Using Equations (2.39) through (2.44), presented in Section 2.4.4, the position vector in the i-frame, r_x, r_y, and r_z (in units of km) and velocity vector in the i-frame, $\dot{r_x}$, $\dot{r_y}$, and $\dot{r_z}$ (in units of km/min), are computed from the geometric Keplerian elements presented in Table 3.1.

Next, the initial attitude states of the satellite in the n-frame, ϕ and θ, that being the pitch and roll angles of the satellite imaging system measured in rad, are assumed to nominally be zero. In other words, it is assumed that initially the satellite's imaging sensor is pointed directly at the target of interest on the ground. For simplicity, it is assumed that the x- and y-axes of the satellite image (in the n-frame) are always aligned with respect to the true latitude and longitude axes of the Earth, respectively; therefore, image rotation is not of concern and the yaw angle of the satellite need not be estimated.

Table 3.2: Initial nominal LEO and MOL navigation and landmark states at apogee, with respect to their respective i and n-frames. The initial navigation states, $r_{x_{nom0}}$, $r_{y_{nom0}}$, $r_{z_{nom0}}$, $v_{x_{nom0}}$, $v_{y_{nom0}}$, and $v_{z_{nom0}}$, are derived using Keplerian orbital element transformation. Assuming the satellite's imaging sensor is pointed directly at the target, the initial attitude states, ϕ_{nom0} and θ_{nom0}, and the initial landmark states, $t_{nx_{nom0}}$ and $t_{ny_{nom0}}$, are considered to be zero.

Initial Conditions	**LEO**	**MOL**
$r_{x_{nom0}}$ (km)	-4,710	17,100
$r_{y_{nom0}}$ (km)	780	-13,900
$r_{z_{nom0}}$ (km)	5,080	39,600
$v_{x_{nom0}}$ (km/min)	-300	81.2
$v_{y_{nom0}}$ (km/min)	139	50.0
$v_{z_{nom0}}$ (km/min)	-299	-17.3
ϕ_{nom0} (rad)	0	0
θ_{nom0} (rad)	0	0
t_{nxnom0} (pixels)	0	0
t_{nynom0} (pixels)	0	0

Finally, the initial n-frame landmark states for the system are defined as the northern and eastern target position errors on the ground, t_{nx} and t_{ny}. Since this state measurement is based upon the resolution of the satellite image, it is calculated in units of pixels (see Section 2.5.1 for details diffraction-based imaging). Similar to the attitude states, the nominal landmark states are initially assumed to be zero, again implying the satellite's imaging sensor is pointed directly at the target of interest on the ground. For the derived low Earth and Molniya orbits, the satellite navigation and landmark states at apogee are represented in Table 3.2.

3.2.2 Satellite System Dynamics . The navigation and landmark state dynamics equations can now be presented. Rewriting Equation (2.36) from Section 2.4.1, the satellite's acceleration vector in the i-frame, $\ddot{\mathbf{r}}$, can be computed as

$$\ddot{\mathbf{r}} = -\frac{GM}{\| \mathbf{r} \|^3}\mathbf{r} + \mathbf{w}_{\ddot{\mathbf{r}}}(t), \tag{3.1}$$

where GM is the Earth's standard gravitational parameter (approximately 398,600 km^3/min^2), $\| \mathbf{r} \|$ is the magnitude of the satellite's position vector and $\mathbf{w}_{\ddot{\mathbf{r}}}(t)$ is uncorrelated, zero-mean, white, Gaussian noise source with

$$E[\mathbf{w}_{\ddot{\mathbf{r}}}(t)\mathbf{w}_{\ddot{\mathbf{r}}}(t)^T(t+\tau)] = q_{\ddot{\mathbf{r}}}(t)\delta(\tau). \tag{3.2}$$

The randomized displacement of the satellite image in the n-frame as a result of variations in the attitude of the imaging sensor (assume to be rigidly fixed to the satellite body) can be described as a first-order time-correlated drift. This drift can be characterized as a first-order Gauss-Markov process [12], in which the satellite's rate of pitch and rate of yaw, respectively, can written as

$$\dot{\phi} = -\frac{1}{\tau_\phi}\phi + \mathbf{w}_{\dot{\phi}}(t) \tag{3.3}$$

$$\dot{\theta} = -\frac{1}{\tau_\theta}\theta + \mathbf{w}_{\dot{\theta}}(t), \tag{3.4}$$

where τ_ϕ and τ_θ are the first-order Gauss Markov time constants of the roll and pitch angle in arcmin, respectively, and $\mathbf{w}_{\dot{\phi}}(t)$ and $\mathbf{w}_{\dot{\theta}}(t)$ are uncorrelated, zero-mean, white, Gaussian noise sources with

$$E[\mathbf{w}_{\dot{\phi}}(t)\mathbf{w}_{\dot{\phi}}(t)^T(t+\tau)] = q_{\dot{\phi}}(t)\delta(\tau) \tag{3.5}$$

$$E[\mathbf{w}_{\dot{\theta}}(t)\mathbf{w}_{\dot{\theta}}(t)^T(t+\tau)] = q_{\dot{\theta}}(t)\delta(\tau). \tag{3.6}$$

As explained in Section 2.8, the landmark state vector will be used to accurately predict the pixel location of a target. As such, t_{nx} and t_{ny} will be defined as a

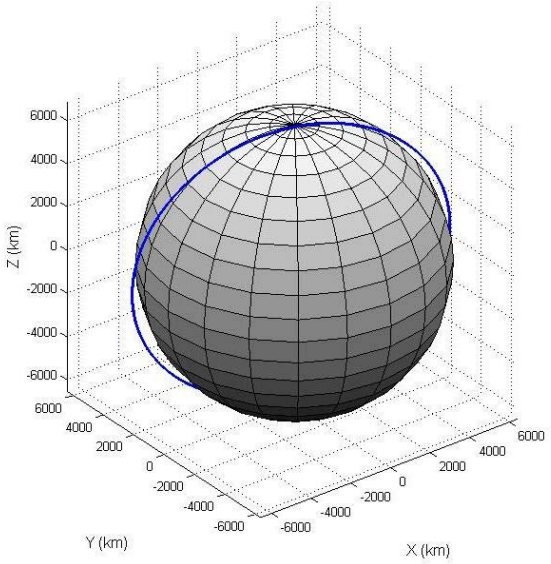

Figure 3.1: Generated nominal satellite trajectory in a LEO.

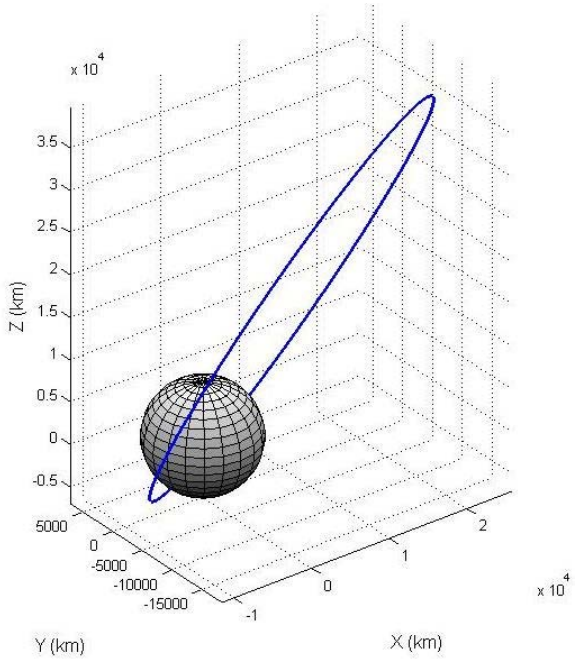

Figure 3.2: Generated nominal satellite trajectory in a MOL.

stochastic projection of the navigation states, and will therefore have no dynamics. In other words,

$$\dot{\mathbf{t}}_n = 0 + \mathbf{w}_{\mathbf{t}_n}(t), \tag{3.7}$$

where $\mathbf{w}_{\mathbf{t}_n}(t)$ is uncorrelated, zero-mean, white, Gaussian noise source with

$$E[\mathbf{w}_{\mathbf{t}_n}(t)\mathbf{w}_{\mathbf{t}_n}(t)^T(t+\tau)] = q_{\mathbf{t}_n}(t)\delta(\tau). \tag{3.8}$$

Using the initial conditions found in Table 3.2 and the defined satellite system dynamics expressed in Equations (3.1) through (3.7), the nominal low-Earth and Molniya orbits are generated. The resulting path of the satellite's position in each orbit is depicted in Figures 3.1 and 3.2.

Table 3.3: Assigned imaging parameters for an observation satellite, for both LEO or MOL orbits. A high apogee in the MOL orbit results in higher image resolution, PX, a smaller maximum off-nadir angle, $\eta_{N_{max}}$, and smaller *view angle* (the maximum angle at which the image can be viewed). Since similar imaging systems will be used for either orbit, the operating wavelength, λ, lens diameter, D_{lens} and lens focal length, f_{lens}, will not vary.

Imaging Parameters	**LEO**	**MOL**
PX (km/pix)	0.1	1.0
$\zeta_{N_{max}}$ (deg)	25	5.0
view angle (deg)	0.4	0.2
λ (nm)	675	675
D_{lens} (m)	0.60	0.60
f_{lens} (m)	10	10

It is assumed that the optimal operation time of the satellite is when it reaches its orbital apogee, since it is at that location in orbit where the satellite travels at its slowest rate (as dictated by Kepler's 2nd law in Section 2.4.2) and therefore the satellite is able to capture as many images of the target of interest as possible within the designated off-nadir angle limits.

3.2.3 Image System Modeling . Based on an appropriate imaging system suitable for either LEO or MOL orbits [4, 18, 20], the observation satellite's assigned imaging parameters are represented in Table 3.3.

It will be assumed that the designed LEO orbit with an apogee of 598 km will have an image resolution, PX, of less than 1 km/pixel (perhaps on the order of 0.1 km/pixel), whereas the MOL orbit with an apogee of 38,900 km will likely have a PX of no better than 1 km/pixel. Likewise, the satellite's off-nadir angle, $\eta_{N_{max}}$, and maximum angle at which the image can be viewed, *view angle*, will likely be much larger for a satellite in a LEO orbit versus that in a MOL orbit, is the satellite's location is orders of magnitude closer to the Earth's surface in the lower orbit. For simplicity, it will be assumed that all other imaging system parameters would be

sufficient for either orbit. Therefore, its operating wavelength, λ, lens diameter, D_{lens} and lens focal length, f_{lens}, will remain unchanged.

3.3 Noise Modeling

It is unreasonable to assume that the nominal image-aided satellite navigation system described in Section 3.2 would not be corrupted by real-world errors. Such errors could include measurement noise due to sensor misalignment (Section 2.2), trajectory noise due to atmospheric drag (Section 2.4), image sensor noise due to vehicle vibration (Section 2.5), or image displacement (or fluctuation) due to atmospheric turbulence (Section 2.6).

3.3.1 Turbulence Noise . Errors due to atmospheric turbulence are identified in order to determine if these errors are significant enough to model in the satellite system. As discussed in Section 2.6, it is already assumed that these errors will be minimal in even the worst case scenarios (i.e., when the off-nadir angle $\zeta_N = \zeta_{N_{max}}$). For completeness, however, these calculations are warranted.

From Sections 2.6.4 and 2.6.5, it was shown that target location errors due to turbulence may exist due to image jitter and horizontal light refraction displacement. Using Table 3.3, and Equations (2.60) and (2.69), the resulting image jitter, σ_{img}, and refraction displacement, Δx_n, are summarized in Table 3.4.

As expected, at minimum off-nadir angles ($\zeta_N = 0$), turbulence error due to image jitter and refraction displacement are insignificant in either orbit. At maximum off-nadir angles ($\zeta_N = \zeta_{N_{max}}$), σ_{img} is again insignificant, and Δx_n is approximately 0.5 pixels (with respect to image resolution) for either orbit. It can be deduced that for uplink propagation at relatively high altitudes above the lower atmosphere (i.e., the case of an imaging sensor onboard an orbiting satellite), image jitter is not found to be of concern, and image displacement due to refraction is only of slight concern when off-nadir angles approach their maximum limit. As such, for completeness, very

Table 3.4: Image position error due to turbulence in LEO and MOL orbits. At minimum off-nadir angles ($\zeta_N = 0$), image jitter, σ_{img}, and refraction displacement, Δx_n, are practically non-existent for either orbit. At maximum off-nadir angles ($\zeta_N = \zeta_{N_{max}}$), σ_{img} is again very small, and Δx_n is only a half a pixel (with respect to image resolution) in either case.

Error due to Turbulence	**LEO**	**Molniya**
σ_{img} at $\zeta_N = 0$ (pixels)	4.8×10^{-12}	1.0×10^{-34}
σ_{img} at $\zeta_N = \zeta_{N_{max}}$ (pixels)	5.0×10^{-12}	1.1×10^{-34}
Δx_n at $\zeta_N = 0$ (pixels)	0	0
Δx_n at $\zeta_N = \zeta_{N_{max}}$ (pixels)	0.54	0.56

slight additive error will be introduced in the attitude and landmark states, as listed in the following section.

3.3.2 Image Sensor, Trajectory and Measurement Noise . As mentioned earlier in Section 3.3, space vehicles, as well as their onboard hardware, are subject to errors as a result of real-world noise sources, including vehicle vibration, atmospheric drag and measurement miscalibration, just to name a few. In order to model these errors in a recursive estimator (such as the extended Kalman filter derived in Section 2.3.2), these noise sources are all assumed to be zero-mean, Gaussian and white. For the purpose of modeling, these assumptions are assumed to be reasonable. With this in mind, careful consideration must be given as to the numerical assignment of these noise sources.

The assigned initial statistical and process noise parameters for the designed LEO and MOL orbits are summarized in Tables 3.5 and 3.6, respectively. Given faster satellite trajectories, larger off-nadir angles and higher atmospheric effects in a LEO orbit, it is reasonable to assume that all initial uncertainties be an order of magnitude smaller and all process noise strengths be at least an order of magnitude larger than they would be in a MOL orbit. An exception would be the time constants, τ_ϕ and τ_θ, since the rate of image sensor drift is independent to the altitude of the

Table 3.5: Assigned initial statistical parameters for a satellite in LEO and MOL orbits. Faster satellite trajectories, larger off-nadir angles and higher atmospheric effects in the LEO orbit justify these parameters to be an order of magnitude smaller than they would be in the MOL orbit, with the exception of the independent time constants, τ_ϕ and τ_θ.

Statistical Parameters	**LEO**	**MOL**
$\sigma_{r_{x0}}$, $\sigma_{r_{y0}}$, $\sigma_{r_{z0}}$ (km)	0.5	0.05
$\sigma_{v_{x0}}$, $\sigma_{v_{y0}}$, $\sigma_{v_{z0}}$ (km/min)	0.05	0.005
σ_{ϕ_0}, σ_{θ_0} (rad)	5×10^{-4}	5×10^{-5}
τ_ϕ, τ_θ (min)	10	10
$\sigma_{t_{nx}meas}$, $\sigma_{t_{ny}meas}$ (pix)	0.5	0.05

Table 3.6: Assigned process noise parameters for a satellite in LEO and MOL orbits. Faster satellite trajectories, larger off-nadir angles and higher atmospheric effects in the LEO orbit justify these parameters to be at least an order of magnitude larger than they would be in the MOL orbit.

Noise Parameters	**LEO**	**MOL**
$q_{\ddot{r}_x}$, $q_{\ddot{r}_y}$, $q_{\ddot{r}_z}$ (km^2/min^2)	5×10^{-4}	5×10^{-6}
$q_{\dot{\phi}}$, $q_{\dot{\theta}}$ (min^{-1})	5×10^{-8}	5×10^{-10}
$q_{\dot{t}_{nx}}$, $q_{\dot{t}_{ny}}$ (pix^2/min)	10	0.1

satellite. Note that all initial statistical parameters are relatively small since it is assumed that a navigation system calibration had just recently occurred.

It should be noted that the satellite roll and pitch rate noise strengths, $q_{\dot{\phi}}$ and $q_{\dot{\theta}}$, are both first-order Gauss-Markov processes as described in Section 3.2.2. Accordingly, these values are calculated as

$$q_{\dot{\phi}} = 2\frac{{\sigma_{\phi_0}}^2}{\tau_\phi} \tag{3.9}$$

$$q_{\dot{\theta}} = 2\frac{{\sigma_{\theta_0}}^2}{\tau_\theta}. \tag{3.10}$$

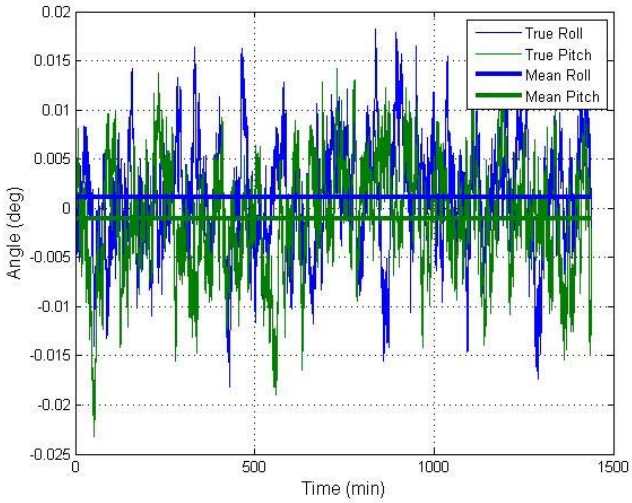

Figure 3.3: Generated true satellite attitude error, as first-order Gauss-Markov processes [12]. In this particular example, an imaging system in a MOL orbit is modeled over a 24 hour period. As a first-order Gauss-Markov process, the mean diverges toward zero at a rate relative to the time constants τ_ϕ and τ_θ.

The results of this first-order Gauss-Markov process, that being the true satellite attitude states, ϕ_{true} and θ_{true}, are plotted in Figure 3.3. The nominal roll and pitch are assumed to be zero for all time (with no optical drift).

Furthermore, the combined process noise intensity matrix, $\mathbf{Q}^\star$, including both navigation and landmark states, is

$$\mathbf{Q}^{\star} = \begin{bmatrix} (q_{\ddot{r}_x})^2 & 0 & 0 & 0 & 0 & 0 & 0 \\ 0 & (q_{\ddot{r}_y})^2 & 0 & 0 & 0 & 0 & 0 \\ 0 & 0 & (q_{\ddot{r}_z})^2 & 0 & 0 & 0 & 0 \\ 0 & 0 & 0 & (q_{\dot{\phi}})^2 & 0 & 0 & 0 \\ 0 & 0 & 0 & 0 & (q_{\dot{\theta}})^2 & 0 & 0 \\ 0 & 0 & 0 & 0 & 0 & (q_{\dot{t}_{nx}})^2 & 0 \\ 0 & 0 & 0 & 0 & 0 & 0 & (q_{\dot{t}_{ny}})^2 \end{bmatrix}. \tag{3.11}$$

Likewise, the measurement noise intensity matrix, $\mathbf{R}$, in pixels, is described as

$$\mathbf{R} = \begin{bmatrix} (\sigma_{t_{nx}meas})^2 & 0 \\ 0 & (\sigma_{t_{ny}meas})^2 \end{bmatrix}. \tag{3.12}$$

The pixel location measurement in the n-frame, a function of both the navigation and landmark states, is calculated as

$$\Delta\mathbf{z}_{meas} = \begin{bmatrix} \Delta x_{meas} \\ \Delta y_{meas} \end{bmatrix} = \begin{bmatrix} t_{nx} - \frac{d_o\phi}{PX} & 0 \\ 0 & t_{ny} - \frac{d_o\theta}{PX} \end{bmatrix}, \tag{3.13}$$

and where the slant range in the e-frame, d_o, from the satellite to the ground target coordinates (x_{oe}, y_{oe}, z_{oe}), is computed as

$$d_o = \sqrt{(r_x - x_{oe})^2 + (r_y - y_{oe})^2 + (r_z - z_{oe})^2}. \tag{3.14}$$

3.4 Ground Error Modeling

Given the assigned satellite trajectory and noise parameters, a ground image model can be constructed using existing satellite imagery. A three-hundred square mile image of the greater Cincinnati, Ohio area, provided by the National Aeronautics and Space Administration (NASA) Landsat satellite [10], is assigned to represent the area of the Earth where the satellite is tracking the target of interest. It is assumed that the satellite is at or near its apogee so that the target tracking duration is maximized. In order to accurately represent the capabilities of a satellite image sensor in either LEO or Molniya orbits, the resolution of the image, PX, must be considered. For simplicity, identical images of the area are used for either orbit, one in which $PX = 0.1$ km/pixel (or 10 pixels/km) to represent the satellite in a low Earth orbit, and one where $PX = 1$ km/pixel to represent the satellite in a Molniya orbit. A sample of the image template (the area in which the subsequent satellite images will be captured within), at a resolution of 1 km/pixel, is depicted in Figure 3.4.

In order to generate the truth data for the landmark state, t_{nxtrue} and t_{nytrue}, a full understanding on the landmark error is necessary. Rationally, target error should be a function of the trajectory of the satellite (as the satellite moves across the sky above the target) as well as a function of the time-correlated attitude errors affecting the image sensor (as described in Section 3.3.2). This combination will be assumed in order to produce the desired truth data for the landmark state.

The northern and eastern true target position errors of the satellite in the n-frame, t_{nxorb} and t_{nyorb}, solely as a function of orbital drift, are defined as

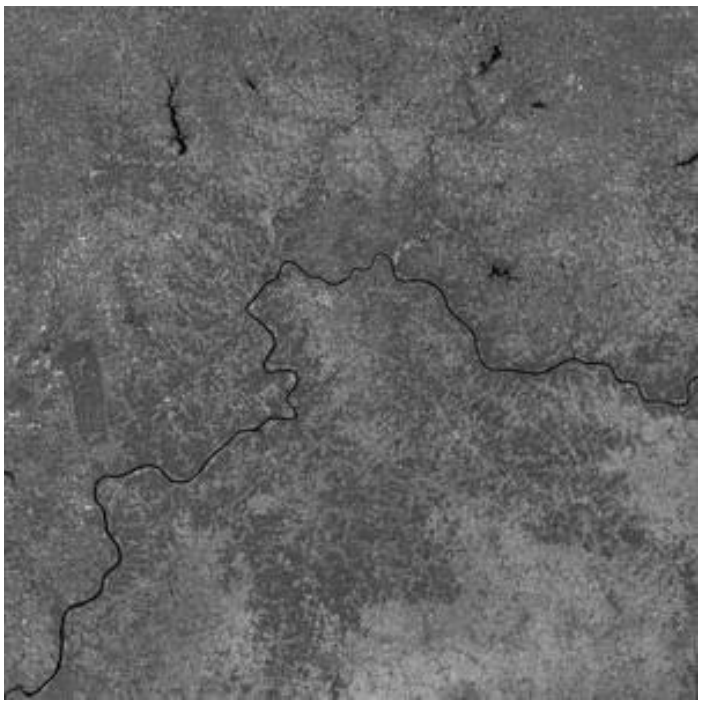

Figure 3.4: A 300 square mile Landsat image of the greater Cincinnati, Ohio area [10]. For the LEO case (where the satellite is close to the Earth), an image resolution, PX, of 0.1 km/pixel (10 pixels/km) is used, whereas for the Molniya orbit case (where the satellite is very far from the Earth at it apogee), a PX of 1 km/pixel is used.

$$t_{nxorb} = R_e \frac{\Delta lat}{PX} \tag{3.15}$$

$$t_{nyorb} = R_e \frac{\Delta lon}{PX} \cos(lat_{nom}), \tag{3.16}$$

where R_e is the radius of the Earth in the e-frame (approximately 6,378 km), and the angular latitude and longitude separation in the e-frame (as a result of the difference between the nominal and true satellite trajectories), Δlat and Δlon, are defined as

$$\Delta lat = lat_{nom} - lat_{true} \tag{3.17}$$

$$\Delta lon = lon_{nom} - lon_{true}. \tag{3.18}$$

Since it is assumed that the terrain is flat, knowledge of the true altitude error is not necessary and therefore is not computed. Next, the true target location error as a function of only the attitude error first order Gauss-Markov processes, t_{nxFOGM} and t_{nyFOGM}, described in Section 3.3.2, are calculated as

$$t_{nxFOGM} = d_o \phi_{FOGM} \tag{3.19}$$

$$t_{nyFOGM} = d_o \theta_{FOGM}. \tag{3.20}$$

The slant range, d_o, from the satellite position to the target aimpoint, is calculated as

$$d_o = \sqrt{(r_x - x_{oe})^2 + (r_y - y_{oe})^2 + (r_z - z_{oe})^2}, \tag{3.21}$$

and the first-order Gauss-Markov attitude errors are calculated as

$$\phi_{FOGM}(i) = e^{-\Delta t/\tau_\phi}\ \phi_{FOGM}(i-1) \tag{3.22}$$

$$\theta_{FOGM}(i) = e^{-\Delta t/\tau_\theta}\ \theta_{FOGM}(i-1), \tag{3.23}$$

where i is the current sample, $i-1$ is the previous sample, and Δt is the time between samples.

Finally, the combined true target location error in the n-frame, t_{nxtrue} and t_{nytrue}, as a function of both orbital drift and first order Gauss-Markov processes, are defined as

$$t_{nxtruth} = t_{nxorb} + t_{nxFOGM} \tag{3.24}$$

$$t_{nytruth} = t_{nyorb} + t_{nyFOGM} \tag{3.25}$$

An example of the resulting landmark state truth data, mapped onto a target of interest (East Fork Lake, 25 miles east of downtown Cincinnati), is depicted in Figure 3.5.

3.5 Image Matching Development

Image matching techniques discussed in Section 2.7.2 can be implemented as a means of tracking a target with unique features among a series of pixelated images. By incorporating matched image data between subsequent images, it can be determine how a stationary target appears to "drift" between those images, therefore providing indirect knowledge of how the true landmark error is generated.

Using the sum-of-squared-difference approach defined in Equation (2.70), a satellite image, representing what the onboard image sensor "sees" based upon the satellites view angle, is sampled across each pixelated row and column with respect

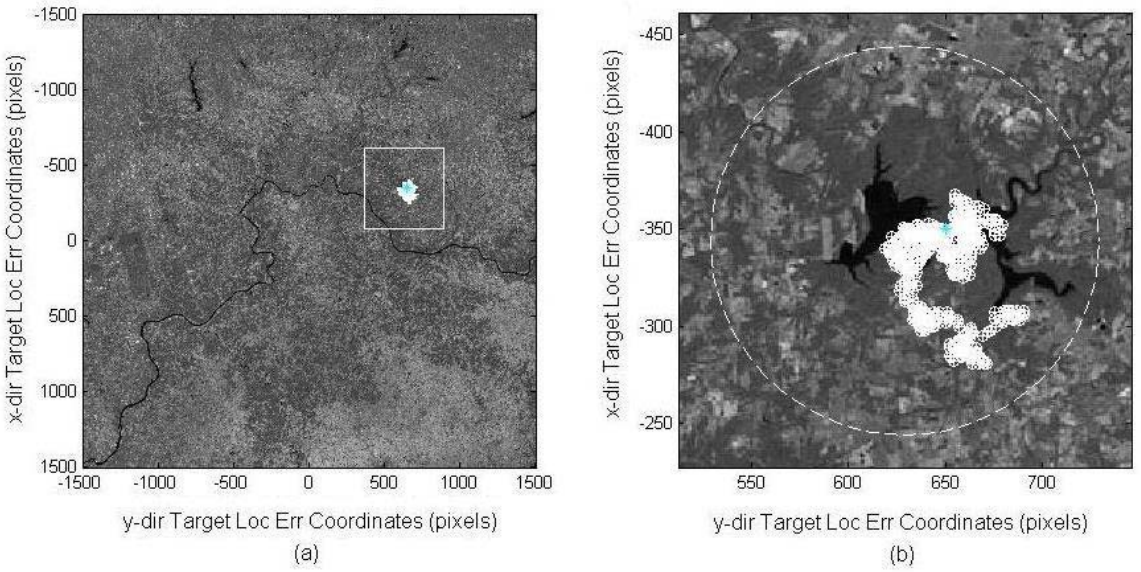

Figure 3.5: Generated ground error in the LEO case, as a function of orbital drift and first-order Gauss-Markov processes. In (a), the target of interest (East Fork Lake) is tracked in a generated image with a swath width of 500 pixels (50 km), as dictated by the satellite's view angle. The blue asterisk denoting the target in (b) is within 3 sigma of the generated ground error uncertainty (represented here as a dashed circle).

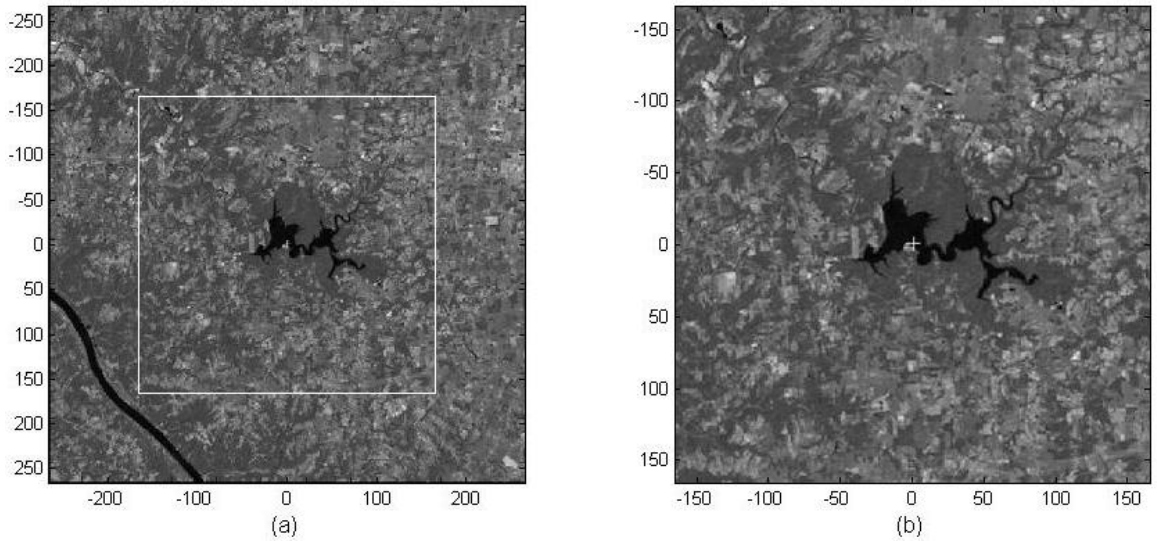

Figure 3.6: Matching a satellite image containing a target of interest (b) within an image template (a), using the SSD approach. In (a), the overlaying image is sampled across each row and column, and the SSD for each sampling is computed in order to determine the lowest SSD intensity (best match).

to an image template (that being the 300 square mile image presented in Figure 3.4). This concept is represented in Figure 3.6, where the target of interest (the lake tracked in Figure 3.5) is matched onto the 300 square mile map of the greater Cincinnati, Ohio area.

The SSD process can be represented as a three dimensional contour plot, in which lower SSD values indicating where the difference between the image and template is minimal, representing the best match between the two images. This is illustrated in Figure 3.7.

3.6 Georeferencing Development

Although the image matching process described in Section 3.5 is an efficient means of determining how a target of interest wanders between subsequent satellite images, it has no knowledge of any existing initial measurement error generated prior to the image matching process. In other words, when the first image is captured, the image sensor assumes that no initial target location error exists, and unknowingly

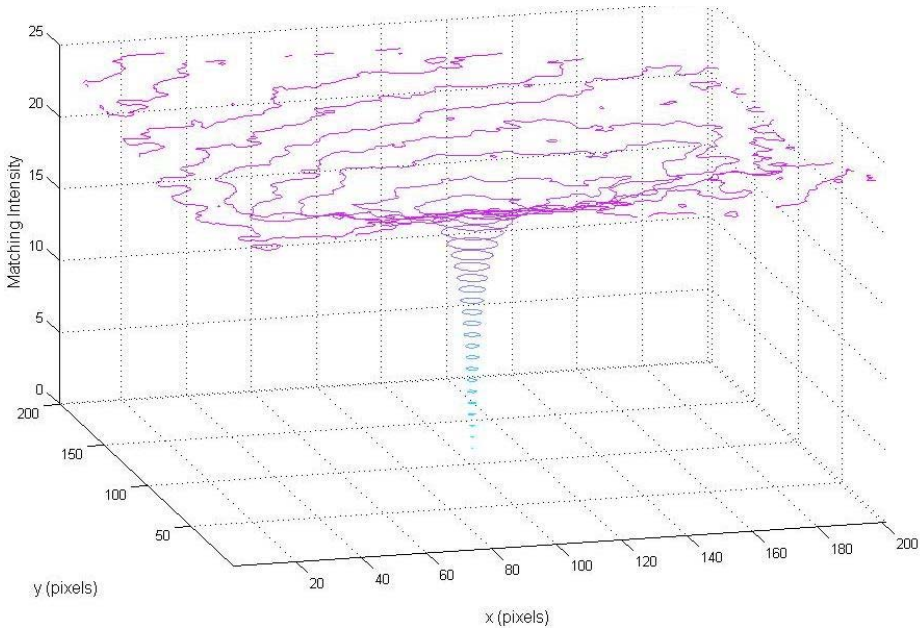

Figure 3.7: A 3-D contour plot of the resulting SSD calculations for each row and column sample. The "best match" is determined to be where the SSD values reach a local minimum, indicating where the difference between the satellite image and image template is smallest.

matches the future captured images relative to the first image. Whether or not the image does in fact contain the target in never truly determined.

Georeferencing provides a solution to this dilemma. Knowledge of the initial target location error by means of automated georeferencing (see Section 2.7.2), the target's true location in the n-frame can be determined relative to a reference map of the Earth. Essentially, a georeferenced image can be used to accurately predict the initial true pixel location of the target. The benefits of geolocation are apparent in Figure 3.8, where a constant "bias" between the SSD matched landmark state and the truth data can be seen. The remaining bias between the matched data and truth data is simply calculated as

$$\mathbf{t}_{nbias} \simeq \mathbf{t}_{nmatch} - \mathbf{t}_{ntruth}. \tag{3.26}$$

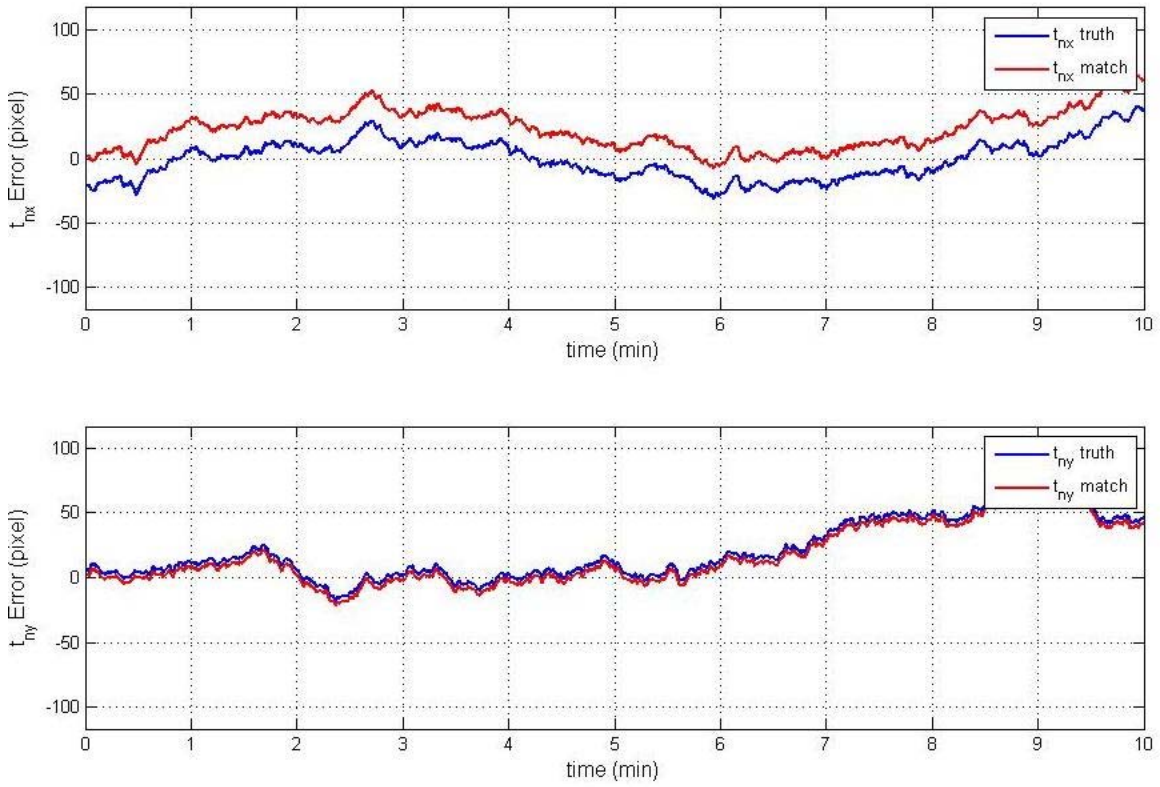

Figure 3.8: Plotting of the best matched northern and eastern target location errors against the generated truth data. The matched data accurately follows the truth data, however, a constant error remains because the initial true pixel location is unknown. This "bias" between the matched data and truth data can be corrected using georeferencing techniques.

Note that $\mathbf{t}_{nbias}$ is only an approximation of this bias, and not a true representation, since its calculation is limited by the available image resolution (rounded to the nearest pixel).

Through combined image matching and georeferencing techniques, an accurate target location error prediction is generated that closely matches the true target location error

$$\mathbf{t}_{npred} \simeq \mathbf{t}_{nmatch} - \mathbf{t}_{nbias} \tag{3.27}$$

$$\mathbf{t}_{npred} \simeq \mathbf{t}_{ntruth}. \tag{3.28}$$

3.7 Extended Kalman Filter Development

Provided the truth data for the navigation and landmark state in Section 3.2, the statistical and noise parameters generated in Section 3.3, and the truth (and predicted) data derived in Sections 3.4 through 3.6, the extended Kalman filter defined in Section 2.3.2 can now be built.

The initial navigation and landmark state mean, $\mathbf{x}_0^\star$, and state covariance, $\mathbf{P}_0^\star$, both derived in Equations (2.81) and (2.82), can be calculated, where, from Equation 3.28, the initial target location error, $\mathbf{y}_0$, is equal to the predicted target location error, or

$$\mathbf{y}_0 = \mathbf{t}_{npred0}. \tag{3.29}$$

The resulting combined initial state vector is

$$\mathbf{x}_0^\star = \begin{bmatrix} \mathbf{x}_0 \\ \\ \mathbf{y}_0 \end{bmatrix} = \begin{bmatrix} r_{xnom0} \\ \\ v_{xnom0} \\ \\ r_{ynom0} \\ \\ v_{ynom0} \\ \\ r_{znom0} \\ \\ v_{znom0} \\ \\ \phi_{nom0} \\ \\ \theta_{nom0} \\ \\ t_{nxpred0} \\ \\ t_{nypred0} \end{bmatrix}. \tag{3.30}$$

Likewise, the resulting combined initial covariance matrix is

$$\mathbf{P}_0^\star = \begin{bmatrix} \mathbf{P}_{xx0} & \mathbf{P}_{xy0} \\ \\ \mathbf{P}_{yx0} & \mathbf{P}_{yy0} \end{bmatrix}, \tag{3.31}$$

where $\mathbf{P}_{xx0}$ is assigned to be

$$\mathbf{P}_{xx0} = \begin{bmatrix} \sigma^2_{r_{x0}} & 0 & 0 & 0 & 0 & 0 & 0 & 0 \\ 0 & \sigma^2_{v_{x0}} & 0 & 0 & 0 & 0 & 0 & 0 \\ 0 & 0 & \sigma^2_{r_{y0}} & 0 & 0 & 0 & 0 & 0 \\ 0 & 0 & 0 & \sigma^2_{v_{y0}} & 0 & 0 & 0 & 0 \\ 0 & 0 & 0 & 0 & \sigma^2_{r_{z0}} & 0 & 0 & 0 \\ 0 & 0 & 0 & 0 & 0 & \sigma^2_{v_{z0}} & 0 & 0 \\ 0 & 0 & 0 & 0 & 0 & 0 & \sigma^2_{\phi_0} & 0 \\ 0 & 0 & 0 & 0 & 0 & 0 & 0 & \sigma^2_{\theta_0} \end{bmatrix}, \tag{3.32}$$

and $\mathbf{P}_{xy0}$, $\mathbf{P}_{yx0}$ and $\mathbf{P}_{yy0}$ are calculated, respectively, as

$$\mathbf{P}_{xy0} = \mathbf{P}_{xx0}\mathbf{G}^T_{yx0} \tag{3.33}$$

$$\mathbf{P}_{yx0} = \mathbf{G}_{yx0}\mathbf{P}_{xx0} \tag{3.34}$$

$$\mathbf{P}_{yy0} = \mathbf{G}_{yx0}\mathbf{P}_{xx0}\mathbf{G}^T_{yx0}. \tag{3.35}$$

The influence coefficient, $\mathbf{G}_{yx0}$, defined in Equation (2.75), is determined from the partial derivatives of the target location error equation solved in Section 3.4, defined as

$$t_{nx} = t_{nxorb} + t_{nxFOGM} \tag{3.36}$$

$$t_{ny} = t_{nyorb} + t_{nyFOGM}. \tag{3.37}$$

Consider the homogeneous nonlinear differential equation defined in Equation (2.16)

$$\dot{\mathbf{x}}^{\star}(t) = \mathbf{f}\,[\,\mathbf{x}^{\star}(t), \mathbf{u}^{\star}(t), t\,]. \tag{3.38}$$

For the given input function, $\mathbf{u}_0^{\star}$ (assumed in this model to be zero), and the initial condition, $\mathbf{x}_0^{\star}$, the nominal solution trajectory, $\tilde{\mathbf{x}}^{\star}(t)$ is known to exist. The perturbations in the initial condition are denoted as

$$\mathbf{x}^{\star}(t) = \tilde{\mathbf{x}}^{\star}(t) + \delta\mathbf{x}^{\star}(t), \tag{3.39}$$

where the perturbation state vector for the system model is defined as

$$\delta\mathbf{x}^{\star}(t) = \begin{bmatrix} \delta r_x \\ \delta v_x \\ \delta r_y \\ \delta v_y \\ \delta r_z \\ \delta v_z \\ \delta\phi \\ \delta\theta \\ \delta t_{nx} \\ \delta t_{ny} \end{bmatrix}. \tag{3.40}$$

From Equations (2.24) and (2.25), the transition matrix and linear perturbation equations, respectively, are therefore

$$\Phi^{\star}(t, t_0) = e^{\mathbf{F}^{\star}(t)\Delta t} \tag{3.41}$$

$$\delta\mathbf{x}^{\star}(t) = \Phi^{\star}(t, t_0)\ \delta\mathbf{x}^{\star}(t^{-}) + \mathbf{w}(t). \tag{3.42}$$

From Equations (2.88) through (2.90) and Equations (3.1) through (3.7), the partial derivative dynamics matrix for both the navigation and landmark states, $\mathbf{F}^{\star}(t)$, is calculated as

$$\mathbf{F}^{\star}(t) = \begin{bmatrix} 0 & 1 & 0 & 0 & 0 & 0 & 0 & 0 & 0 & 0 \\ \frac{\partial \ddot{r}_x}{\partial r_x} & 0 & \frac{\partial \ddot{r}_x}{\partial r_y} & 0 & \frac{\partial \ddot{r}_x}{\partial r_z} & 0 & 0 & 0 & 0 & 0 \\ 0 & 0 & 0 & 1 & 0 & 0 & 0 & 0 & 0 & 0 \\ \frac{\partial \ddot{r}_y}{\partial r_x} & 0 & \frac{\partial \ddot{r}_y}{\partial r_y} & 0 & \frac{\partial \ddot{r}_y}{\partial r_z} & 0 & 0 & 0 & 0 & 0 \\ 0 & 0 & 0 & 0 & 0 & 1 & 0 & 0 & 0 & 0 \\ \frac{\partial \ddot{r}_z}{\partial r_x} & 0 & \frac{\partial \ddot{r}_z}{\partial r_y} & 0 & \frac{\partial \ddot{r}_z}{\partial r_z} & 0 & 0 & 0 & 0 & 0 \\ 0 & 0 & 0 & 0 & 0 & 0 & \frac{\partial \dot{\phi}}{\partial \phi} & 0 & 0 & 0 \\ 0 & 0 & 0 & 0 & 0 & 0 & 0 & \frac{\partial \dot{\theta}}{\partial \theta} & 0 & 0 \\ 0 & 0 & 0 & 0 & 0 & 0 & 0 & 0 & 0 & 0 \\ 0 & 0 & 0 & 0 & 0 & 0 & 0 & 0 & 0 & 0 \end{bmatrix}. \tag{3.43}$$

$\mathbf{F}^{\star}(t)$ can be further solved as

$$\mathbf{F}^{\star}(t) = \begin{bmatrix} 0 & 1 & 0 & 0 & 0 & 0 & 0 & 0 & 0 & 0 \\ \frac{(2r_x^2 - r_y^2 - r_z^2)GM}{\|\mathbf{r}\|^5} & 0 & \frac{3r_x r_y GM}{\|\mathbf{r}\|^5} & 0 & \frac{3r_x r_z GM}{\|\mathbf{r}\|^5} & 0 & 0 & 0 & 0 & 0 \\ 0 & 0 & 0 & 1 & 0 & 0 & 0 & 0 & 0 & 0 \\ \frac{3r_x r_y GM}{\|\mathbf{r}\|^5} & 0 & \frac{(2r_y^2 - r_x^2 - r_z^2)GM}{\|\mathbf{r}\|^5} & 0 & \frac{3r_y r_z GM}{\|\mathbf{r}\|^5} & 0 & 0 & 0 & 0 & 0 \\ 0 & 0 & 0 & 0 & 0 & 1 & 0 & 0 & 0 & 0 \\ \frac{3r_x r_z GM}{\|\mathbf{r}\|^5} & 0 & \frac{3r_y r_z GM}{\|\mathbf{r}\|^5} & 0 & \frac{(2r_z^2 - r_x^2 - r_y^2)GM}{\|\mathbf{r}\|^5} & 0 & 0 & 0 & 0 & 0 \\ 0 & 0 & 0 & 0 & 0 & 0 & -\frac{1}{\tau_\phi} & 0 & 0 & 0 \\ 0 & 0 & 0 & 0 & 0 & 0 & 0 & -\frac{1}{\tau_\theta} & 0 & 0 \\ 0 & 0 & 0 & 0 & 0 & 0 & 0 & 0 & 0 & 0 \\ 0 & 0 & 0 & 0 & 0 & 0 & 0 & 0 & 0 & 0 \end{bmatrix}. \tag{3.44}$$

Note that the dynamics of the landmark states, $\dot{t}_{nx}$ and $\dot{t}_{ny}$, are zero, since they are stochastic projections of the navigation state (see Section 2.8). From Equations (2.92) through (2.94), and Equation (3.13), the partial derivative pixel projection matrix, $\mathbf{H}^{\star}(t)$, is calculated as

$$\mathbf{H}^{\star}(t) = \begin{bmatrix} \frac{\partial \Delta x_{meas}}{\partial r_x} & 0 & \frac{\partial \Delta x_{meas}}{\partial r_y} & 0 & \frac{\partial \Delta x_{meas}}{\partial r_z} & 0 & \frac{\partial \Delta x_{meas}}{\partial \phi} & 0 & 1 & 0 \\ \frac{\partial \Delta y_{meas}}{\partial r_x} & 0 & \frac{\partial \Delta y_{meas}}{\partial r_y} & 0 & \frac{\partial \Delta y_{meas}}{\partial r_z} & 0 & 0 & \frac{\partial \Delta y_{meas}}{\partial \theta} & 0 & 1 \end{bmatrix}. \tag{3.45}$$

$\mathbf{H}^{\star}(t)$ can be further solved as

$$\mathbf{H}^{\star}(t) = \begin{bmatrix} \frac{-\phi\ (r_x - x_{oe})}{H'\ PX} & 0 & \frac{-\phi\ (r_y - y_{oe})}{H'\ PX} & 0 & \frac{-\phi\ (r_z - z_{oe})}{H'\ PX} & 0 & \frac{-H'}{PX} & 0 & 1 & 0 \\ \frac{-\theta\ (r_x - x_{oe})}{H'\ PX} & 0 & \frac{-\theta\ (r_y - y_{oe})}{H'\ PX} & 0 & \frac{-\theta\ (r_z - z_{oe})}{H'\ PX} & 0 & 0 & \frac{-H'}{PX} & 0 & 1 \end{bmatrix}, \quad (3.46)$$

where H' is defined as

$$H' = \sqrt{r_x^2 - 2r_x x_{oe} + x_{oe}^2 + r_y^2 - 2r_y y_{oe} + y_{oe}^2 + r_z^2 - 2r_z z_{oe} + z_{oe}^2}. \quad (3.47)$$

The resulting estimates of the navigation and landmark state will be presented in the next chapter.

IV. Results and Observations

In order to validate the mathematical methods presented in Chapter III, the satellite-based image-aided navigation system algorithms are evaluated using simulation-based analyses. First, the development of the simulation will be described. An analysis of Monte Carlo results for a satellite system in both low Earth and Molniya orbits will follow.

4.1 Simulation Development

The performance of the extended Kalman filter built in Section 3.7 is verified using a statistical ensemble of sample functions, totaling 100 sample functions per Monte Carlo run. Each Monte Carlo run has a 20 minute duration, sampling at 1 Hz (for a total of 1200 data points per sample). For each sample, an entirely new set of inertial sensor and imaging system data is generated using the respective system dynamics and and error models described Chapter III, and are based upon the assigned statistical and noise parameters listed in Table 3.6.

For each 20 minute run, the EKF is implemented for three distinct profiles: the first without any image-aided updates to the target location error estimate, the second using only the image matching method developed in Section 3.5 to update the target location error estimate, and the third using both image matching and georeferencing methods developed in Sections 3.5 and 3.6 to update the target location error estimate. For convenience, these profiles were be referred to as "non-updated", "image-matched", and "image-corrected", accordingly.

In each profile, initial and subsequent target location error predictions are made per Equations (3.28) and (3.29). In the non-updated profile, these predictions are assigned to be zero mean with initial uncertainty, $\mathbf{P}_0^\star$. In the image-matched profile, subsequent images are matched to the first captured image in order to reduce optical drift; however, without knowledge of the initial target location error, a constant target location error will remain. Finally, in the image-corrected profile, the initial bias of

the image matched profile is corrected through georeferencing, therefore providing the most precise target geolocation capability of the three profiles.

In order to demonstrate system performance in multiple orbits, two Monte Carlo scenarios will be implemented. The first scenario contains a satellite system in low Earth orbit, where the satellite is located in a relatively small orbital apogee and image resolution is high. The second scenario consist of a system in a Molniya orbit, where the satellite is located in a relatively high orbital apogee and image resolution is low. Orbital and imaging system parameters are listed in Tables 3.1 and 3.3, respectively.

For simplicity, the pre-generated high-resolution and low-resolution satellite images of the greater Cincinnati, Ohio area are used to represent a satellite in the LEO and MOL orbits, respectively. This template is depicted in Figure 3.4. Whereas these static satellite images are appropriate for testing the coupled image/inertial sensor algorithm, the results are not directly comparable to the performance of a real satellite imaging system. As such, imaging issues including poor sunlight conditions, target obstruction, ego-motion disparity and motion blur between subsequent images are not modeled [25].

4.2 Low Earth Orbit Simulation

The navigation and landmark state errors of the imaging satellite are simulated in 20 minute durations for a total of 100 samples. The satellite is initialized in a LEO orbit at an elevation of 598 km (at apogee) above the Cincinnati, Ohio area, with an imaging resolution of 0.1 km/pixel.

The position and velocity errors of the satellite, in the e-frame x-, y- and z-directions, are shown in Figures 4.1 through 4.2, respectfully. As expected with large acceleration-level noise, the inertial position and velocity measurement errors accumulate over time, resulting in quickly growing position and velocity error uncertainties without bound. The observed drift from zero mean is the result of two phenomenon. The first phenomenon is that the additive error, introduced onto the initial position

and velocity states prior to propagation, results in a slight deviation of the estimated orbit from true orbit over time, producing a non-zero position and velocity error mean. The second phenomenon is due to an insufficient number of Monte Carlo samples, resulting in a perceived "bias" of each position and velocity error state away from the true zero mean. Although not confirmed by this research, it is hypothesized that by running tens of thousands of samples, the position and velocity errors would begin to approach their expected zero means. Note the variations of position and velocity errors between non-updated, image-matched and image-corrected profiles were minimal; therefore, only the non-updated profile is depicted.

The attitude errors of the imaging system, time-correlated first-order Gauss-Markov processes described in Sections 3.2.1 and 3.3, are shown in Figure 4.3. Being first-order Gauss-Markov processes, the state estimates are zero-mean with growing uncertainties, reaching a steady state of approximately 0.17 degs at time constant, τ, of 10 minutes. Note the variations of attitude errors between non-updated, image-matched and image-corrected profiles were minimal; therefore, only the non-updated profile is depicted.

The n-frame target location errors are estimated with respect to the non-updated, image-matched and image-corrected profiles as shown in Figures 4.4 through 4.6, respectfully. As a stochastic projection of the navigation states, the behavior of the non-updated target location errors in Figure 4.4 correspond to the growing position and velocity errors and of the first-order Gauss-Markov attitude errors. As such, a zero-mean target location error is observed with a large, unbounded uncertainty growing over the 20 min duration. Recalling Equation (3.37), the target location error due to satellite orbital drift is dominate in LEO orbit, primarily the result to faster satellite trajectories, larger off-nadir angles and larger atmospheric effect considerations, causing a larger initial uncertainty in a particular direction (in this case, the x-direction). The non-updated profile can be visualized with respect to the satellite image in Figure 4.7.

The image-matched target location errors in Figure 4.5 are also zero-mean; however, it can be seen that the time-correlated drift with respect to the attitude states is suppressed by the image matching algorithm, resulting in steady uncertainties. This uncertainty remains high, however, since navigation state uncertainties are large and knowledge of the initial target location error is not available. Again, the satellite orbital drift due to large statistical and noise parameters dominates the target location error, potentially causing a larger uncertainty in a particular direction (in this case, the x-direction). The image-matched profile can be visualized with respect to the satellite image in Figure 4.8.

In Figure 4.6, the image-corrected target location error remains small in both x- and y-directions. This error is seen to improve by roughly an order of magnitude compared to that of the previous two profiles. The image-corrected profile takes advantage of both the image-matching algorithm (which corrects the time-correlated drift) as well as the georeferencing algorithm (which corrects the initial target location error). The result is a greatly reduced target location error throughout the entire 20 minute duration, corrupted only by minor measurement noise. The image-corrected profile can be visualized with respect to the satellite image in Figure 4.9.

Finally, the root-sum-squared (RSS) errors of the target location error are analyzed in order to provide a more direct comparison of the simulated satellite system's performance with respect to the three profiles. The RRS errors comparing the target location errors in these three cases are shown in Figure 4.10. Over the entire 20 minute simulation, it can be clearly seen that the image-corrected profile improves the system performance by an order of magnitude over that of the non-updated and image-matched profiles.

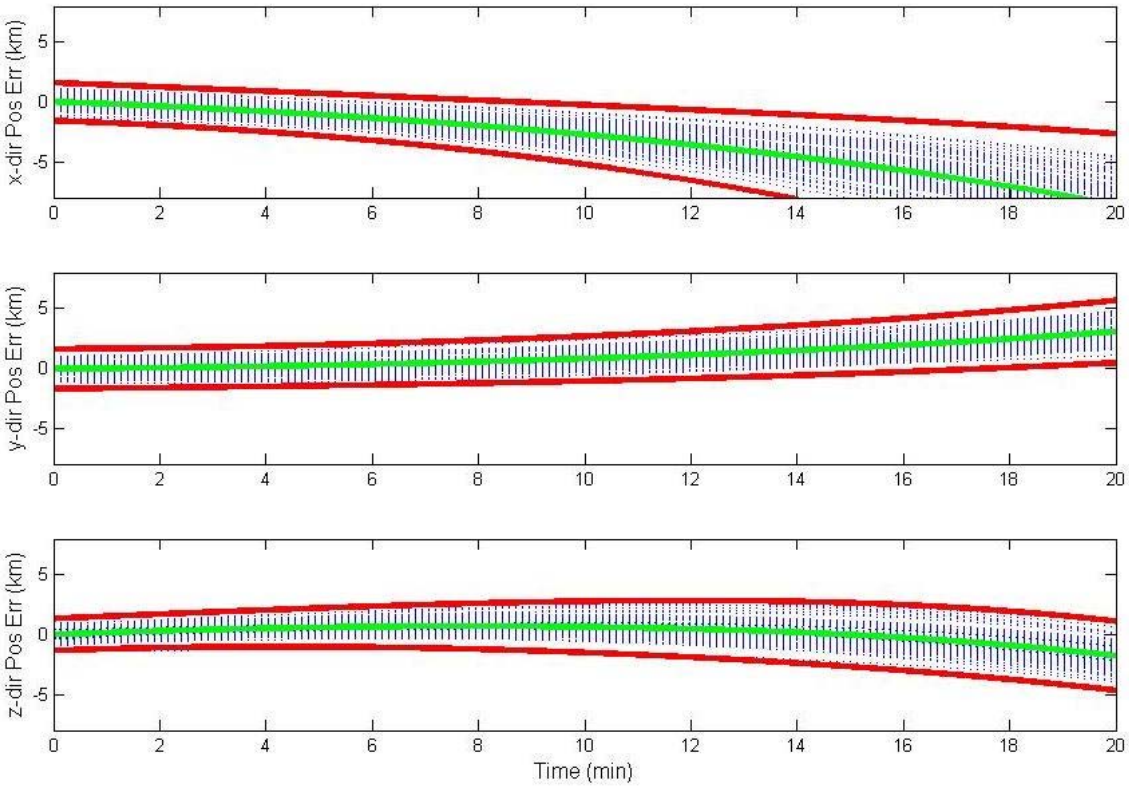

Figure 4.1: Simulated 100-run Monte Carlo satellite position error results in LEO, without image updates. The position error sample functions are indicated by blue dotted lines. The ensemble mean and 3-sigma standard deviation are indicated by the green and red solid lines, respectively. The large acceleration-level noise results in quickly growing position uncertainties. The observed drift is most likely due to both the initial introduction of acceleration noise as well as the low number of Monte Carlo samples.

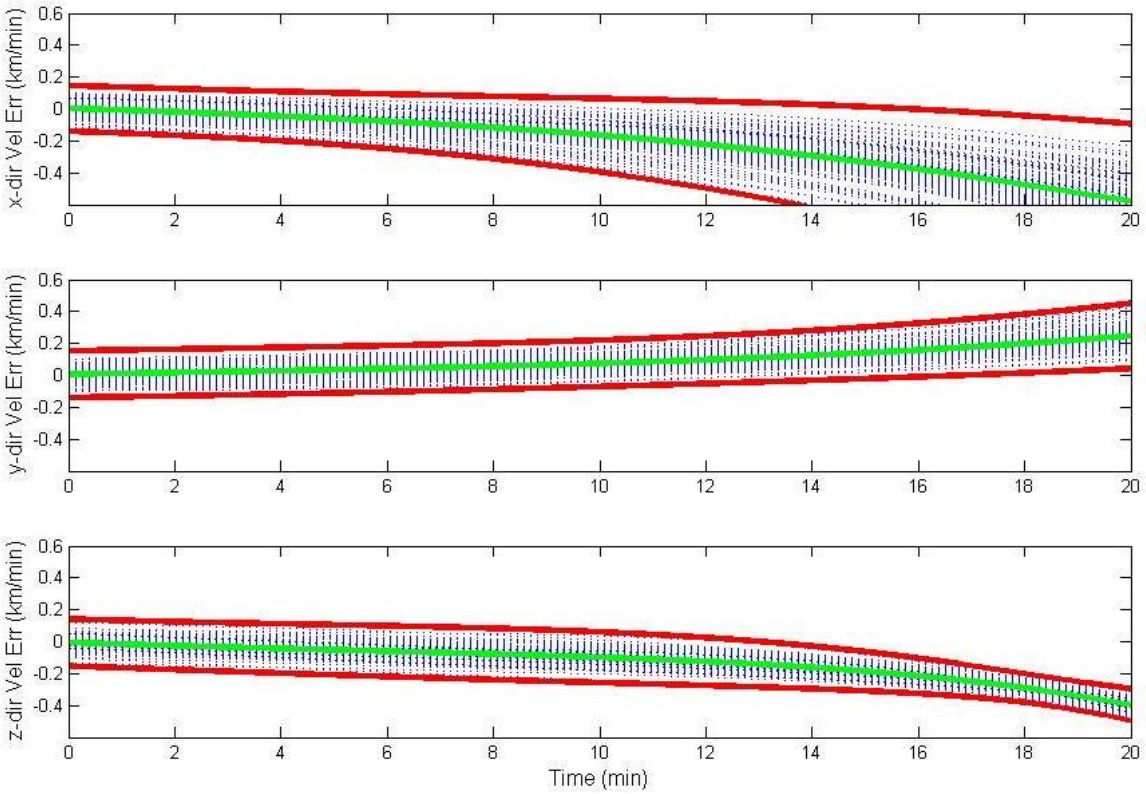

Figure 4.2: Simulated 100-run Monte Carlo satellite velocity error results in LEO, without image updates. The velocity error sample functions are indicated by blue dotted lines. The ensemble mean and 3-sigma standard deviation are indicated by the green and red solid lines, respectively. The large acceleration-level noise results in quickly growing velocity uncertainties. The observed drift is most likely due to both the initial introduction of acceleration noise as well as the low number of Monte Carlo samples.

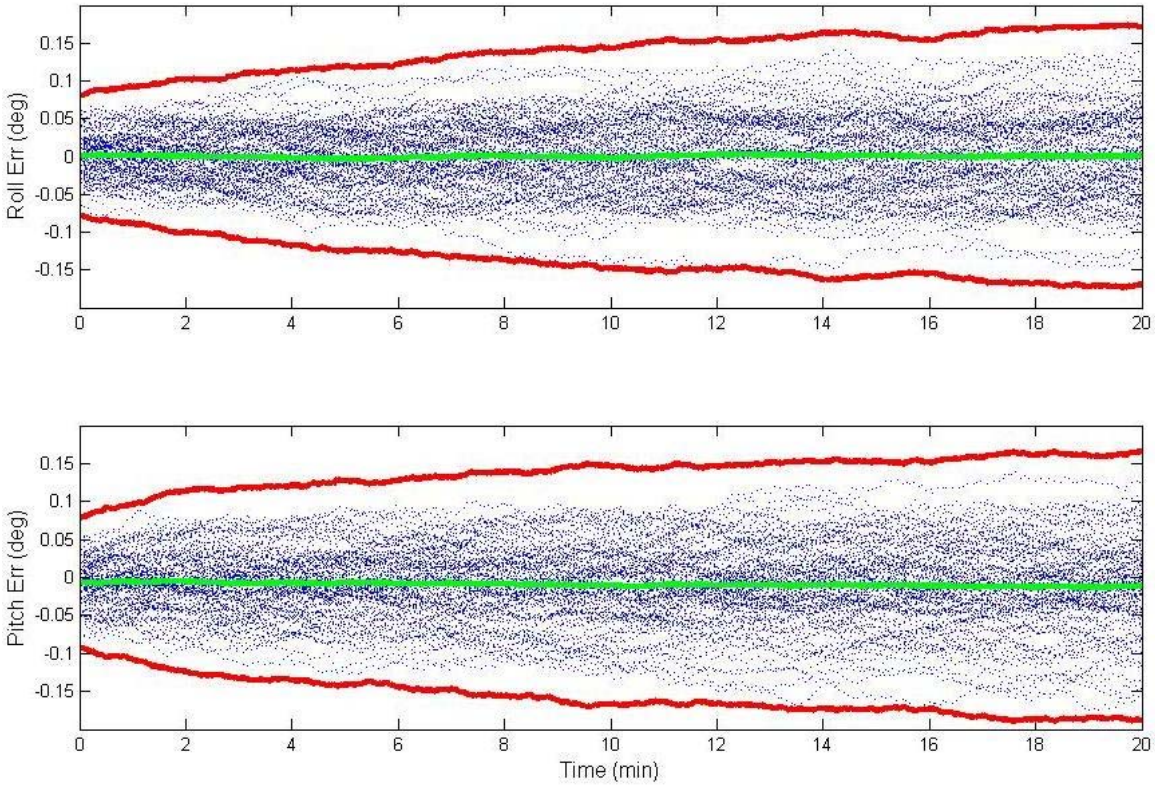

Figure 4.3: Simulated 100-run Monte Carlo satellite attitude error results in LEO, without image updates. The attitude error sample functions are indicated by blue dotted lines. The ensemble mean and 3-sigma standard deviation are indicated by the green and red solid lines, respectively. The attitude errors are zero-mean with growing uncertainties, reaching a steady state of approximately 0.17 degs at a time constant, τ, of 10 minutes.

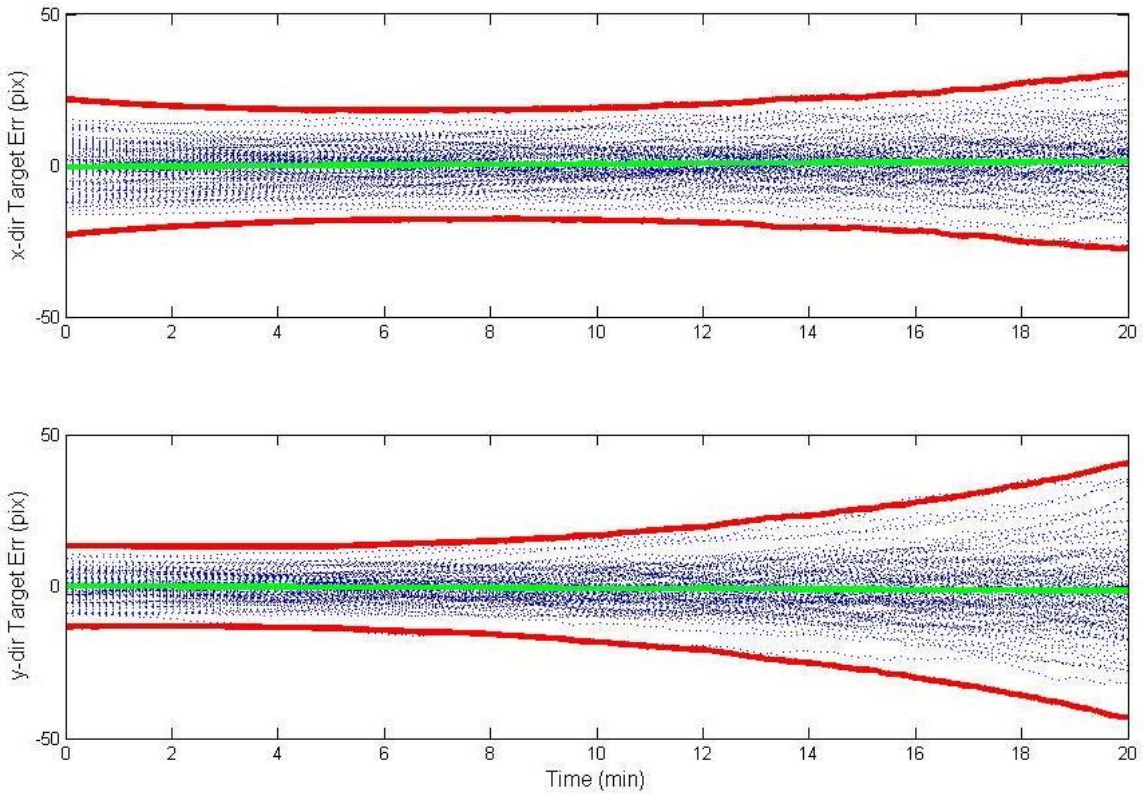

Figure 4.4: Simulated 100-run Monte Carlo target location error results in LEO, without image updates. The target location error sample functions are indicated by blue dotted lines. The ensemble mean and standard deviation are indicated by the green and red solid lines, respectively. A zero-mean target location error is observed with a large, unbounded uncertainty growing over the 20 min duration.

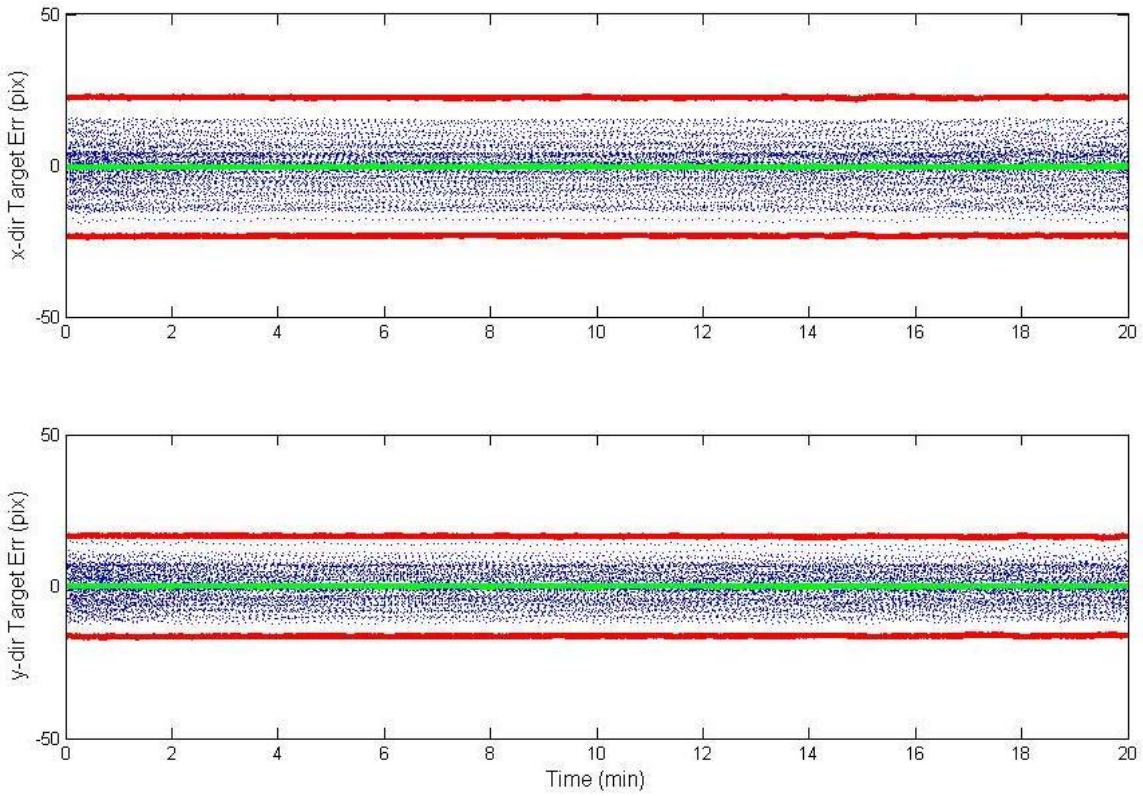

Figure 4.5: Simulated 100-run Monte Carlo target location error results in LEO, with image matching. The target location error sample functions are indicated by blue dotted lines. The ensemble mean and standard deviation are indicated by the green and red solid lines, respectively. The time-correlated drift with respect to the attitude errors is suppressed by the image matching algorithm, resulting in large steady uncertainties.

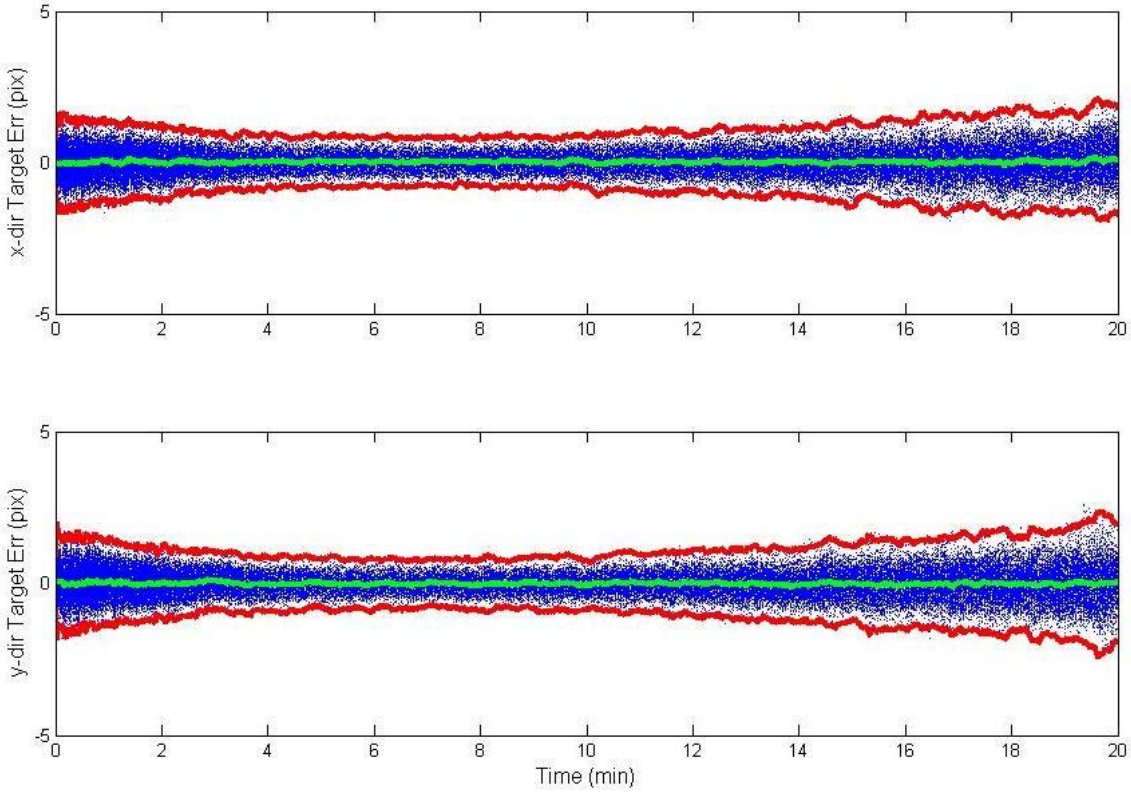

Figure 4.6: Simulated 100-run Monte Carlo target location error results in LEO, with full image correction. The target location error sample functions are indicated by blue dotted lines. The ensemble mean and standard deviation are indicated by the green and red solid lines, respectively. Both time-correlated drift and initial target location error are corrected in this profile, resulting in a reduced target location error by an order of magnitude.

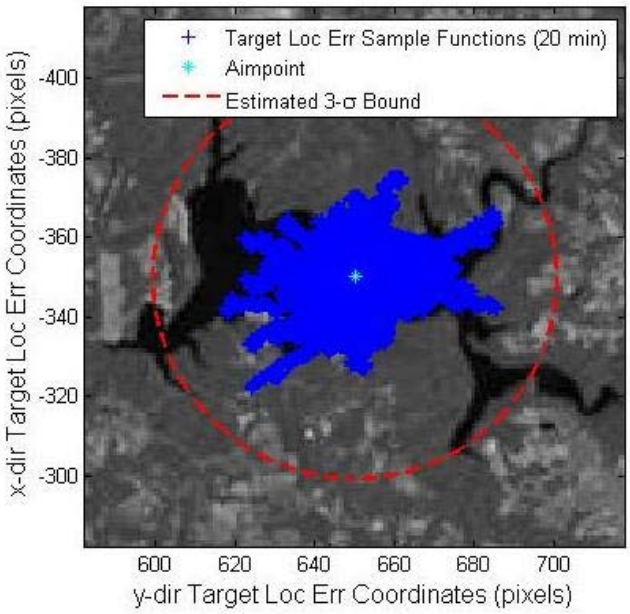

Figure 4.7: Mapped 100-run Monte Carlo target location error results after 20 minutes in LEO, without image updates. Over time, the target location error is seen to grow without bound.

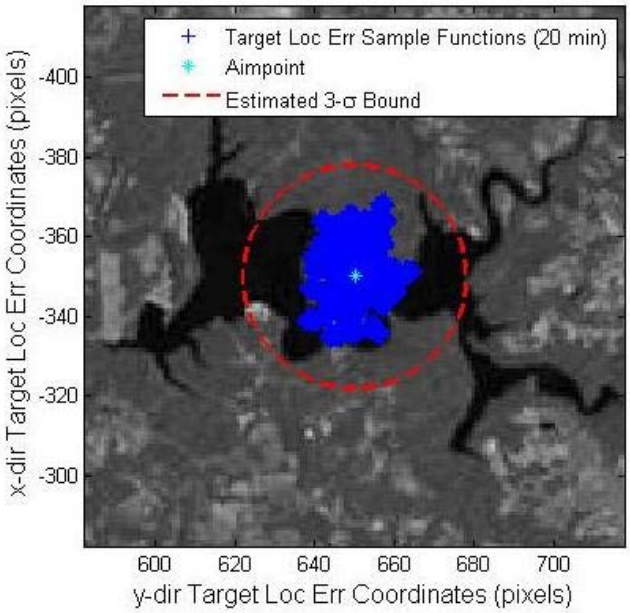

Figure 4.8: Mapped 100-run Monte Carlo target location error results after 20 minutes in LEO, with image matching. Although the initial target location error is large, the error does not significantly drift over time.

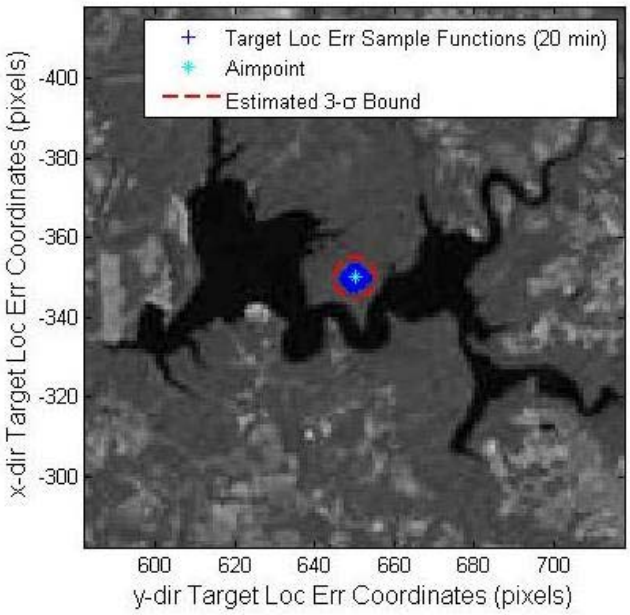

Figure 4.9: Mapped 100-run Monte Carlo target location error results after 20 minutes in LEO, with full image correction. Both the image-matching algorithm (which corrects the time-correlated drift) and georeferencing algorithm (which corrects the initial target location error) are utilized.

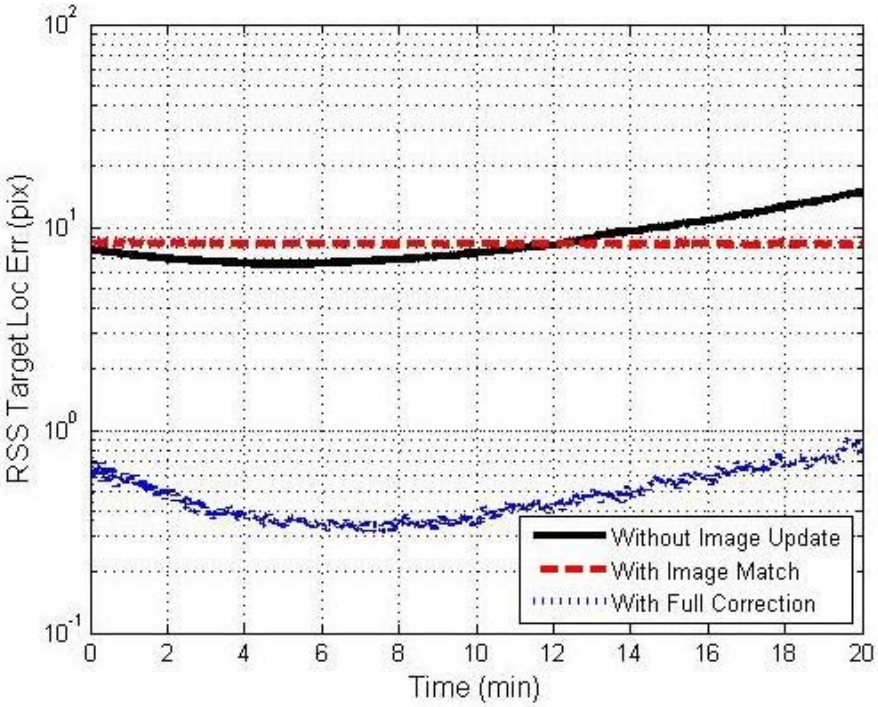

Figure 4.10: Simulated 100-run Monte Carlo root-sum-squared (RSS) target location error results in LEO, comparing the three image-aided profiles. It can be clearly seen that the image-corrected profile improves the system performance by an order of magnitude over that of the non-updated and image-matched profiles.

4.3 High Earth Orbit Simulation

For a satellite system in a MOL orbit, an identical simulation to that of the LEO scenario is conducted to determine whether the satellite system's elevation and image resolution would vastly affect the results. For comparison, the navigation and landmark state errors of the imaging satellite are again simulated in 20 min durations for a total of 100 samples. The satellite is initialized in a MOL orbit at an elevation of 38,900 km (at apogee) above the Cincinnati, Ohio area, with an imaging resolution of 1 km/pixel.

The e-frame x-,y- and z-directional position and velocity errors of the satellite are shown in Figures 4.11 through 4.12, respectfully. With the smaller acceleration-level noise at the higher orbit, the inertial position and velocity measurement errors accumulate more slowly over time, resulting in slowly growing position and velocity error uncertainties without bound. As with the LEO orbit position and navigation error states, the observed drift is due to both the initial introduction of acceleration noise as well as the low number of Monte Carlo samples. Again, the variations of position and velocity errors between non-updated, image-matched and image-corrected profiles were minimal; therefore, only the non-updated profile is depicted.

The time-correlated first-order Gauss-Markov process attitude errors of the imaging system are shown in Figure 4.13. Being first-order Gauss-Markov processes, the state estimates are zero-mean with growing uncertainties, reaching a steady state of approximately 0.017 degs at time constant, τ, of 10 minutes. Again, the variations of attitude errors between non-updated, image-matched and image-corrected profiles were minimal; therefore, only the non-updated profile is depicted.

The n-frame target location errors are estimated with respect to the non-updated, image-matched and image-corrected profiles as shown in Figures 4.14 through 4.16, respectfully. As with the lower orbit scenario, the behavior of the non-updated target location errors in Figure 4.14 correspond to the growing position, velocity, and attitude errors. As such, a zero-mean target location error is observed with a large,

unbounded uncertainty growing over the 20 min duration. The target location error in the MOL scenario is not dominated by either satellite orbital drift or time-correlated optical drift, resulting in a large and unsteady initial uncertainty in both x- or y-directions. The non-updated profile can be visualized with respect to the satellite image in Figure 4.17.

The image-matched target location errors in Figure 4.15 are also zero-mean; however, like in the LEO scenario, the time-correlated attitude drift is suppressed by the image matching algorithm. This results in steady and high uncertainties due to large navigation state uncertainties and unknown initial target location error. In the MOL orbit, neither orbital drift or optical drift dominate the target location error. The image-matched profile can be visualized with respect to the satellite image in Figure 4.18.

In Figure 4.16, the image-corrected target location error remains small in both x- and y-directions. Like the LEO scenario, this error is seen to improve by roughly an order of magnitude compared to that of the previous two profiles, taking advantage of both the image-matching and georeferencing algorithms. The result is a greatly reduced target location error throughout the entire 20 minute duration, corrupted only by minor measurement noise. The image-corrected profile can be visualized with respect to the satellite image in Figure 4.19.

Finally, the RSS errors of the target location error are analyzed with respect to the three profiles. The RRS errors comparing the target location errors in these three cases are shown in Figure 4.20. Very similar to the LEO scenario, it can be clearly seen that the image-corrected profile improves the system performance by an order of magnitude over the entire 20 minute duration.

4.4 Simulation Comparisons

In comparison of the LEO and MOL scenarios, the image-corrected profile in both cases has been shown to provide highly accurate target tracking results over a

20 minute duration. The larger statistical and noise parameters of the LEO orbit, resulting in respectively large navigation uncertainties, still do not drastically affect target tracking performance in the image-matched or image-corrected profiles. Likewise, in both the high-resolution LEO system and low-resolution MOL system, it is shown that subsequent satellite images can be effectively matched and minimal initial target location error can be provided through georeferencing, in order to accurately predict and track the target location in either scenario.

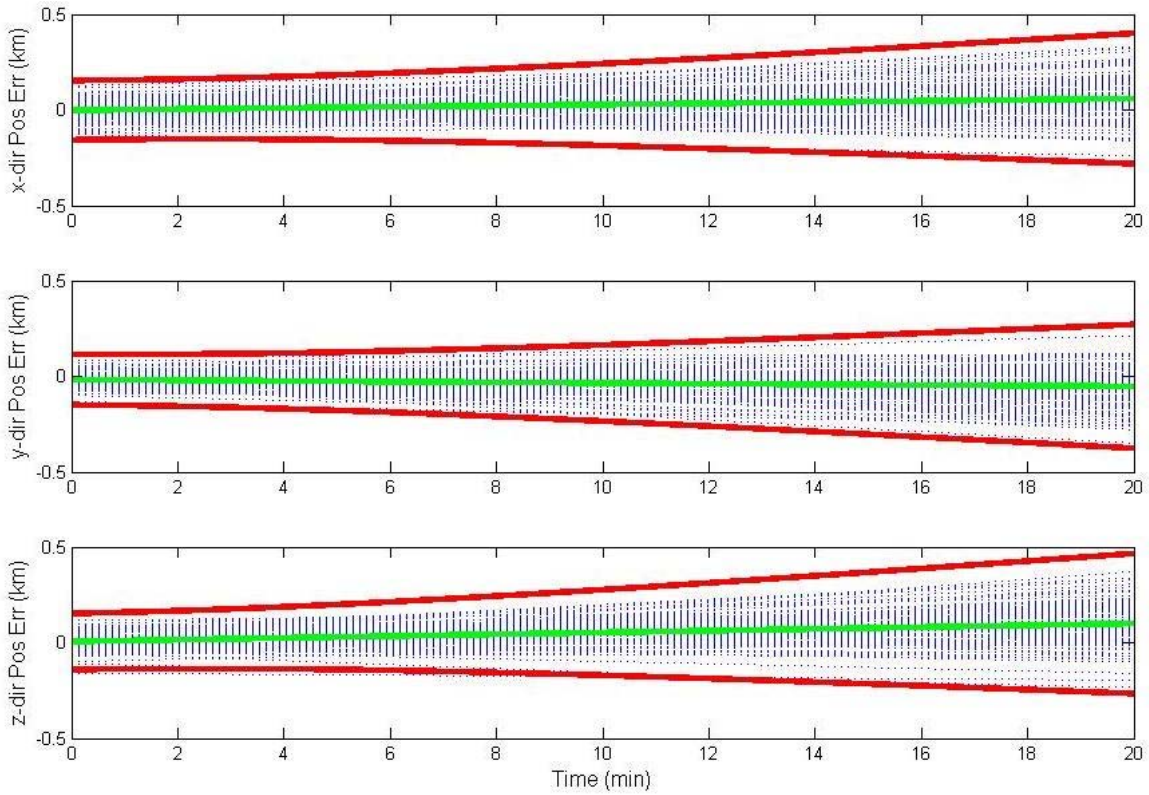

Figure 4.11: Simulated 100-run Monte Carlo satellite position error results in MOL, without image updates. The position error sample functions are indicated by blue dotted lines. The ensemble mean and 3-sigma standard deviation are indicated by the green and red solid lines, respectively. The smaller acceleration-level noise results in slowly growing position uncertainties. The observed minor drift is most likely due to both the initial introduction of acceleration noise as well as the low number of Monte Carlo samples.

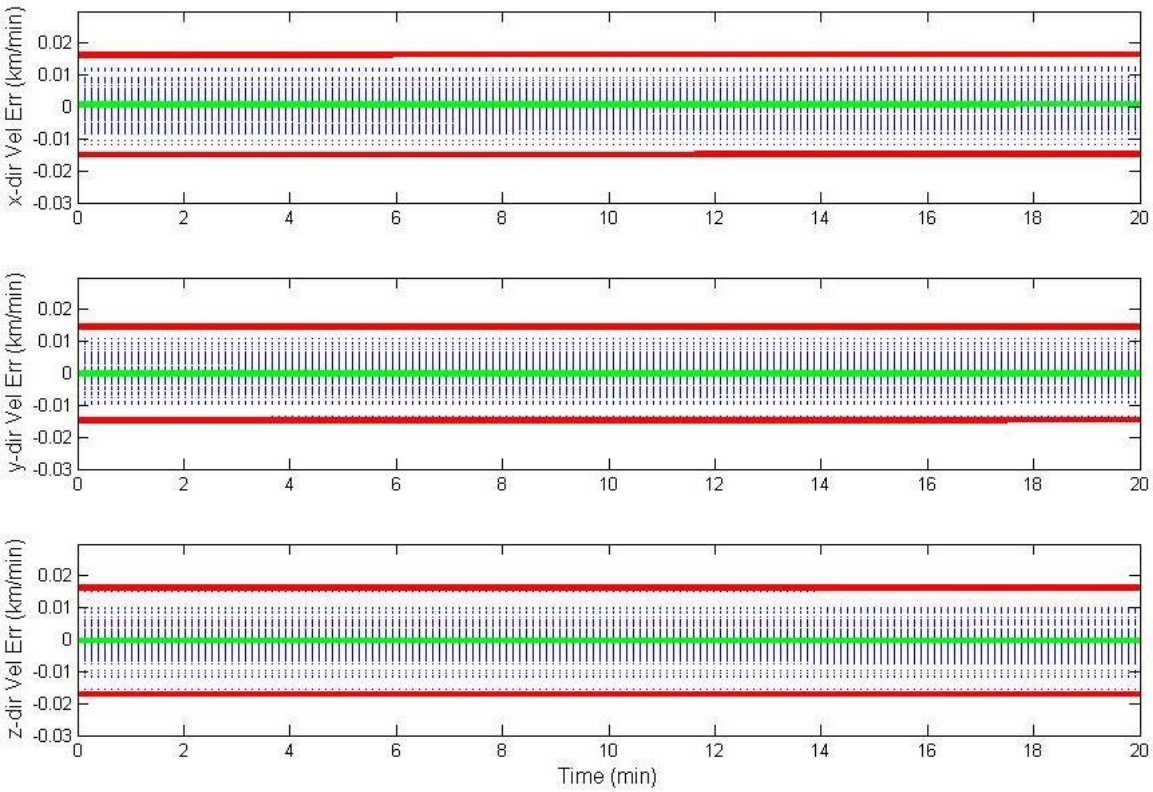

Figure 4.12: Simulated 100-run Monte Carlo satellite velocity error results in MOL, without image updates. The velocity error sample functions are indicated by blue dotted lines. The ensemble mean and 3-sigma standard deviation are indicated by the green and red solid lines, respectively. The smaller acceleration-level noise results in very minor growth of velocity error uncertainties.

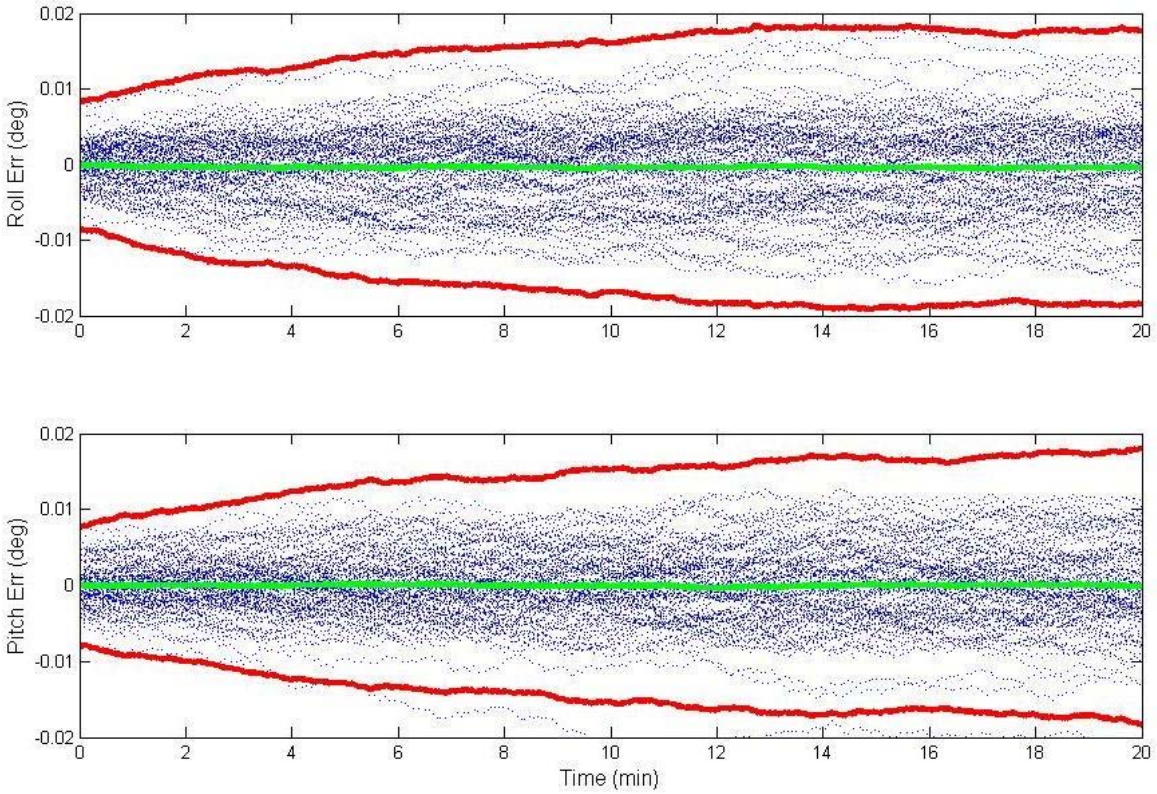

Figure 4.13: Simulated 100-run Monte Carlo satellite attitude error results in MOL, without image updates. The attitude error sample functions are indicated by blue dotted lines. The ensemble mean and 3-sigma standard deviation are indicated by the green and red solid lines, respectively. The attitude errors are zero-mean with growing uncertainties, reaching a steady state of approximately 0.017 degs at a time constant, τ, of 10 minutes.

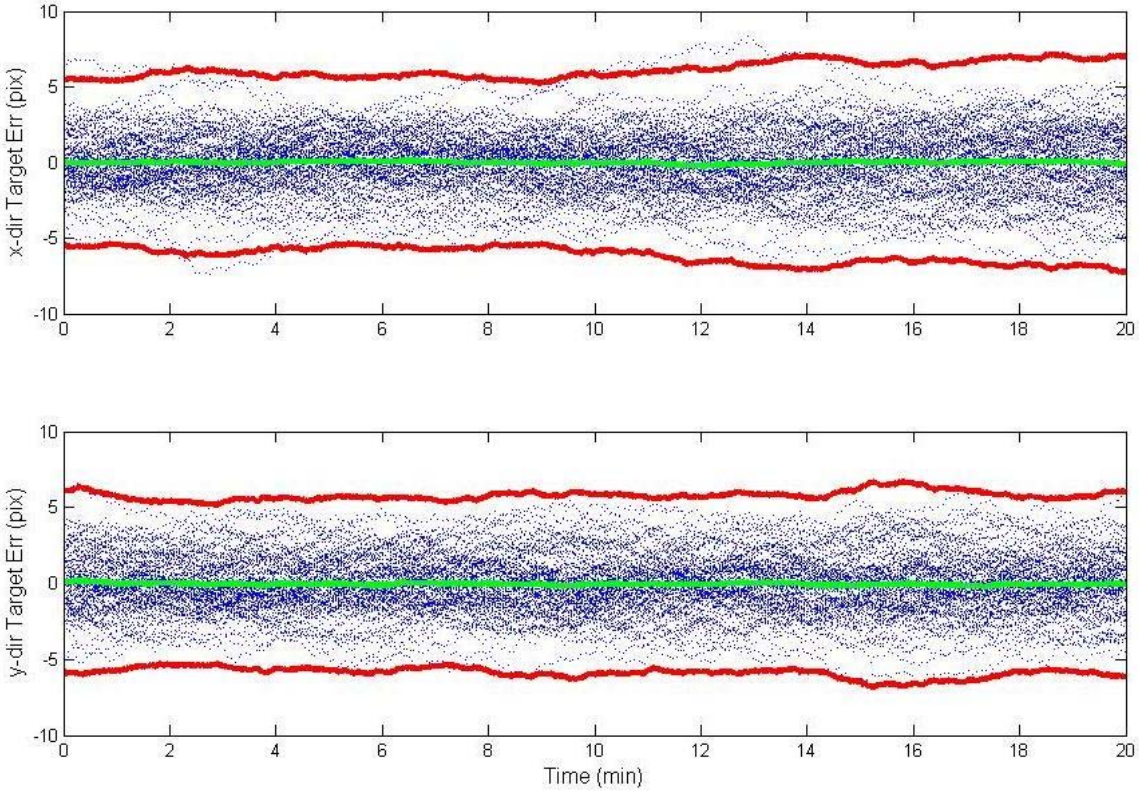

Figure 4.14: Simulated 100-run Monte Carlo target location error results in MOL, without image updates. The target location error sample functions are indicated by blue dotted lines. The ensemble mean and standard deviation are indicated by the green and red solid lines, respectively. A zero-mean target location error is observed with a large, unsteady uncertainties over the 20 min duration.

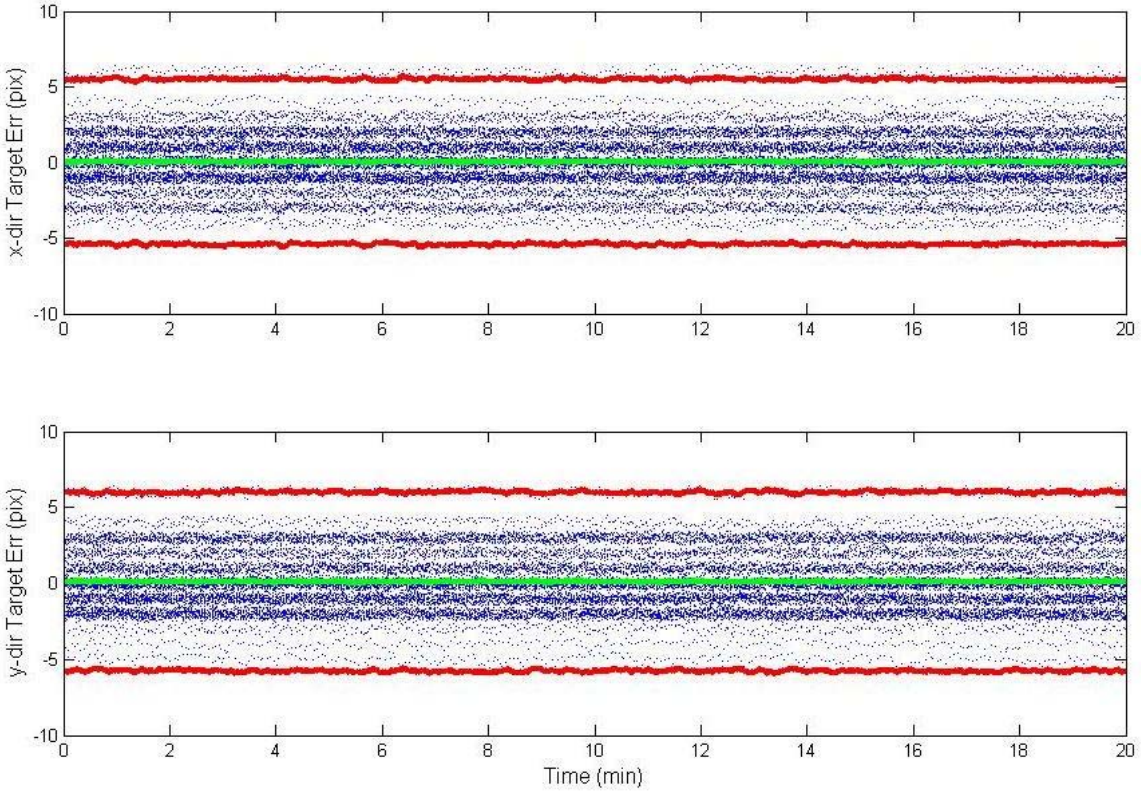

Figure 4.15: Simulated 100-run Monte Carlo target location error results in MOL, with image matching. The target location error sample functions are indicated by blue dotted lines. The ensemble mean and standard deviation are indicated by the green and red solid lines, respectively. The time-correlated drift with respect to the attitude errors is suppressed by the image matching algorithm, resulting in large steady uncertainties.

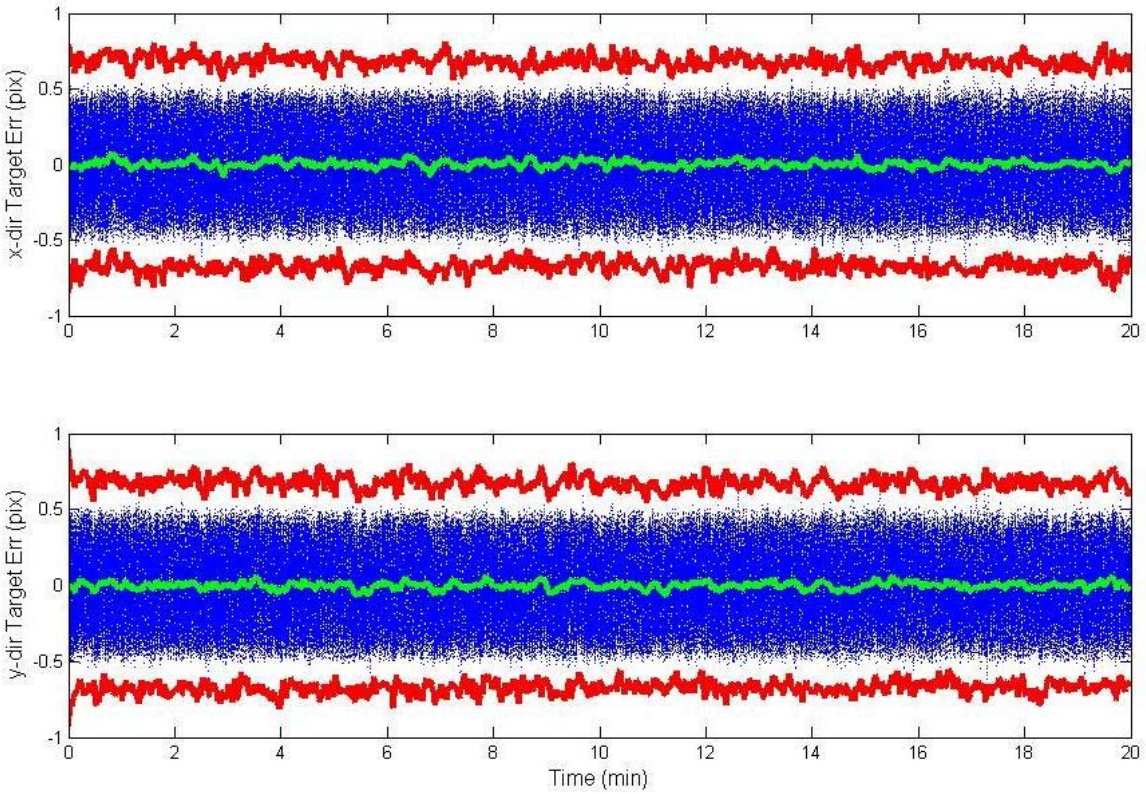

Figure 4.16: Simulated 100-run Monte Carlo target location error results in MOL, with full image correction. The target location error sample functions are indicated by blue dotted lines. The ensemble mean and standard deviation are indicated by the green and red solid lines, respectively. Both time-correlated drift and initial target location error are corrected in this profile, resulting in a reduced target location error by an order of magnitude.

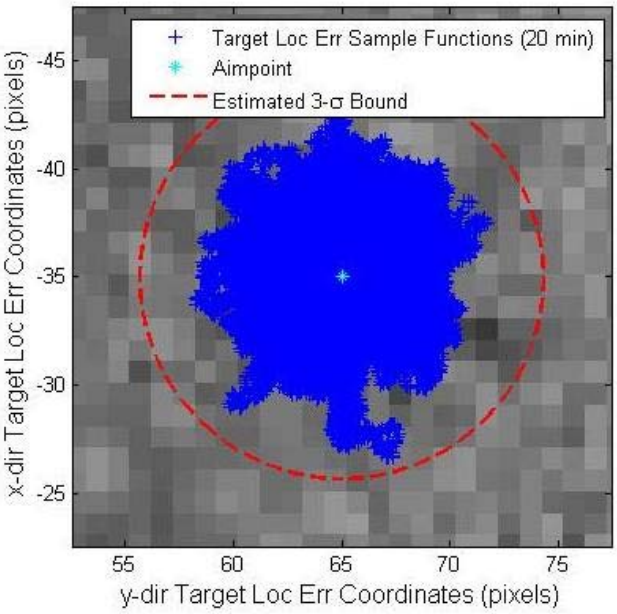

Figure 4.17: Mapped 100-run Monte Carlo target location error results after 20 minutes in MOL, without image updates. Over time, the target location error is seen to very slowly grow without bound.

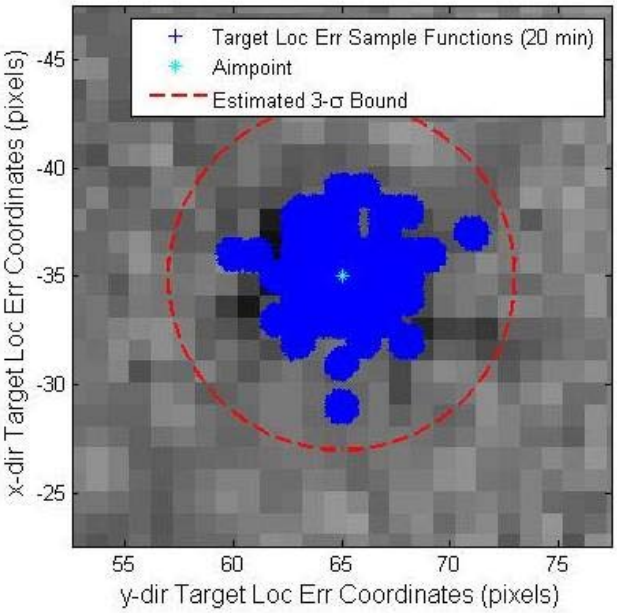

Figure 4.18: Mapped 100-run Monte Carlo target location error results after 20 minutes in MOL, with image matching. Although the initial target location error is large, the error does not significantly drift over time.

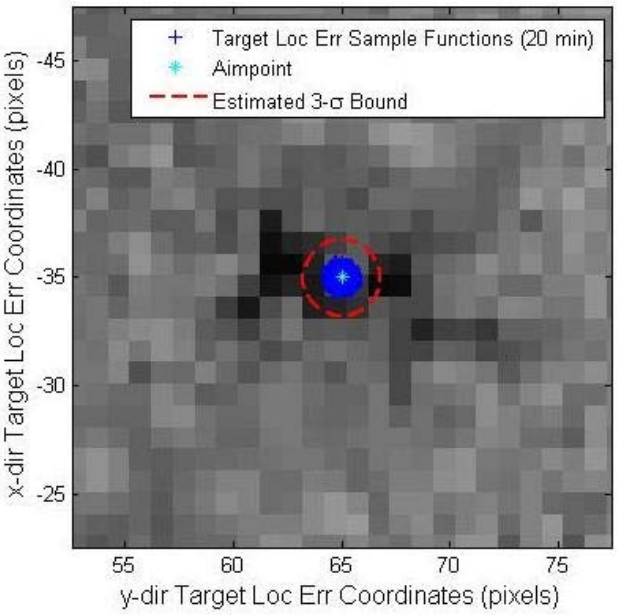

Figure 4.19: Mapped 100-run Monte Carlo target location error results after 20 minutes in MOL, with full image correction. Both the image-matching algorithm (which corrects the time-correlated drift) and georeferencing algorithm (which corrects the initial target location error) are utilized.

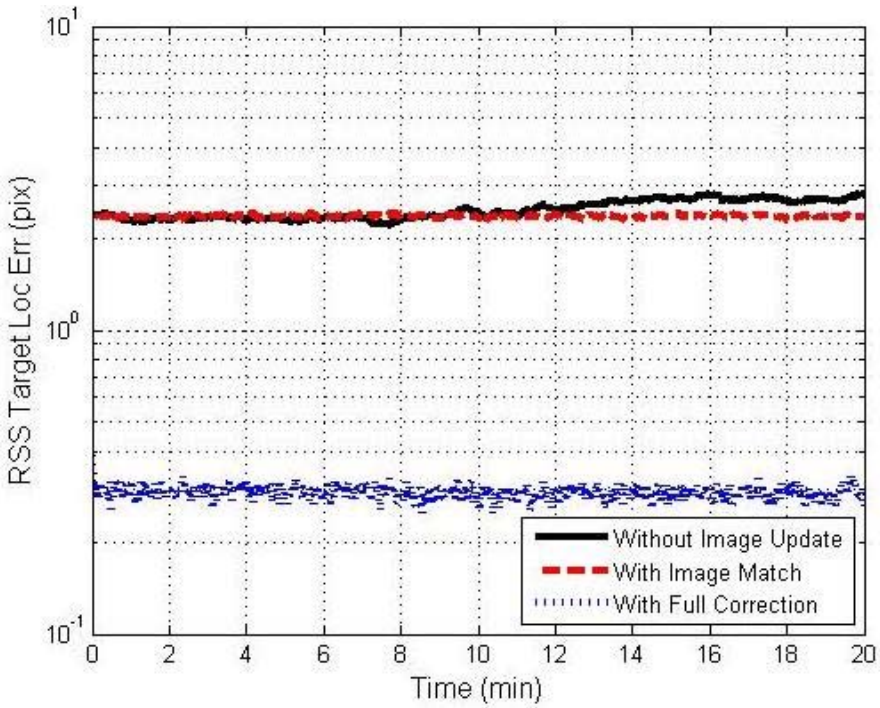

Figure 4.20: Simulated 100-run Monte Carlo root-sum-squared (RSS) target location error results in MOL, comparing the three image-aided profiles. The image-corrected profile improves the system performance by an order of magnitude over that of the non-updated and image-matched profiles.

V. Conclusions

This thesis introduces the concept of fusing the imaging and inertial sensors of a satellite observation system to accurately and autonomously geolocate commercial or military ground targets of interest. In this chapter, conclusions regarding the image-aided satellite system simulation are presented, and potential focus areas of future research are addressed.

5.1 Summary

As mentioned in Chapter I, the goal of this research was to develop a low-cost, low-weight, highly-accurate image-aided inertial satellite navigation system without the need of human interaction or dependency on external navigation system sources. This section summarizes the implementation, results and observations of this system design.

In Chapter III, the orbital modeling parameters listed in Section 3.1 were used to define both a nominal low Earth and Molniya orbit of an imaging satellite. The satellite system parameters and dynamics defined in Section 3.2 described the trajectory of the vehicle and the functionality of the onboard imaging system. Next, the navigation and landmark noise error parameters assigned in Section 3.3 were introduced into the nominal state initial conditions and system dynamics to produce simulated truth data; specifically, the generated ground error as described in Section 3.4. Image matching and georeferencing techniques presented in Sections 3.5 and 3.6, respectively, aided in the tracking of the ground target of interest by detecting unique features of the target between subsequent images and correcting for any initial target location error. Finally, the extended Kalman filter described in Section 3.7 was implemented in order to estimate of the navigation and landmark states and determine the errors between the estimated and truth data over time.

In Chapter IV, the satellite-based image-aided navigation system algorithms defined in Chapter III were evaluated using Monte Carlo simulation-based analyses. The performance of the extended Kalman filter was verified using a 20 minute statistical

ensemble of 100 independent sample functions, sampled at 1 Hz, and were analyzed in three image-aided profiles: non-updated, image-matched and image-corrected. Two separate Monte Carlo scenarios are implemented: the first was a satellite system in a low Earth orbit (with high image resolution) and the second system in a high Earth orbit (with low image resolution). Respective high and low resolution images of the Cincinnati, Ohio area were used to represent the satellite's field of view and identify a unique target of interest. In both LEO and MOL orbit scenarios (Sections 4.2 and 4.3, respectively), it was observed that the full image-aided target location prediction of the image-corrected profile minimized the target location error by an order of magnitude throughout the 20 minute simulation. Additionally, it was shown that the satellite system's trajectory and image resolution capability did not drastically affect the performance of the image-aided satellite system in either scenario, verifying that this model is suitable for both high or low Earth orbit assignments with corresponding image resolution requirements.

5.2 Conclusions

Based upon the methodology, results and observations summarized in Section 5.1, final conclusions of the image-aided satellite inertial navigation system can be made.

A significant motivator defined in Chapter I expressed the need for a low-cost, low-weight, highly-accurate satellite imaging system. Growing expenses associated with overall satellite design and space launch capabilities demand that space vehicles be as efficient and light weight as possible. Since the developed image-aided algorithms defined in Chapter III utilize only pre-existing image and inertial sensors, and no additional vehicle or ground tracking hardware is implemented, it can be reasonably concluded that vehicle cost and weight will not be drastically affected by this design. The accuracy of the fully corrected image-aided model, as discussed in detail in Chapter IV, provides appreciable evidence that minimal target location error is

available for the first 20 minutes of target tracking. It is assumed that this period of time is sufficient for most target tracking applications.

Since this integrated image/inertial Earth observation system actually estimates the extended Kalman filter navigation states of the satellite, these estimates can be fed back into the satellite in order to improve the combined satellite navigation/target tracking solution. This is particularly beneficial to navigation systems requiring routine navigation calibrations since these calibrations are accomplished simultaneously with the target tracking functionality.

Another motivator for this research was to build a system that is fully autonomous and independent of external navigation reference sources, such as GPS or continuous post-capture georeferencing. The image matching SSD algorithm is shown to be fully autonomous, and therefore satisfies this requirement. Likewise, GPS or similar external reference sources are never implemented in this model and is therefore independent of such systems. The georeferencing algorithm used to initially correct the target location prediction could be viewed as a possible infringement; however, in this application, it is assumed that a pre-generated georeferenced map of the area of interest is available, with a sufficient number of control points to accurately correct any initial target location errors. Additionally, since an image matching algorithm is used in conjunction with this georeferencing technique, the target need only be georeferenced once in order to provide significant target tracking improvement. As a comparison, if the target were to instead be georeferenced once every sample (in the case of no available image-matching capabilities), sluggish georeferencing response time would potentially outweigh any target location error correction. It was shown that one-time geolocation early in the simulation provided considerable target tracking improvement throughout the entire simulation; therefore, the response time of one georeferencing sampling is not of major concern.

Although further advances could be made to further optimize the performance of the target tracking system, these results show promise that the development of a robust image-aided satellite system is worthwhile.

5.3 Future Work

This research represents a preliminary analysis in the fusion of image/inertial sensors of Earth-observation satellites for precise geolocation of ground targets. A number of recommendations for future research can be made, further exploring this space-based image-aided navigation system. They are listed as follows:

- *Simulation Using Real Data*: While the pre-generated satellite images are appropriate for testing the coupled image/inertial sensor algorithm, the results are not directly comparable to the performance of a real satellite imaging system. A logical next step would be to test a series of authentic, subsequent satellite images of a feature-rich ground target in order to provide further verification of system performance.
- *Use of a Standard Earth Coordinate Frame*: This research uses a simplistic, spherical Earth model as a reference frame and assumes the target of interest is located at a fixed elevation (i.e., at sea level). A more sophisticated reference coordinate system, such as the World Geodetic System 1984 (WGS 84), would provide more precise ground tracking capabilities for real-world image-aided satellite navigation systems.
- *Introduction of Imaging Anomalies*: Imaging issues such as poor sunlight conditions, partial target obstruction, binocular disparity, motion blur, and affine transformations are not identified in this research. It is recommended that a number of these considerations be modeled to provide further system credibility in the presence of real-world imaging anomalies.

Bibliography

1. Andrews, L. C. and R. L. Phillips. *Laser Beam Propagation through Random Media*. The International Society for Optical Engineering, Bellingham, Washington, United States, second edition, 2005.

2. Dereniak, E. L. and G. D. Boreman. *Infrared Detectors and Systems*. John Wiley & Sons, Inc., New York, New York, United States, 1996.

3. Derpanis, K. G. *Relationship Between the Sum of Squared Difference (SSD) and Cross Correlation for Template Matching*. Technical report, York University, Toronto, Ontario, Canada, December 2005.

4. DigitalGlobe, Inc. *QuickBird Satellite Fact Sheet*. DigitalGlobe, Inc., Longmont, Colorado, United States, Accessed September 2008. URL <`http://www.digitalglobe.com/index.php/85/QuickBird`>.

5. Doviak, R. J. and D. S. Zrnic. *Doppler Radar and Weather Observations*. Dover Publications, Inc., Mineola, New York, United States, second edition, 1993.

6. Fried, D. L. "Limiting Resolution Looking Down Through the Atmosphere". *J. Opt. Soc. Am.*, 56(10), 1966.

7. Fried, D. L. "Scintillation of a Ground-to-Space Laser Illuminator". *J. Opt. Soc. Am.*, 57(8), 1967.

8. Goodman, J. W. *Fourier Optics*. Roberts & Company Publishers, Greenwood Village, Colorado, United States, second edition, 2005.

9. Hecht, E. *Optics*. Pearson Education, Inc., San Francisco, California, United States, forth edition, 2002.

10. landsat.org. *Global Observatory for Ecosystem Services*. Michigan State University, East Lansing, Michigan, United States, Accessed December, 2008. URL <`http://www.landsat.org/`>.

11. Lobo, J. and J. Dias. "Visual and Inertial Sensor Cooperation Using Gravity as a Vertical Reference". *IEEE Transactions on Pattern Analysis and Machine Intelligence*, 25, December 2003.

12. Maybeck, P. S. *Stochastic Models, Estimation, and Control*, volume 1 of *Mathematics in Science and Engineering*. Academic Press, Inc., New York, New York, United States, 1982.

13. Maybeck, P. S. *Stochastic Models, Estimation, and Control*, volume 2 of *Mathematics in Science and Engineering*. Academic Press, Inc., New York, New York, United States, 1982.

14. Michaels, D. "Ball Aerospace Star Tracker Achieves High Tracking Accuracy for a Moving Star Field". *IEEE Aerospace Conference*, March, 2005.

15. Misra, P. and P. Enge. *Global Positioning System Signals, Measurements, and Performance*, volume 3. Ganga-Jamuna Press, Lincoln, Massachusetts, United States, 1982.

16. Olson, C. F. "Maximum-likelihood Image Matching". *IEEE Transaction on Pattern Analysis and Machine Intelligence*, 24, June 2002.

17. Palme, E. *Stereo Vision Library for Obstacle Avoidance Applications.* Master's thesis, University of Fribourg, Switzerland, October 2006.

18. Riishojgaard, L. P. *The Molniya Orbit Imager - A High Latitude Quasi Geostationary Mission Concept.* Technical report, University of Maryland Baltimore County and Goddard Space Flight Center, Baltimore, Mayland and Greenbelt, Maryland, 2008.

19. Rogers, R. M. *Applied Mathematics in Integrated Navigation Systems.* American Institute of Aeronautics and Astronautics, Reston, Virginia, United States, third edition, 2007.

20. Salvini, R., M. Anselmi, A. Indinella, and I. Callegari. *Quickbird Stereo Photogrammetry for Geological Mapping (Cyrene-Libya).* Technical report, Center of Geotechnologies, San Giovanni Valdarno (AR), Italy, 2004.

21. Schmidt, J. "Numerical Simulation of Optical Wave Propagation, With Examples in Matlab", August 2008. Air Force Institute of Technology, Wright Patterson Air Force Base, Ohio, United States.

22. Sellers, J. J. *Understanding Space, An Introduction to Astronautics.* McGraw-Hill Companies, United States, second edition, 2004.

23. Strelow, D. and S. Singh. "Optimal Motion Estimation from Visual and Inertial Measurements". *Proceedings of the Workshop on Applications of Computer Vision*, 1, December 2002.

24. Titterton, D. H. and J. L. Weston. *Strapdown Inertial Navigation Technology.* The Institution of Electrical Engineers and The American Institute of Aeronautics and Astronautics, Stevenage, Herts, United Kingdom and Reston, Virginia, second edition, 2004.

25. Veth, M. J. *Fusion of Imaging and Inertial Sensors for Navigation.* Ph.D. thesis, Air Force Institute of Technology, Wright Patterson Air Force Base, Ohio, United States, 2006.

26. Veth, M. J., R. Anderson, F. Webber, M. Nielsen, and J. Raquet. "Tightly-Coupled INS, GPS, and Imaging Sensors for Precision Geolocation". *Proceedings of the 2008 National Technical Meeting of the Institute of Navigation*, January 2008.

27. Veth, M. J. and J. Raquet. "Fusion of Low-cost Imaging and Inertial Sensors for Navigation". *Proceedings of the Institute of Navigation - 19th International Technical Meeting of the Satellite Division*, 2, 2006.

28. Veth, M. J. and J. Raquet. "Two-Dimensional Stochastic Projections for Tight Integration of Optical and Inertial Sensors for Navigation". *Proceedings of the 2006 National Technical Meeting of the Institute of Navigation*, January 2006.

29. Veth, M. J. and J. Raquet. "Alignment and Calibration of Optical and Inertial Sensors Using Stellar Observations". *Proceedings of ION GNSS 2005*, September 2005.

30. Veth, M. J., J. Raquet, and M. Pachter. *Stochastic Constraints for Fast Image Correspondence Search with Uncertain Terrain Model*. Technical report, Air Force Institute of Technology, Wright Patterson Air Force Base, Ohio, United States, 2007.

31. Wertz, J. R. and W. J. Larson. *Space Mission Analysis and Design*. Microcasm Press and Kulwer Academic Publishers, El Segundo, California, United States and Dordrecht, The Netherlands, third edition, 2003.

32. Zhang, X., X. Yu, and J. Yan. "Influence of Atmospheric Turbulence on Image Resolution of an Optical Remote Sensing System". *Society of Photo-Optical Instrumentation Engineers*, 5639, November 2004.

REPORT DOCUMENTATION PAGE

Form Approved
OMB No. 074-0188

1. REPORT DATE *(DD-MM-YYYY)*	**2. REPORT TYPE**	**3. DATES COVERED** *(From – To)*
26-03-2009	Master's Thesis	June 2008-March 2009

4. TITLE AND SUBTITLE

Satellite-based Fusion of Image/Inertial Sensors for Precise Geolocation

5a. CONTRACT NUMBER

5b. GRANT NUMBER

5c. PROGRAM ELEMENT NUMBER

6. AUTHOR(S)

Jesse, Neil R., Captain, USAF

5d. PROJECT NUMBER
ENG09-152

5e. TASK NUMBER

5f. WORK UNIT NUMBER

7. PERFORMING ORGANIZATION NAMES(S) AND ADDRESS(S)
Air Force Institute of Technology
Graduate School of Engineering and Management (AFIT/EN)
2950 Hobson Way
WPAFB OH 45433-7765 DSN: 785-3636

8. PERFORMING ORGANIZATION REPORT NUMBER

AFIT/EO/ENG/09-04

9. SPONSORING/MONITORING AGENCY NAME(S) AND ADDRESS(ES)

Craig A. Speicher
Senior Astronautical Engineer
Advanced Multi-spectral Sensors Group
Ball Aerospace & Technologies Corp.
2875 Presidential Drive, Suite #180
Fairborn, OH 45324
Voice Mail: 937-320-4184
E-mail: cspeiche@ball.com

10. SPONSOR/MONITOR'S ACRONYM(S)

11. SPONSOR/MONITOR'S REPORT NUMBER(S)

12. DISTRIBUTION/AVAILABILITY STATEMENT

DISTRIBUTION APPROVED FOR PUBLIC RELEASE; DISTRIBUTION UNLIMITED.

13. SUPPLEMENTARY NOTES

14. ABSTRACT

The ability to produce high-resolution images of the Earth's surface from space has flourished in recent years with the continuous development and improvement of satellite-based imaging sensors. Earth-imaging satellites often rely on complex onboard navigation systems, with dependence on Global Positioning System (GPS) tracking and/or continuous post-capture georegistration, to accurately geolocate ground targets of interest to either commercial and military customers. Consequently, these satellite systems are often massive, expensive, and susceptible to poor or unavailable target tracking capabilities in GPS-denied environments. Previous research has demonstrated that a tightly-coupled image-aided inertial navigation system (INS), using existing onboard imaging sensors, can provide significant target tracking improvement over that of conventional navigation and tracking systems. Satellite-based image-aided navigation is explored as a means of autonomously tracking stationary ground targets by implementing feature detection and recognition algorithms to accurately predict a ground target's pixel location within subsequent satellite images. The development of a robust satellite-based image-aided INS model offers a convenient, low-cost, low-weight and highly accurate solution to the geolocation precision problem, without the need of human interaction or GPS dependency, while simultaneously providing redundant and sustainable satellite navigation capabilities.

15. SUBJECT TERMS
Geolocation, Georeferencing, GPS, Image Registration, Imaging, INS, Navigation, Satellite, Tracking

16. SECURITY CLASSIFICATION OF:			**17. LIMITATION OF ABSTRACT**	**18. NUMBER OF PAGES**	**19a. NAME OF RESPONSIBLE PERSON**
REPORT	**ABSTRACT**	**c. THIS PAGE**			Lt Col Michael Veth
U	**U**	**U**	**UU**	121	**19b. TELEPHONE NUMBER** *(Include area code)* (937) 255-3636; email: Michael.Veth@afit.edu